UNIVERSITEIT ANTWERPEN
Faculteit Wetenschappen
Departement Fysica

First-principles electronic structure calculations of transparent conducting oxide materials

---

First-principles berekeningen van de elektronische structuur van transparante geleidende oxide - materialen

Proefschrift voorgelegd tot het behalen van de graad van doctor in de wetenschappen aan de Universiteit Antwerpen te verdedigen door

Hemant Dixit

Promotoren
Prof. Dr. B. Partoens
Prof. Dr. D. Lamoen

Antwerpen
July, 2012

Members of the Jury:

Chairman
Prof. Wim Wenseleers, Universiteit Antwerpen, Belgium

Supervisors
Prof. Bart Partoens, Universiteit Antwerpen, Belgium
Prof. Dirk Lamoen, Universiteit Antwerpen, Belgium

Members
Prof. Jacques Tempère, Universiteit Antwerpen, Belgium
Prof. Nick Van Remortel, Universiteit Antwerpen, Belgium
Prof. Stefaan Cottenier, Universiteit Gent, Belgium
Prof. Xavier Gonze, Université Catholique de Louvain, Belgium

Contact Information

Hemant Dixit
G.U. 313
Groenenborgerlaan 171
2020 Antwerpen
Belgium
Hemant.Dixit@ua.ac.be

Acknowledgement

On this page I wish to express my sincere gratitude to my promoters Prof. B. Partoens and Prof. D. Lamoen, for their motivation, support and guidance during my PhD. They have given me an opportunity and complete freedom to work on interesting research topics during the last four years. This thesis is a result of their consistent encouragement and the fruitful discussions I had with them. My special thanks to Dr. Rolando Saniz for working together and his guidance during early stage of my PhD. My other colleagues in Antwerp: Dr. Ying Xu, Ms. Mozhgan Amini, Dr. Nandan Tandon, Dr. Matsubara Masahiko, Dr. Fabiana Da Pieve have also helped me and provided a cheerful atmosphere. I want to thank the people I collaborated with: Prof. X. Gonze, Prof. Gian-Marco Rignanese, Dr. Martin Stankovski, Ms. Anna Miglio and other members of the ABINIT group in Louvain-la-Neuve along with Prof. Stefaan Cottenier at the University of Ghent. Also I would like to thank Prof. F. Peeters, my colleagues from the CMT group in Antwerp. Finally, special thanks to my parents, family members and many friends including a team called 'Sahyadri Explorers' for supporting me during my studies.

Contents

List of abbreviations **1**

1 Introduction **3**
1.1 Transparent Conducting Oxides 3
1.2 TCO Materials 4
1.2.1 Alternative materials for TCO applications 5
1.3 Basic physics of TCOs 6
1.3.1 Electron energy bands in TCOs 6
1.3.2 Conductivity in TCOs 8
1.3.3 Role of defects 9
1.4 Applications 10
1.5 First-principles study of TCOs 12
1.6 Goal of this thesis 14

2 Electronic structure with Density Functional Theory **17**
2.1 Introduction 17
2.1.1 Born-Oppenheimer approximation 18
2.1.2 The Hartree approximation 19
2.1.3 The Hartree-Fock approximation 19
2.1.4 The correlation energy 20
2.2 The fundamentals of density functional theory 21
2.2.1 The Hohenberg-Kohn theorems 21
2.2.2 The Kohn-Sham equations 22
2.2.3 The exchange-correlation approximations 23
2.3 Computation on solids: electronic band structure 26
2.4 Methods for electronic structure calculations 27
2.4.1 Plane wave pseudopotential method 27
2.4.2 All-electron methods 28
2.4.3 Projector augmented wave method 31
2.5 The band gap problem in DFT 32

3 Electronic band structure of prototype TCOs with DFT 35
3.1 Introduction . . . 35
3.1.1 Computational details . . . 36
3.2 Zinc oxide . . . 37
3.3 Cadmium oxide . . . 38
3.4 Tin dioxide . . . 39
3.5 Indium oxide . . . 40
3.6 Summary . . . 41
3.6.1 Structural properties . . . 41
3.6.2 Electronic properties . . . 42

4 GW approximation: an introduction 45
4.1 Photoelectron spectroscopy . . . 45
4.2 Green's Function . . . 46
4.2.1 The Lehmann representation . . . 47
4.3 Feynman diagrams . . . 48
4.4 The Dyson equation and concept of self-energy . . . 49
4.5 Hedin's equations . . . 52
4.5.1 The GW approximation . . . 58
4.6 The GW approximation in practice . . . 62

5 ZnO: quasiparticle corrections to the band gap 67
5.1 Introduction . . . 67
5.2 Computational details . . . 68
5.3 Result and discussion . . . 69
5.4 Details of 20-electron PP . . . 77
5.5 Effect of plasmon-pole model . . . 78
5.6 Summary . . . 81

6 Quasiparticle band structure of SnO_2 and CdO 83
6.1 Introduction . . . 83
6.2 Computational details . . . 84
6.3 Results and discussion . . . 84
6.3.1 SnO_2 . . . 85
6.3.2 CdO . . . 89

7 TCOs based on ZnX_2O_4 (X=Al,Ga and In) spinel structure 95
7.1 Introduction . . . 95
7.2 Computational details . . . 97
7.2.1 Pseudopotentials . . . 97
7.2.2 DFT, GW and TB-mBJ . . . 97

7.3 Result and discussion 98
7.3.1 Structural properties and electronic band structure using DFT 98
7.3.2 GW and TB-mBJ band gaps 102
7.3.3 Formation enthalpy 105
7.4 Conclusions 106

8 Electronic structure with TB-mBJ scheme 107
8.1 Introduction 107
8.2 Theory 109
8.3 Computational details 110
8.4 Results 110
8.4.1 n-type binary oxides 110
8.4.2 p-type ternary oxides 116
8.5 Discussion and Conclusions 121

9 Formation energy of native defects in $ZnAl_2O_4$ spinel 123
9.1 Introduction 123
9.2 Method and Computational Details 124
9.3 Result and discussion 128
9.3.1 Electronic band structure with HSE06 128
9.3.2 Formation energy with GGA and GGA+U 129
9.3.3 Formation energy with HSE06 130
9.4 Conclusions 132

Summary 133

Samenvatting 137

Appendices 141

List of publications 159

Curriculum Vitae 161

Bibliography 163

List of abbreviations

TCO	Transparent conducting oxides
DFT	Density functional theory
LDA	Local density approximation
GGA	Generalized gradient approximation
PPM	Plasmon-pole model
PP	Pseudopotential
TB-mBJ	Tran-Blaha modified Becke Johnson potential
APW	Augmented plane wave method
LAPW	Linearized Augmented Plane Wave
APW+lo	Augmented plane wave method + local orbitals
PAW	Projector augmented wave method
ZB, RS, WZ	zincblende, rocksalt, wurtzite

Chapter 1

Introduction

1.1 Transparent Conducting Oxides

Transparent conducting oxides (TCO) constitute a unique class of materials which combine two physical properties together - high optical transparency and high electrical conductivity. These properties are generally considered to be mutually exclusive of each other since high conductivity is a property possessed by metals while insulators are optically transparent. This peculiar combination of physical properties is achieved by generating free electron or hole carriers in a material having a sufficiently large energy band gap (i.e., $>\sim$3.1 eV) so that it is non absorbing or transparent to visible light. The charge carriers are usually generated by doping the insulator with suitable dopants and also by defects. It is no wonder that this unique material property makes TCOs technologically an important material and TCOs are widely used in commercial applications such as - in liquid crystal display (LCD), plasma and organic light emitting (OLED) displays; touch-screen sensors; thin-film and organic photovoltaics, OLED lighting; low-e windows and smart windows; solar control film etc.

The TCOs used in technological applications should have following characteristics. First, they should be transparent for the visible part of light with transmittance $>\sim$ 80%. Second, they should be a good conductor of electricity with a high enough concentration of electrical carriers, i.e., an electron or hole concentration $>\sim 10^{19}$ cm^{-3} and with a sufficiently large mobility, $>\sim$ 1 cm^2 V^{-1} s^{-1}. The three most common TCOs are tin doped indium oxide In_2O_3:Sn, fluorine doped tin oxide SnO_2:F, and aluminum doped zinc oxide ZnO:Al. All three of these materials have band gaps above that required for transparency across the full visible spectrum. Note that although these TCOs are considered to be good conductors from the perspective of a

semiconductor, they are actually very poor conductors compared to metals. For example, the best conductivity of In_2O_3:Sn (for indium tin oxide or ITO) is about a factor of 10 to 60 lower than that of a typical integrated circuit contact metal. The low conductance of TCOs compared to metals has important consequences for both TCO and transparent electronics applications. An ideal TCO should have high electrical conductivity combined with low absorption of visible light. Therefore an appropriate quantitative measure of the performance of TCOs is the ratio of the electrical conductivity (σ) to the visible absorption coefficient (α). Thus the figure of merit of TCO material, which is defined as the ratio of the electrical conductivity and the optical absorption

$$\textit{Figure of merit} = \frac{\sigma}{\alpha},$$

is used for quantitative description of TCO performance. Figures of merit for some TCOs are given in Table 1.1.

Table 1.1: Figures of Merit σ/α for some TCOs [From Ref. [1]].

Material	Sheet resistance ($\Omega/$ cm^2)	Visible absorption coefficient (α)	Figure of merit (Ω^{-1})
ZnO:F	5	0.03	7
Cd_2SnO_4	7.2	0.02	7
ZnO:Al	3.8	0.05	5
In_2O_3:Sn	6	0.04	4
SnO_2:F	8	0.04	3
ZnO:Ga	3	0.12	3
ZnO:B	8	0.06	2
SnO_2:Sb	20	0.12	0.4
ZnO:In	20	0.20	0.2

1.2 TCO Materials

A plethora of systems have been studied as candidate material for a TCO [2]. Table 1.2 lists the commonly used TCO host materials and corresponding dopants. These include binary oxides, ternary oxides and also multicomponent oxides. Among these the binary oxides: In_2O_3, SnO_2, ZnO and CdO form a kind of basic set of TCO host materials since most of the ternary, multicomponent oxide systems are derived from these. Sn-doped In_2O_3 thin films [$In_{2-x}Sn_xO_3$:ITO] show the best performance as TCO and are widely

Table 1.2: TCO materials.

Material	Dopant or compound
In_2O_3	$Sn, Ge, Mo, F, Ti, Zr, Hf, Nb, Ta, W, Te$
SnO_2	Sb, F, As, Nb, Ta
ZnO	$Al, Ga, B, In, Y, Sc, F, V, Si, Ge, Ti, Zr, Hf$
CdO	In, Sn
$ZnO - SnO_2$	$Zn_2SnO_4, ZnSnO_3$
$ZnO - In_2O_3$	$Zn_2In_2O_5, Zn_3In_2O_3$
$In_2O_3 - SnO_2$	$In_4Sn_3O_{12}$
$CdO - SnO_2$	$Cd_2SnO_4, CdSnO_3$
$CdO - In_2O_3$	$CdIn_2O_4$
$GaInO_3, (Ga, In)_2O_3$	Sn, Ge
$CdSb_2O_6$	Y
$ZnO - In_2O_3 - SnO_2$	$Zn_2In_2O_5 - In_4Sn_3O_12$
$CdO - In_2O_3 - SnO_2$	$CdIn_2O_4 - Cd_2SnO_4$
$CuXO_2$	$X = Al, Ga, In$
$ZnXO_4$	$X = Al, Ga, Co, Rh, Ir$

used in most optoelectronic devices. However, since ITO is an expensive material there is a necessity of finding economic alternatives and other systems - particularly Al doped ZnO is being explored as viable alternative. These basic TCOs are n-type conducting and p-type conductivity is a relatively rare phenomenon. Only few systems are known to be p-type conducting, these include delafossite $CuXO_2$ (X=Al, Ga and In) [3, 4, 5, 6] and the ZnX_2O_4 (X=Co, Rh and Ir) [7, 8, 9] spinel structures.

1.2.1 Alternative materials for TCO applications

There are also alternative non-oxide materials which are transparent and conducting, particularly here I would like to mention graphene. Graphene, which is a single-layer of carbon, also exhibits high electrical conductivity and high optical transparency [10, 11]. The advantages of graphene over TCOs are its mechanical strength and flexibility, in contrast to ITO, which is brittle. Moreover, since it is a carbon derivative it is cheap and available in abundance. Additionally, graphene films may be deposited from solution over large areas. Still it is unlikely to replace the TCOs in all the devices for practical reasons that there is an existing technology to synthesize and fabricate TCO devices, moreover the graphene films are sensitive to surface roughness [12] while TCOs can be easily fabricated on rough surfaces. Ad-

ditionally a wide range of TCO material system also provides an access to a wide range of physical properties such as the work function.

1.3 Basic physics of TCOs

1.3.1 Electron energy bands in TCOs

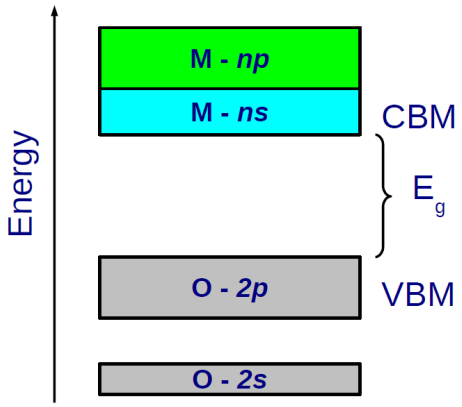

Figure 1.1: Schematic illustration of electronic states in metal oxides.

In the simple metal oxide compounds such as ZnO, CdO, and SnO_2, the metal cations have ns^0 (n being the valence shell of metal atom and the s^2 electrons are transferred to the oxygen in the compound) and oxide anions have $2s^2$,$2p^6$ valence electron configurations. A schematic illustration of these energy bands is shown in Fig. 1.1 and also the band structure of ZnO calculated using the local density approximation (LDA) within density functional theory (DFT) is shown in Fig. 1.2. The valence band maximum (VBM) is formed with the filled O $2p^6$ orbitals, while the conduction band minimum corresponds to the empty metal-centered ns^0 orbital. From the band structure and projected density of states (PDOS) of ZnO shown, it can be seen that the narrow Zn $3d$ bands lie several eV below the VBM. The conduction band shows ns-np orbital mixing at the Γ point while moving away from this point the s-band exhibits greater mixing with the p orbitals. The conduction band minimum (CBM) has a high dispersion and an approximately parabolic shape characteristic of the free-electron model of a metal. The high dispersion of the band contributes to a small electron mass ($\sim$0.3 m_e in case of ZnO) and a high mobility. Thus these metal oxides are

a suitable choice as TCO host materials. The large band gap ensures the optical transparency. Suitable dopants then can introduce energy levels in the proximity to the CBM. In the case of ZnO - Al, Ga or In are the suitable candidates. These metals contain an extra electron (np^1) in the valence compared to a Zn atom. The doping is typically substitutional and the Zn cations are replaced by the metal ions. The extra electron then populates the conduction band and a degenerate electron gas is produced. Since these carrier electrons are confined to the conduction band, a wide dispersion of the conduction band is necessary to reduce the scattering of free carriers and assure high conductivity.

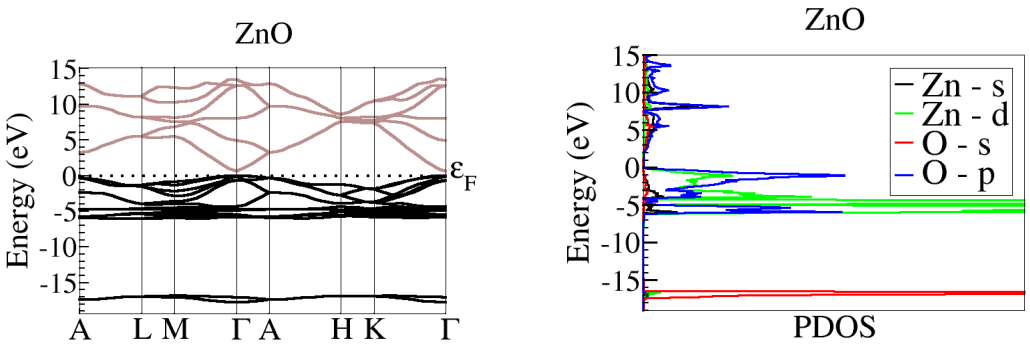

(a) (b)

Figure 1.2: (a)-electronic band structure and (b)-PDOS of ZnO calculated using LDA within DFT (a detailed discussion follows in chapter 3).

Doping leads to perturbation of the electron energy bands in TCO materials. When ZnO is doped with Al, defect levels are introduced near the bottom of the conduction band thereby leading to an increase in the bandgap energy. The resulting blue shift in the high-energy absorption edge is known as the Burstein-Moss effect [13, 14, 15]. The Burstein-Moss is schematically represented in Fig. 1.3. In conclusion, the electrical conductivity is imparted in wide band gap metal oxides by dopants. The defect energy levels introduced can either donate electrons (free carriers) to the host metal oxide conduction band (n-type conductor) or accept electrons from the metal oxide valence band (p-type hole conductor) and the resulting TCO shows either n-type or p-type conductivity. Thus the understanding of electron energy bands in TCOs is important to enhance the performance and for the development of new materials.

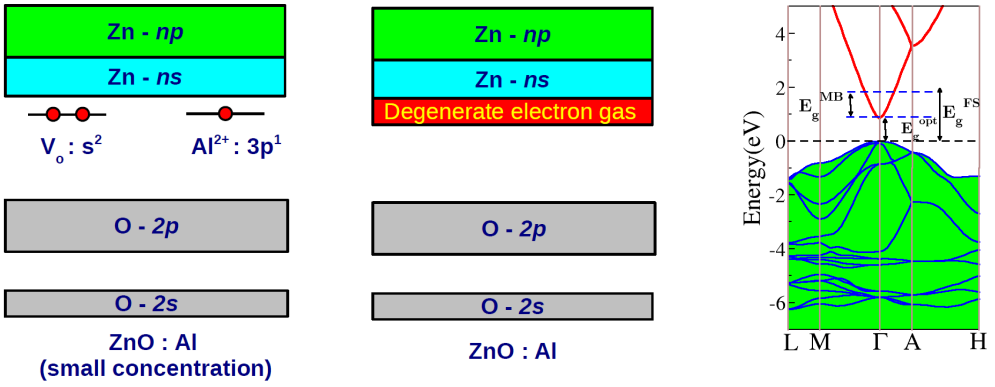

Figure 1.3: (a),(b) Schematic illustration of defect (Al) electronic states in metal oxides and (c) The schematic band structure highlighting the Fermi level stabilization energy, E_g^{FS}, the Moss-Burnstein shift, E_g^{MB}, and the optical band gap, E_g^{opt}, for defective ZnO. The green shaded areas indicate occupation by electrons.

1.3.2 Conductivity in TCOs

The materials physics of TCOs can be reasonably well understood with the help of simple arguments. The basic idea is to create free charge carriers (electrons or holes) in wide band gap insulators using suitable dopants. For example, the chemical doping of Sn^{4+} for In^{3+} in ITO leads to donor induced states located close to the host (In_2O_3) conduction band. The oxygen vacancies (In_2O_{3-x}) can also introduce impurity states in the band gap which may contribute to the conductivity. Further doping of Sn^{4+} leads to a degenerate gas of current-carrying electrons which gives rise to far-infrared absorption and high electronic conductivity, but at the same time the fundamental host band gap is left intact. Thus the electrically conductive material remains optically transparent in the visible region. The mechanism of conductivity in TCOs can be understood with the help of classical (Drude like) description of charge transport in metals. The charge carriers produced through doping are to be treated as the free electron gas, thus the conductivity (σ)

is determined by the density of charge carriers and their effective mass:

$$\sigma = \frac{n_e e^2 \tau}{m_e} = n_e e \mu_e$$

where n_e is the number of charge carriers, m_e is their effective mass, τ is the relaxation time and $\mu_e = e\tau/m_e$ is the mobility of the charge carriers. The plasmon frequency associated with the degenerate free electron gas, in the limit of high electron density [16], is given by:

$$\omega_p = \left(\frac{ne^2}{\epsilon_\infty \epsilon_0 m^*} \right)^{1/2}$$

The 'optical window' for ITO is thus set by the plasmon frequency (proportional to the number of charge carriers) at longer wavelengths and at short wavelengths by its direct band gap (around 3.1 eV). The response of TCO material to incident light is schematically illustrated in Fig. 1.4. The incident photons having lower energy than the plasmon frequency are reflected and those with energy higher than the band gap are absorbed by the TCO. Thus by shifting the plasmon frequency (by changing the number of charge carriers) the infrared (IR) part of visible spectrum can be either transmitted or blocked by the TCO. The key physical properties of a TCO material are the band gap for optical transparency, the effective mass of the electron which determines the mobility of charge carriers and the plasmon frequency. Also a large second band gap which is the difference between the two lowest conduction bands, is essential. The larger value of the second band gap lowers the intraband transition of charge carriers and thereby ensures optical transparency.

1.3.3 Role of defects

It is observed that undoped as-grown TCO thin films and bulk crystals typically exhibit n-type conductivity. The origin of this unintentional conductivity is not clear and often it is attributed to native point defects. The unintentional conductivity is commonly attributed to the cation interstitials or oxygen vacancies based on its observed dependence on oxygen content in the growth environment. The defects and impurities in TCOs also play an important role in determining their electronic structure and physical properties as it is observed for semiconductors.

First-principles total energy calculations based on DFT can be used to calculate the formation energy of native point defects. The calculated formation energies are key quantities in the characterization of defects since we

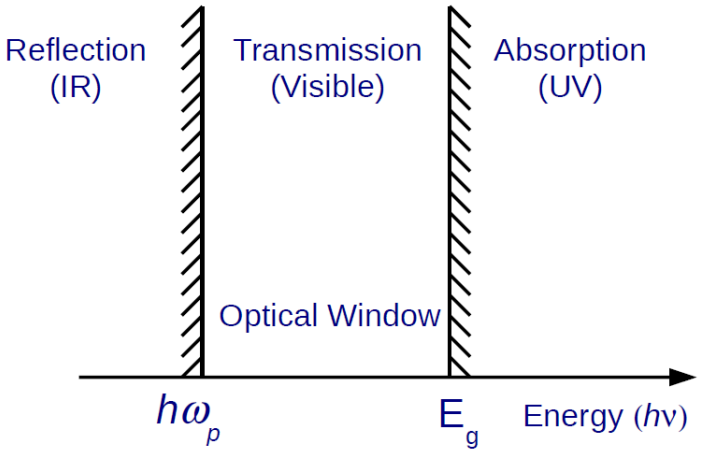

Figure 1.4: The 'optical window' set by plasma frequency (ω_p) and the band gap (E_g).

can derive equilibrium concentrations of defects, stability of different charge states and the electronic transition levels from them [17]. Thus the electronic structure study of intrinsic defects is necessary to understand if defects are likely to contribute to the conductivity and can provide guidelines for experimental growth conditions facilitating a control over conductivity.

1.4 Applications

The unique material property of being transparent and conducting makes TCOs technologically important materials. TCOs are widely used in a large number of opto-electronic devices and more applications are yet to be explored. The well known applications are described briefly in the following. Most of these devices use TCOs in the form of thin films coated over suitable substrates.

- Solar cells - The front surfaces of solar cells are covered by transparent electrodes. A typical architecture of (a) a thin film solar cell and (b) an organic solar cell is shown in Fig. 1.5. A TCO layer is generally used for the front contact of all thin-film silicon solar cells, whereas a reflective contact material is needed at the back. In solar cell, TCOs are needed as a contact for collection of the photo-generated carriers while still allowing the light to reach the active solar absorber material.

The optical qualities of these materials substantially affect the required thickness of the silicon absorber layer, in terms of facilitating the absorption of an optimal amount of irradiation. ITO is widely used in the organic solar cells due too its high transparency and low resistivity. However limited supply of In makes it an expensive material and cheaper alternatives such as ZnO:Al have great demand by industries.

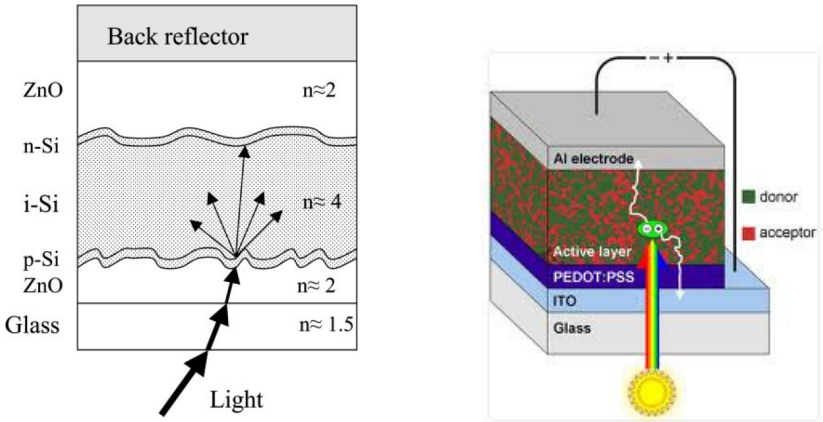

(a) (b)

Figure 1.5: A typical architecture of a) thin film solar cell and b) organic solar cell [from Ref. [18]].

- Flat-panel displays - The many different styles of flat-panel displays use a transparent conductor as a front electrode. The role of TCOs is to pass the electrical signals to the pixels forming the display and simultaneously allow the light generated to pass on to viewer. Etchability is a very important consideration in forming patterns in the transparent conducting electrode. The easier etchability of ITO has favored its use over tin oxide, which is more difficult to etch. The low deposition temperature of ITO is also a factor for color displays in which the transparent conductor is deposited over thermally sensitive organic dyes. Low resistance is another factor favoring ITO in very finely patterned displays, since the ITO layer can be made very thin, thus the etched topography remains fairly smooth. ZnO is lower in cost and easier to etch than ITO, so ZnO may replace ITO in future displays.

- Smart windows - Smart windows use TCO coatings on glass. Typically, the function of a smart window is to electronically block some or all of

the light incident onto a window. Since the plasma frequency can be tuned, the TCO coating can either block or allow the IR part of light thereby allowing control over room temperature. Thus in cold climates, TCO coated glass can be used to reflect heat back into the residential space, while in hot climates the reverse approach is taken. Also the smart window eliminates the need for blinds or drapes, and, if UV is blocked, helps to protect carpeting and furniture from fading.

- Touch screens - Touch screens, commonly used in devices such as mobile phones or ATM machines, are formed from etched TCOs on glass. They sense the presence of a finger by direct contact or capacitively through the glass. The resistive system consists of a normal glass panel that is covered with a conductive and a resistive metallic layer. These two layers are held apart by spacers, and a scratch-resistant layer is placed on top of the whole setup. An electrical current runs through the two layers while the device is operational. When a user touches the screen, the two layers make contact in that exact spot. The change in the electrical field is noted and the coordinates of the point of contact are further acted upon by the device. In the capacitive system, a layer that stores electrical charge is placed on the glass panel of the monitor. When a user touches the monitor with his or her finger, some of the charge is transferred to the user, so the charge on the capacitive layer decreases. This decrease is measured in circuits located at each corner of the device and further this signal is processed.

- Automotive applications - An automobile affords numerous application venues for transparent electronics. Obvious candidate platforms include window glass, dashboards, and navigation systems.

- Transparent electronics - Most of TCOs show n-type conductivity, however, if p-type conducting TCO a is synthesized a transparent p-n junction can be formed. This may lead to an era of transparent electronics where the electronic circuits are transparent. Moreover, futuristic applications such as flexible electronic newspapers and wearable clothing displays may also be realized.

1.5 First-principles study of TCOs

The number of TCO related research articles published over a period of last 12 years is shown in 1.6. This citation report is obtained from the Web of Science with the search keyword “TCO” that appears in the topic

from the year 2000 to 2012. The trend shows a steep rise in the number of publications each year, which clearly indicates that TCOs offer an active field of research for both theory and experiments. There is an ever increasing demand of TCO materials by the industries. Also the emerging technological applications demand higher performance from TCOs. Therefore a deeper understanding of the materials physics of the microscopic electronic structure and mechanisms driving the unique combination of electrical and optical properties in TCOs is essential. Specifically, the elucidation of electronic structure of the host material, the effect of dopants on the electronic structure and further the electron scattering mechanisms of the degenerate electron gas produced is necessary to improve the performance of the TCOs. *Ab initio*

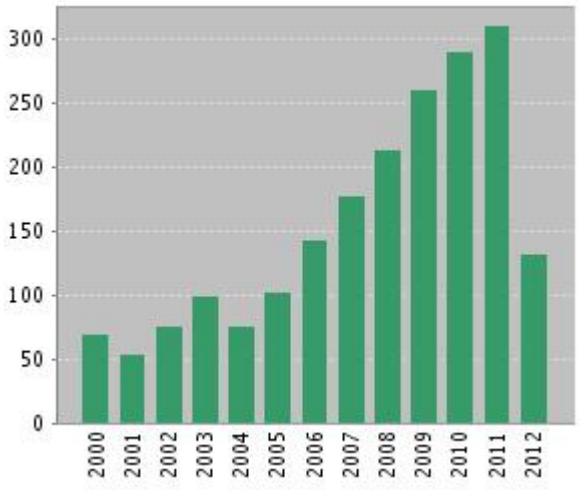

Figure 1.6: Number of TCO related publications over last decade (source: Web of Science).

electronic structure calculations are necessary to understand the basic physics that governs the behavior of the electronic states. It also offers a vital tool for efficient materials design. The key physical properties of TCO host materials are the band gap for optical transparency and the effective masses which determines the mobility of the charge carriers. The application of electronic structure methods, capable of calculating these quantities accurately, is thus helpful in order to find better performing or new TCO materials. Thus the electronic structure of these metal-oxide semiconductors has been a subject of enduring interest.

The majority of the available theoretical studies on TCOs report band structures calculated using DFT formalism. The key quantity in DFT is the electron density from which all ground-state properties can be determined. It serves as the workhorse technique in first principles materials simulation. Approaches based on DFT are widely available in a number of academic and commercial packages, e.g. the codes ABINIT, WIEN2K etc. However the widely used exchange-correlation functionals such as the LDA or generalized gradient approximation (GGA) within DFT, fail to give a proper description of electronic states due to a discontinuity in the exchange-correlation potential [19, 20, 21, 22]. As a result, the calculated electronic band gaps within DFT are severely underestimated (a detailed discussion follows in the next chapter).

Thus, for quantitative band gap predictions, one should make use of many-body approaches such as the GW theory. Such a method can obviate the limitations of standard DFT for the calculation of electronic and optical properties of complex materials [23]. The GW method where the electron self-energy is obtained as the product of the one-particle Greens function and of the screened Coulomb interaction, enables the accurate determination of quasiparticle excitation energies and lifetimes. These physical quantities are key to interpreting a number of experiments, ranging from angle-resolved photoemission spectroscopy to charge transport in molecular electronics. However, the use of the GW method has been limited, with respect to that of standard DFT, by the much higher computational cost. Only the past few years have witnessed a more widespread use of the GW method, following the introduction of more efficient algorithms, the increased performance and availability of supercomputing clusters, and the availability of reliable and efficient software for GW calculations [24, 25, 26].

1.6 Goal of this thesis

This thesis is confined to computational research on TCO host materials and following two topics are addressed in this thesis: (1) Before real materials design is possible using *ab initio* techniques, reliable and well understood methods must be available. Therefore, an accurate description of the electronic band structure using state of the art DFT and the GW approximation for TCO materials is prepared in this thesis. (2) The formation energy of native defects in TCO host materials: The presence of naturally occurring defects, during the growth of TCO films, introduces the impurity states in the band gap. Their classification as shallow donor or impurity states is necessary to explain the origin of unintentional conductivity in these materials.

The thesis is organized as follows. Chapter 2 contains a brief discussion of DFT and ways to solve the Kohn-Sham equations. In the third chapter the structural parameters and electronic band structure, calculated using DFT, is presented for prototype n-type conducting TCOs. It is observed that the calculated band gaps of TCOs are severely underestimated. Thus to access the excited state we use the GW approximation to many body perturbation theory and the theoretical background is presented in chapter 4. We have studied in detail three binary oxides namely - ZnO, CdO, SnO_2 and the calculated quasiparticle band structure is presented in the successive chapters. Chapter 5 contains a systematic study of the self-energy dependence on the pseudopotentials used and results are obtained for ZnO in different phases. Chapter 6 shows the quasiparticle band structure calculated for SnO_2 and CdO. Further, in chapter 7, we study TCOs based on the spinel structure and calculate the quasiparticle corrections to the band gap for the ZnX_2O_4 (X=Al, Ga and In) spinels. Chapter 8 deals with the recently proposed Tran-Blaha modified Becke-Johnson potential scheme. This scheme has emerged as a computationally inexpensive technique to calculate band gaps which shows good agreement with the experiment for a wide class of semiconductors and insulators. We present the electronic band structure of prototype p and n-type conducting TCOs using this scheme. Finally in the last chapter, the formation energies of native defects in $ZnAl_2O_4$ spinel are presented. These calculations are performed using hybrid functionals.

Chapter 2

Electronic structure with Density Functional Theory

2.1 Introduction

All materials are composed of atomic nuclei and electrons. The macroscopic material properties that we observe only depend on the position of these electrons and ions. Thus knowing only the type of atoms the material is made of is in principle enough to calculate the wave function and energy of the system using the (time independent) Schrödinger equation

$$H\Psi(\mathbf{r}_1, \mathbf{r}_2, ..., \mathbf{R}_1, \mathbf{R}_2, ...) = E\Psi(\mathbf{r}_1, \mathbf{r}_2, ..., \mathbf{R}_1, \mathbf{R}_2, ...) \tag{2.1}$$

where Ψ is the wave function of the system, $\mathbf{r}_i$ and $\mathbf{R}_i$ are the positions of the electrons and ions respectively, and H is the Hamiltonian for the system:

$$\begin{aligned} H = -\sum_i \frac{\hbar^2 \nabla_i^2}{2m_e} - \sum_{i,I} \frac{1}{4\pi\epsilon_0} \frac{Z_I e^2}{|\mathbf{r}_i - \mathbf{R}_I|} + \frac{1}{2} \sum_{i \neq j} \frac{1}{4\pi\epsilon_0} \frac{e^2}{|\mathbf{r}_i - \mathbf{r}_j|} \\ - \sum_I \frac{\hbar^2 \nabla_I^2}{2M_I} + \frac{1}{2} \sum_{I \neq J} \frac{1}{4\pi\epsilon_0} \frac{Z_I Z_J e^2}{|\mathbf{R}_I - \mathbf{R}_J|} \end{aligned} \tag{2.2}$$

M_I and Z_I are the nucleus mass and charge respectively and m_e is the electron mass. This Hamiltonian can be decomposed in five terms

$$H = T_e + V_{ext} + V_{int} + T_N + V_N \tag{2.3}$$

where T_e and T_N are the kinetic energy operator of electrons and nuclei respectively, V_{ext} is the potential energy of the electrons in field of nuclei, V_{int} represents the Coulomb interaction between the electrons and similarly

E_N is the Coulomb interaction between nuclei. These calculations are known as first-principles or ***ab initio*** calculations since they are based only on the laws of physics and the values of nature's constants, such as Planck's constant $\hbar$ and the electron charge e. Nothing else is assumed or used as empirical input.

In practice, however, it is only possible to solve the Schrödinger equation exactly for small simple systems such as the hydrogen atom with spherical symmetry. For larger systems like molecules and solids, additional approximations have to be made. Note that hereafter we will make use of atomic units to simplify the formulas. In atomic units we have $\hbar = m_e = e = 4\pi\epsilon_0 = 1$.

2.1.1 Born-Oppenheimer approximation

The first step is the *Born-Oppenheimer approximation* which separates the motion of the ions and the electrons. This is justified by the fact that the mass of a nucleus is much larger than the mass of an electron so that they move on different time scales. From the electron point of view, the ions are stationary and the electron cloud will rearrange itself instantaneously to any new ionic configuration. Mathematically, the wave function is rewritten as a product of the electron wave function and the nuclear wave function

$$\Psi(\mathbf{r}_1, \mathbf{r}_2, ..., \mathbf{R}_1, \mathbf{R}_2, ...) = \psi(\mathbf{r}_1, \mathbf{r}_2, ...; \mathbf{R}_1, \mathbf{R}_2, ...) \cdot \chi_{nuc}(\mathbf{R}_1, \mathbf{R}_2, ...) \quad (2.4)$$

The semicolon in the electron wave function indicates that it is dependent upon the ionic positions as parameters but not as variables. The Schrödinger equation of the electrons for a given frozen ionic configuration is written as follows:

$$H'\psi(\mathbf{r}_1, \mathbf{r}_2, ...; \mathbf{R}_1, \mathbf{R}_2, ...) = E'\psi(\mathbf{r}_1, \mathbf{r}_2, ...; \mathbf{R}_1, \mathbf{R}_2, ...) \quad (2.5)$$

H' represents the electronic Hamiltonian consisting of only electronic terms:

$$H = T_e + V_{ext} + V_{int} \quad (2.6)$$

and the total Hamiltonian is then reduced to:

$$H = T_e + V_{ext} + V_{int} + V_N \quad (2.7)$$

With the Born-Oppenheimer approximation, the original problem is now reformulated as a quantum many-body problem for the electrons in an Hamiltonian set by the nuclei positions. The last, and probably hardest, obstacle to overcome is the reduction of the many-electron equation above to a solvable problem.

2.1.2 The Hartree approximation

The simplest way to solve the many-electron equation is to rewrite Eq.(2.5) as a one-particle equation for an electron moving in an average potential from all the electrons, as proposed by Hartree. The wave function then becomes

$$\psi(\mathbf{r}_1, \mathbf{r}_2, ..., \mathbf{r}_n) = \phi_1(\mathbf{r}_1)\phi_2(\mathbf{r}_2)\cdots\phi_n(\mathbf{r}_n) \tag{2.8}$$

The $\phi_i(\mathbf{r}_i)$ are n independent electron wave functions. A fundamental result in quantum mechanics states that if E_0 is the ground state energy solution of the Schrödinger equation, for any wavefunction φ:

$$\frac{\langle\varphi|H|\varphi\rangle}{\langle\varphi|\varphi\rangle} \geq E_0 \tag{2.9}$$

This is called the variational principle. This principle can be used with the Hamiltonian in Eq.(2.3) and the constraint that the wave function should have the Hartree form (presented in Eq.(2.8)) to prove that the solution to the Schrödinger equation in the Hartree approximation is obtained by solving the *Hartree equation*

$$\big[-\sum_i \frac{\nabla_i^2}{2} - \sum_I \frac{Z_I}{|\mathbf{r}_i - \mathbf{R}_I|} + \sum_{j\neq i}\int \phi_j^*(\mathbf{r}_j)\frac{1}{|\mathbf{r}_i - \mathbf{r}_j|}\phi_j(\mathbf{r}_j)\big]\phi_i(\mathbf{r}_i) = \epsilon_i\phi_i^*(\mathbf{r}_i) \tag{2.10}$$

In the Hartree approximation, each electron i is treated independently but in an effective potential determined by an integration over the wave functions of the other electrons. Thus, the Hartree approximation is a mean-field approximation replacing the complicated many-body problem by n simpler problems in a mean-field potential. Hartree also proposed a *self-consistent* way to solve this equation since for the i^{th} wave function, the effective potential depends on all the other wave functions. Self-consistency is a procedure in which the wave function for the step k are found through solving the Eq.(2.10) with the effective potential determined by the wave function in step $k-1$. The procedure is repeated until all the wave functions converge to a solution.

2.1.3 The Hartree-Fock approximation

Electrons being fermions, the exact many-particle wavefunction needs to be antisymmetric by exchange of electrons:

$$\psi(\mathbf{r}_1, \mathbf{r}_2, ..., \mathbf{r}_j, ..., \mathbf{r}_k, ..., \mathbf{r}_n) = -\psi(\mathbf{r}_1, \mathbf{r}_2, ..., \mathbf{r}_k, ..., \mathbf{r}_j, ..., \mathbf{r}_n) \tag{2.11}$$

This constraint can be added to the independent electron Hartree approach by using a Slater determinant as wavefunction instead of Eq.(2.8):

$$\Psi(\mathbf{r}_1, \mathbf{r}_2, ..., \mathbf{r}_n) = \frac{1}{\sqrt{n!}} \begin{vmatrix} \phi_1(\mathbf{r}_1) & \phi_2(\mathbf{r}_1) & \cdots & \phi_n(\mathbf{r}_1) \\ \phi_1(\mathbf{r}_2) & \phi_2(\mathbf{r}_2) & \cdots & \phi_n(\mathbf{r}_2) \\ \vdots & \vdots & & \vdots \\ \phi_1(\mathbf{r}_n) & \phi_2(\mathbf{r}_n) & \cdots & \phi_n(\mathbf{r}_n) \end{vmatrix} \tag{2.12}$$

Using the variational principle with this Slater determinant, it can be proven that the best solution is obtained by solving the *Hartree-Fock* equation:

$$\begin{aligned} \big[-\sum_i \frac{\nabla_i^2}{2} - \sum_I \frac{Z_I}{|\mathbf{r}_i - \mathbf{R}_I|} + \sum_j \int \phi_j^*(\mathbf{r}_j) \frac{1}{|\mathbf{r}_i - \mathbf{r}_j|} \phi_j(\mathbf{r}_j) \big] \phi_i(\mathbf{r}_i) \\ - \sum_j \big[\int \phi_j^*(\mathbf{r}_j) \frac{1}{|\mathbf{r}_i - \mathbf{r}_j|} \phi_i(\mathbf{r}_j) \big] \phi_j(\mathbf{r}_i) = \epsilon_i \phi_i^*(\mathbf{r}_i) \end{aligned} \tag{2.13}$$

The effect of the new constraint is to add a term, called the exchange potential, to the Hartree Eq.(2.10).

2.1.4 The correlation energy

The Hartree-Fock approach assuming independent electrons in an effective potential is an approximation to the true many-body problem. The energy missing is defined as the *correlation* energy ($E_{corr.} = E_{exact} - E_{HF}$). Many methods exist to introduce this correlation energy very accurately for instance Møller-Plesset (MP) perturbation theory, configuration interaction (CI), or coupled cluster (CC) methods or quantum Monte-Carlo methods. However, these methods are computationally very expensive and only the smallest systems can be currently computed. On the other hand, Density Functional Theory (DFT) offers a good compromise between the qualitative description of electronic structure and the computational effort required to produce the result. Thus DFT is one of the most popular and successful quantum mechanical approaches to describe matter. It is nowadays routinely applied for calculating, e.g., the binding energy of molecules in chemistry and the electronic band structure of solids in physics. In this thesis we apply DFT to solve the electronic Hamiltonian for periodic crystals. There are many excellent reviews and books available [27, 28, 29, 30] to which the reader may refer for details. In the following sections we will discuss the basic theorems of DFT and the approximations that are used in practical calculations.

2.2 The fundamentals of density functional theory

2.2.1 The Hohenberg-Kohn theorems

Modern theory of DFT is based on the two Hohenberg-Kohn (HK) theorems [31, 32]: the first theorem states that the many-body wave function, which has a central position in standard quantum theory, can be replaced by the electron ground state density without any loss of information and the second theorem is more or less the equivalent of the variational principle in standard quantum mechanics. In DFT the electron density is the central quantity. In a system of n electrons the electron density is defined from the wave functions as follows,

$$n(\mathbf{r}) = \sum_{i=1}^{N} \int \cdots \int d\mathbf{r}_1 ... d\mathbf{r}_N \Psi^*(\mathbf{r}_1, ..., \mathbf{r}_N) \delta(\mathbf{r}_i - \mathbf{r}) \Psi(\mathbf{r}_1, ..., \mathbf{r}_N) \qquad (2.14)$$

The energy is now rewritten from being the expectation value of the electronic Hamiltonian to a functional only depending on the electron density and not explicitly the wave function.

The first Hohenberg-Kohn theorem is:

Theorem 1. *For any system of interacting particles in an external potential $V_{ext}(\boldsymbol{r})$ the potential $V_{ext}(\boldsymbol{r})$ is determined uniquely, except for a constant, by the ground state density $n_0(\boldsymbol{r})$.*

This implies that all the properties can thus be extracted from the exact ground state electron density. The problem is now only how to find this density. The second theorem based on the variational principle is helpful in this matter.

Theorem 2. *A universal functional for the energy $E[n]$ in terms of the density $n(\boldsymbol{r})$ can be defined, valid for any external potential $V_{ext}(\boldsymbol{r})$. The exact ground state energy of the system is the global minimum of this functional and the density that minimizes the functional is the exact ground state density $n_0(\boldsymbol{r})$.*

This reduces the very complex problem of finding all ground state physical properties of a system to finding the minimum of the energy with respect to the electron density. The energy functional is as follows:

$$E_{HK}[n] = T[n] + E_{int}[n] + \int V_{ext}(\mathbf{r}) n(\mathbf{r}) d\mathbf{r} \qquad (2.15)$$

where $E_{HK}[n]$ is the total energy functional, $T[n]$ its kinetic energy part and $E_{int}[n]$ the part coming from the electronic interactions. E_N does not depend on the density and is due to the nuclei-nuclei interaction. It should be noted that although the first Hohenberg-Kohn theorem requires a non-degenerate ground state, degenerate ground states are also allowed by the Levy formulation [28]. It should also be noted that using the Hohenberg-Kohn formulation of DFT implies that we are working at $T = 0$ K.

2.2.2 The Kohn-Sham equations

The Hohenberg-Kohn theorems show that the electron density can rigorously be made the fundamental quantity of the many-body problem, but they are pure theorems of existence and say nothing on how this exact charge density can be found.

Kohn and Sham have shown that there is a way to map the problem of solving Eq.(2.15) to the one of solving a system of noninteracting electrons moving in an effective potential from all the (other) electrons. According to Theorem 2, the true electron density will minimize the total energy, but all means of finding it are valid. It could be guessed or, as suggested by Kohn and Sham [32], calculated from a reference system of non-interacting electrons moving in an effective potential. Thus, developing this variation with the full energy functional added (Eq.(2.15)), under the condition that the sum of the density throughout the molecule or solid should be constant and equal to the number of electrons,

$$\int_V n(\mathbf{r})d\mathbf{r} = n_e \tag{2.16}$$

finally gives the Schrödinger-like equations called the Kohn-Sham equations:

$$\mathcal{H}\phi_i = [-\frac{1}{2}\nabla^2 + V_{eff}(\mathbf{r})]\phi_i = \epsilon_i\phi_i \tag{2.17}$$

$\mathcal{H}$ is the one electron Hamiltonian and $V_{eff}(\mathbf{r})$ the effective potential in which the electron moves. The effective potential is given by

$$V_{eff}(\mathbf{r}) = V_{ext} + V_H + V_{XC} = V_{ext}(\mathbf{r}) + \int \frac{n(\mathbf{r}')}{|\mathbf{r} - \mathbf{r}'|}d\mathbf{r}' + \frac{\delta E_{XC}[n(\mathbf{r})]}{\delta[n(\mathbf{r})]} \tag{2.18}$$

Since the electron density,

$$n(\mathbf{r}) = \sum_{i=1}^{occ.} |\phi_i(\mathbf{r})|^2, \tag{2.19}$$

is needed to calculate the last two terms, which are the Coulomb potential from all electrons and the exchange-correlation potential, the Kohn-Sham equations need to be solved self-consistently. The new term, the exchange-correlation potential, appearing here contains all the many-body effects that are not present in the classical Hartree interaction term. The initial electron density can be chosen, for example, as a superposition of atomic densities. The Kohn-Sham equations can now be solved instead of finding the minimum of Eq.(2.15), and the orbitals $\phi_i(\mathbf{r})$ then give the electron density according to Eq.(2.19) above. These orbitals are often called Kohn-Sham orbitals and in the case of a non spin-polarized system, each of these orbitals contain two electrons. (To deal with the spin-related effects, the total density is instead expressed as the sum of the spin-up and spin-down densities $n(\mathbf{r}) = n_\uparrow(\mathbf{r}) + n_\downarrow(\mathbf{r})$).

2.2.3 The exchange-correlation approximations

The local density approximation:

The simplest physical way to approximate the exchange-correlation energy is the Local Density Approximation (LDA). In this approximation two assumptions are made: i) the local exchange-correlation energy per particle only depends on the local density (hence the name of the approximation) and ii) is equal to the exchange-correlation energy per particle of a homogeneous electron gas, that has the same density, in a neutralizing positive background (jellium background). The total exchange-correlation energy E_{XC} is then given by the sum of the contributions of each point in space, where it is assumed that the contribution of one point only depends on the density of that particular point, independent of the other points. So

$$E_{XC}[n] = \int n(\mathbf{r})\epsilon_{XC}(n(\mathbf{r}))d\mathbf{r} \tag{2.20}$$

where $\epsilon_{XC}(n(\mathbf{r}))$ is the exchange-correlation energy per particle of a uniform electron gas of density $n(\mathbf{r})$. The quantity $\epsilon_{XC}(n(\mathbf{r}))$ can be further split into exchange and correlation contributions,

$$\epsilon_{XC}(n(\mathbf{r})) = \epsilon_X(n(\mathbf{r})) + \epsilon_C(n(\mathbf{r})) \tag{2.21}$$

The exchange part, ϵ_X, represents the exchange energy of an electron in a uniform electron gas and is given by

$$\epsilon_X = -\frac{3}{4}\sqrt[3]{\frac{3n(\mathbf{r})}{\pi}} \tag{2.22}$$

The correlation part, ϵ_C, is determined using quantum Monte-Carlo simulations of the homogeneous electron gas as proposed by Ceperly and Alder [33].

This approximation is more accurate for systems with slowly varying densities, as it is assumed that the density is locally a constant. While being a simple approximation, the results of this approximation are surprisingly good. In general, LDA almost always leads to a correct picture of binding trends across the periodic table. Also structures, bond lengths, vibrational energies, phonon spectra and other properties are predicted correctly, or with a systematic deviation. Binding energies of solids and molecules are usually overestimated, which leads to an underestimation of the bond lengths. Band gaps are also underestimated (a notorious example of this is the bandgap of bulk Ge, which is predicted to be metallic).

The generalized gradient approximation:

In LDA one uses the knowledge of the density in a point $\mathbf{r}$. In real systems the density varies in space. A logical improvement of the LDA approximation would be to include also information of this rate of change in the functional. This can be done by adding gradient terms. This approach is called the gradient-expansion approximation. In this class of approximation one tries to systematically calculate gradient-corrections of the form $|\nabla n(\mathbf{r})|$, $|\nabla n(\mathbf{r})|^2$, $|\nabla^2 n(\mathbf{r})|$, etc., to the LDA. In practice, the inclusion of low-order gradient corrections almost never improves on the LDA, and often even worsens it. Moreover higher-order corrections are exceedingly difficult to calculate and little is known about them. It was realized that instead of power-series-like systematic gradient expansions one could experiment with more general functions of $n(\mathbf{r})$ and $|\nabla n(\mathbf{r})|$, which need not proceed order by order. Such functionals, of the general form

$$E_{XC}^{GGA} = \int \epsilon_{XC}(n, |\nabla n|, \nabla^2 n) d\mathbf{r} \tag{2.23}$$

are known as generalized-gradient approximations (GGAs). The current GGAs seem to give reliable results for all main types of chemical bonds and are popular in computational chemistry. We have used the Perdew-Burke-Ernzerhof (PBE) version of GGA [34] in this work.

The hybrid functional:

The LDA or GGA approximation predict the structural properties such as lattice constants and bulk moduli with good accuracy. However, the LDA or GGA results for electronic properties such as band gaps are of much lower

quality. The band gaps are typically underestimated by 50-100 %. Further improvements in the description of band gaps is achieved by the introduction of so-called hybrid functionals which are obtained by admixing a fixed amount of the Hartree-Fock (HF) exchange to the GGA functional. The hybrid functional proposed by Heyd, Scuseria and Ernzerhof termed as HSE06 functional [35, 36] fulfills the need for a universally applicable method that is computationally feasible for a wide range of systems and nowadays becomes a popular choice for calculating the structural properties and the band gaps. The exchange potential employed in HSE06 is divided into short- and long-range parts, and HF exchange is mixed with Perdew-Burke-Ernzerhof (PBE) exchange in the short-range part. To avoid the expensive calculation of long-range HF exchange as well as enabling hybrid DFT calculations on metal elements for which conventional HF or global hybrid calculations are intractable, this term is replaced by long-range PBE exchange, as shown in the following equation

$$E_{XC}^{HSE} = \frac{1}{4}E_X^{HF,sr}(\mu) + \frac{3}{4}E_X^{PBE,sr}(\mu) + E_X^{PBE,lr}(\mu) + E_C^{PBE} \tag{2.24}$$

where (sr) and (lr) refer to the short- and long-range parts of the respective exchange interactions, and μ is the parameter that defines the range separation of the Coulomb kernel which varies between 0.2 and 0.3 $Å^{-1}$. The HSE06 functional yields excellent results, in molecules and solids, for many different properties. The lattice parameters, bulk moduli, heats of formation, binding energies and the band gaps for semiconductors and insulators are accurately described. Thus in contrast to LDA or GGA which typically underestimate the band gap, HSE06 can be employed for both the structural and electronic properties. The improvements in the band gap with HSE06 can be attributed to the admixing of HF exchange [36] and the HSE06 functional just gives the right balance of exchange contribution. However, it should be noted that HSE06 results are not entirely satisfactory. The proposed 25% admixing of HF exchange is not a generic feature for all systems. For example, in the case of ZnO, 37.5% admixing of HF exchange is required to obtain the experimental band gap using the HSE06 functional [37]. Thus the HF exchange is used as a parameter in HSE06 functional and needs to be adjusted to obtain the correct band gap. Thus, in principle, HSE06 can not be treated as an *ab initio* method which accurately describes the electronic properties. We have used HSE06 to calculate the formation energy of point defects in TCOs.

2.3 Computation on solids: electronic band structure

Real crystalline solids contain roughly 10^{24} electrons and ions per cm^3 and in principle all of these should be considered to construct the Kohn-Sham Hamiltonian. This is computationally an impossible task. Thus to solve the problem at hand, the periodicity of the solids crystal structure must be used. The periodic symmetry of the crystal lattice allows to reduce the problem to only those electrons and ionic cores that are contained in the unit cell, which forms the smallest repeat unit. Thus by solving the Kohn-Sham Hamiltonian for the atoms in the unit cell, one can calculate the electron eigenstates for solid. The effective potential, V_{eff}, in the Kohn-Sham equation will now be periodic i.e. $V_{eff}(\mathbf{r}) = V_{eff}(\mathbf{r} + \mathbf{R})$ for all lattice vectors $\mathbf{R}$ of the crystal.

Bloch's theorem says that the eigenstates ϕ of a one-particle Hamiltonian can be written as the product of a plane wave and a lattice-periodic function, i.e.

$$\phi_{n\mathbf{k}}(\mathbf{r}) = e^{i\mathbf{k}\cdot\mathbf{r}} u_{n\mathbf{k}}(\mathbf{r}) \tag{2.25}$$

where $\mathbf{k}$ is the wavevector labeling the wavefunction and can be chosen in the first Brillouin zone due to the translational symmetry, and n is the band index which labels the different solutions for a given $\mathbf{k}$. Here $u_{n\mathbf{k}}$ is a function with the periodicity of the lattice i.e.

$$u_{n\mathbf{k}}(\mathbf{r}) = u_{n\mathbf{k}}(\mathbf{r} + \mathbf{R}) \tag{2.26}$$

If $E_{n\mathbf{k}}$ is an energy eigenvalue, then $E_{n\mathbf{k}+\mathbf{G}}$ is also an eigenvalue for all vectors $\mathbf{G}$ of the reciprocal lattice, i.e.

$$E_n(\mathbf{k}) = E_n(\mathbf{k} + \mathbf{G}) \tag{2.27}$$

Thus the energy values are periodic in reciprocal space.

Using Bloch's theorem the problem of infinitely many-electrons has been turned into a problem of infinitely many k-points inside the first Brillouin zone. Since the wavefunctions of closely located k-points are almost identical, a small region can be sampled by one single k-point and the electronic part of the total energy can thus be calculated, to a good approximation, using only a discrete number of k-points. Different schemes exist to sample appropriately the Brillouin zone with a set of k-points that will give the best estimate of the full integral. In this thesis, we use the k-point sampling scheme as proposed by Monkhorst-Pack [38].

2.4 Methods for electronic structure calculations

In this section we will briefly discuss the three most popular methods that are used to calculate the electronic band structure of TCOs. These are (i) pseudopotentials in combination with the plane wave basis set (ii) the linearized augmented plane wave (LAPW) method and (iii) the projector augmented wave (PAW) method.

2.4.1 Plane wave pseudopotential method

Plane waves offer a natural choice as a basis set to expand the periodic functions $u_{n\mathbf{k}}(\mathbf{r})$ as

$$u_{n\mathbf{k}}(\mathbf{r}) = \sum_{\mathbf{G}} c_{n\mathbf{k},\mathbf{G}} e^{i\mathbf{G}\cdot\mathbf{r}} \tag{2.28}$$

where the summation is over all the reciprocal lattice vectors $\mathbf{G}$ of the system under study. Thus the electronic wave functions can be written as

$$\phi_{n\mathbf{k}}(\mathbf{r}) = \sum_{\mathbf{G}} c_{n\mathbf{k},\mathbf{G}} e^{i(\mathbf{k}+\mathbf{G})\cdot\mathbf{r}}. \tag{2.29}$$

The electronic wavefunctions at each k-point are now expressed in terms of a discrete plane wave basis set. In principle this Fourier series is infinite. However, in practice we cannot work with an infinite basis set, it has to be truncated. The number of plane waves can be restricted by placing an upper boundary to the kinetic energy of the plane waves. This boundary is called energy cut-off E_{cut} and only plane-waves satisfying the condition

$$\frac{|\mathbf{k}+\mathbf{G}|^2}{2} < E_{cut} \tag{2.30}$$

are considered in the computation.

With DFT the complexity of the problem has reduced appreciably. However, for systems with a large number of electrons, it still remains computationally very expensive. Pseudopotentials helped in a crucial way to make the calculations tractable. Using the fact that the physical properties of solids depend mainly on valence electrons, the computational effort can be minimized considerably. In the pseudopotential approximation, the core electrons are removed and the strong ionic potential is replaced by the weaker pseudo potential (V_{pseudo}) that acts on a set of pseudo wave functions (Ψ_{pseudo}) rather than the true valence wave functions (Ψ). The pseudopotential and pseudo wave functions are generated in such a way that they are identical to the

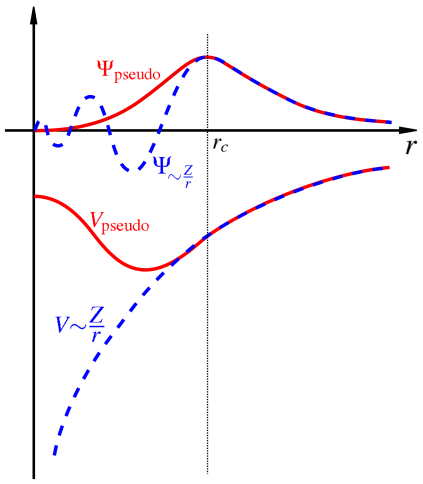

Figure 2.1: Schematic representation of pseudopotential and the pseudo wave function.

true potential and wave function beyond a certain radius known as *cut-off* radius (r_c). In the core region the pseudo wave function is constructed such that all the nodes are removed but the norm is conserved. Also since the nodes of the core states are removed, the number of plane-wave basis functions required to describe this wave function in the core region is much less resulting in reduced computational effort. This leads to a popular plane wave pseudopotential method for electronic structure calculations. For better understanding of this subject the reader may refer to following articles and books [27, 29, 30, 39]. There are several ways to construct a pseudopotential. In this work we have used the OPIUM [40] pseudopotential generator and the details of the pseudopotentials used are described in the successive chapters.

In this thesis we use this method to calculate the DFT band structure and quasiparticle correction to the band gap within the GW approximation for TCO materials. These calculations are performed using the ABINIT code.

2.4.2 All-electron methods

It is possible to solve the Kohn-Sham equations by avoiding an artificial core-valence separation of electrons, as described by the pseudopotential. Such methods are called *all-electron* methods in which all the electrons are explicitly used in the computation.

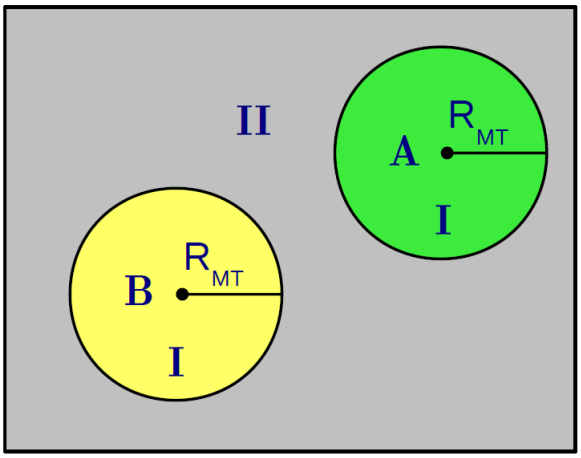

Figure 2.2: Schematic division of unit cell containing two types of atoms A and B, in Muffin-Tin spheres (I) and an interstitial region (II).

Augmented plane wave method (APW)

The APW method uses a plane wave basis set which is especially modified to solve the problem. This adaptation is achieved by dividing the unit cell into (I) non-overlapping atomic spheres (centered at the atomic sites), also known as the Muffin-Tin spheres, and (II) an interstitial region. This is schematically illustrated in Fig. 2.2 with a unit cell containing two types of atoms: A and B. For the two regions, the electron potential $V(\mathbf{r})$ is expanded as

$$V(\mathbf{r}) = \begin{cases} \sum_{lm} V_{lm}(r) Y_{lm}(\hat{\mathbf{r}}) & (\mathbf{r} \in MT) \\ \sum_{\mathbf{G}} V_{\mathbf{G}} e^{i\mathbf{G}\cdot\mathbf{r}} & (\mathbf{r} \in I) \end{cases} \tag{2.31}$$

In the two types of regions different basis sets are used:

$$\phi_{\mathbf{k}_n}^{APW}(\mathbf{r}, \epsilon_l) = \begin{cases} \sum_{lm} A_{lm,\mathbf{k}_n} u_l(r, \epsilon_l) Y_{lm}(\hat{\mathbf{r}}) & (\mathbf{r} \in MT) \\ \frac{1}{\sqrt{V}} e^{i\mathbf{k}_n\cdot\mathbf{r}} & (\mathbf{r} \in I) \end{cases} \tag{2.32}$$

where $\mathbf{k}_n = \mathbf{k} + \mathbf{G}_n$; $\mathbf{G}_n$ are the reciprocal lattice vectors, $\mathbf{k}$ is the wave vector inside the first Brillouin zone and V is the volume of unit cell.

In the atomic spheres (MT), the wave functions are expanded by radial functions times spherical harmonics. $u_l(r, \epsilon_l)$ is the (at the origin) regular solution of the radial Schrödinger equation for a spherical potential $V(r)$ for energy ϵ_l,

$$-\frac{1}{r^2}\frac{d}{dr}(r^2\frac{du_l}{dr}) + [\frac{l(l+1)}{r^2} + V(r) - \epsilon_l] r u_l = 0 \tag{2.33}$$

In the interstitial region (I) plane waves are instead used to build the wave function. The coefficients A_{lm} in the atomic sphere expansion are determined by requiring that the wave functions in the MT and the interstitial regions match each other at the MT boundary.

Thus, each plane wave is augmented by an atomic-like function in every atomic sphere and constitutes thus the basis set used to expand the Kohn-Sham wave function (ψ),

$$\psi_{\mathbf{k}}(\mathbf{r}) = \sum_n c_n \phi_{\mathbf{k}_n}(\mathbf{r}) \tag{2.34}$$

The disadvantage in the APW method is that it can not get the eigenvalues from a single diagonalization due to the unknown parameter ϵ_l in Eq.(2.32). The exact ϵ_l value is needed to describe the eigenstate $\psi_{\mathbf{k}}(\mathbf{r})$ accurately. Since this energy depends on the function $u_l(r, \epsilon_l)$, the resulting eigenvalue problem is non-linear in energy. Thus it needs to be solved self-consistently which makes the APW method computationally inefficient.

Linearized Augmented Plane Wave (LAPW) method

In order to overcome the non-linearity problem in the APW method, the LAPW method was developed. The radial wavefunction can be expanded in a Taylor series expansion around ϵ_l as

$$u_l(r, \epsilon_l) = u_l(r, \epsilon_l^1) + (\epsilon_l - \epsilon_l^1)\dot{u}_l(r, \epsilon_l^1) + O((\epsilon_l - \epsilon_l^1)^2) \tag{2.35}$$

where $\dot{u}_l = \partial u_l / exp \partial \epsilon_l$. In this case the radial function error is second order and the energy error is of fourth order. When ϵ_l^1 is set near ϵ_l the radial function and energy errors are negligible. Thus the LAPW basis set can be defined as

$$\phi_{\mathbf{k}_n}^{LAPW}(\mathbf{r}) = \begin{cases} \sum_{lm}[A_{lm,\mathbf{k}_n} u_l(r, \epsilon_l) + B_{lm,\mathbf{k}_n}\dot{u}_l(r, \epsilon_l)]Y_{lm}(\hat{\mathbf{r}}) & (\mathbf{r} \in MT) \\ \frac{1}{\sqrt{V}} e^{i\mathbf{k}_n \cdot \mathbf{r}} & (\mathbf{r} \in I) \end{cases} \tag{2.36}$$

In the interstitial region, the basis set is the same as in the APW method, but in the Muffin-Tin spheres, the basis functions not only depend on u_l, but also on its energy derivative, $\dot{u}_l$. Thus LAPW method offers more flexibility than the APW method in the Muffin-Tin spheres. Now, it is not important to know the exact value of ϵ_l. For a fixed value of ϵ_l^1, the modified basis functions provide the extra flexibility to cover a large energy region around this linearization energy. The coefficients A_{lm} and B_{lm} are determined by requiring that this basis function matches (in value and slope) each plane wave (PW) which is the corresponding basis function of the interstitial region.

The APW+lo method

Another efficient way to linearize the APW method is achieved by the introduction of local orbitals (lo). The basis set of the introduced APW+lo method is also energy independent and still has the same basis size as the original APW method. To allow enough variational flexibility local orbitals are added, which are defined as

$$\phi_{lm}^{lo}(\mathbf{r}) = \begin{cases} [A_{lm}u_l(r,\epsilon_l) + B_{lm}\dot{u}_l(r,\epsilon_l)]Y_{lm}(\hat{\mathbf{r}}) & (\mathbf{r} \in MT) \\ 0 & (\mathbf{r} \in I) \end{cases} \tag{2.37}$$

The two coefficients A_{lm} and B_{lm} are determined by normalization and by the condition that the local orbital is zero at the Muffin-Tin boundary. The advantage of the APW+lo method is that it has a small basis set like the APW method but with the same accuracy compared to the LAPW method.

The APW+lo method is used to calculate the band structure of prototype TCOs using the recently proposed Tran-Blaha modified Becke-Johnson potential scheme as implemented in the WIEN2k code.

2.4.3 Projector augmented wave method

An approach that lies half-way between the LAPW and the pseudopotential methods has been introduced by Blöchl [41] known as the projector augmented waves (PAW) method. This approach retains the all-electron character, but it uses a decomposition of the all-electron wave function in terms of a smooth pseudo-wave function, and a rapidly varying contribution localized within the core region. The true and pseudo-wave functions are related by a linear transformation:

$$|\Psi_n^{AE}\rangle = |\Psi_n^{PS}\rangle + \sum_i (|\phi_i^{AE}\rangle - |\phi_i^{PS}\rangle)\langle p_i^{PS}|\Psi_n^{PS}\rangle \tag{2.38}$$

The pseudo-wave functions Ψ_n^{PS}, where n is the band index, are the variational quantities and are expanded in plane waves. In the regions between the PAW spheres surrounding the atoms, the Ψ_n^{PS} are identical to the AE wave functions Ψ_n^{AE}, but inside the spheres Ψ_n^{PS} are only a bad approximation to the exact wave functions, they are used only as a computational tool. The AE partial waves ϕ_i^{AE} are solutions of the spherical scalar-relativistic Schrödinger equation for a non spin-polarized atom at a reference energy ϵ_i in the valence regime and for an angular momentum l_i,

$$\Big(-\frac{1}{2}\nabla^2 + \nu_{eff}^{AE}\Big)|\phi_i^{AE}\rangle = \varepsilon_i|\phi_i^{AE}\rangle \tag{2.39}$$

where ν_{eff}^{AE} is the spherical component of the AE potential. The index i contains the reference energy ε_i, the angular momentum quantum numbers (l_i,m_i), and the atomic coordinates $\mathbf{R}_i$. The PS partial waves ϕ_i^{PS} are nodeless and identical to the AE partial wave outside a core radius r_c (approximately equal to half the nearest-neighbor distance) and match continuously to ϕ_i^{PS} inside these spheres.

The projector functions p_i^{PS} are constrained to be dual to the partial waves, they are constructed by a two-step procedure: First, intermediate functions χ_i are computed via

$$|\chi_i\rangle = \left(\varepsilon_i + \frac{1}{2}\nabla^2 - \nu_{eff}^{PS}\right)|\phi_i^{PS}\rangle \tag{2.40}$$

where ν_{eff}^{PS} is the spherical component of the effective pseudopotential, which can be chosen arbitrarily inside the radius r_c but must match ν_{eff}^{AE} for $r \geq r_c$. The projector functions are linear combinations of the χ_i with

$$|\phi_i^{PS}\rangle = \sum_j (B^{-1})_{ji}|\chi_j\rangle, B_{ij} = \langle\phi_i^{PS}|\chi_j\rangle \tag{2.41}$$

such that the ϕ_i^{PS} and p_i^{PS} are dual, $\langle p_i^{PS}|\phi_j^{PS}\rangle = \delta_{ij}$ and $\langle r|p_i^{PS}\rangle = 0$ for $r > r_c$.

The PAW method, as implemented in the VASP code, is used to calculate the formation energies of native point defects in $ZnAl_2O_4$ spinel which are discussed in the last chapter in this thesis.

2.5 The band gap problem in DFT

DFT is an *ab initio* method which is routinely used to calculate the electronic structure of atoms, molecules and solid. It serves as the workhorse technique in quantum mechanical description of materials. The key quantity in DFT is the electron density from which all ground-state properties can be determined. It gives direct access to forces and stresses allowing a structural relaxation of the system. The lattice parameters and atomic positions are accurately predicted with a systematic error of $<$ 1-5%, depending on the type of exchange-correlation functional used. However the efficiency of DFT in describing and predicting the excitation energies and the band gaps is not that good. The band gaps calculated within DFT show a severe underestimation compared to experiment as evident from Fig. 2.3.

The underestimation of the band gap is, however, not surprising. The Kohn-Sham eigenvalues ϵ_i from DFT are completely artificial objects. These are the eigenvalues of a non-interacting system chosen to yield the same

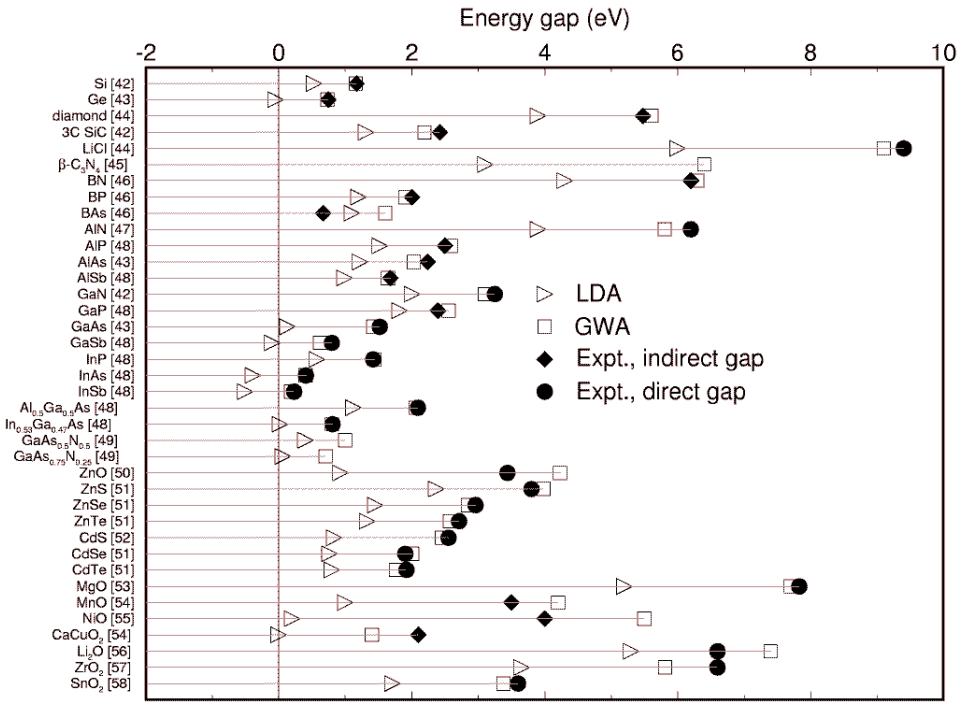

Figure 2.3: Comparison between the experimental gap and the gap calculated using DFT-LDA for semiconductors and insulators [from Ref. [23]].

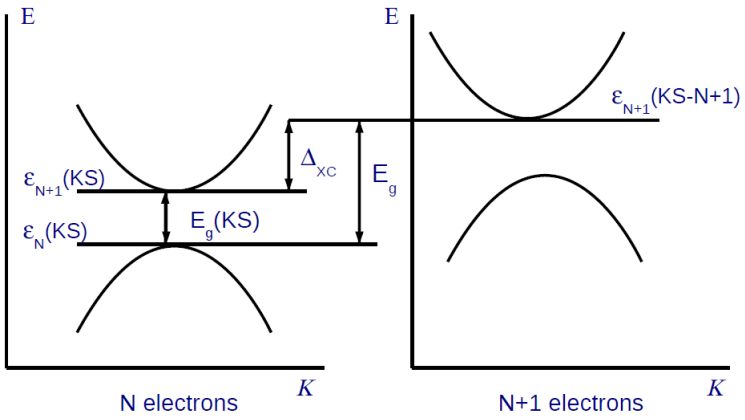

Figure 2.4: Schematic illustration of the experimental band gap and Kohn-Sham gap.

density as the many-body interacting system. There is no physical basis to interpret the Kohn-Sham gaps as the real experimental gaps. However, in practice, such a comparison is motivated by the close resemblance observed between the Kohn-Sham band structure and the real band structure for many systems. The band dispersion shows a good agreement with the experiments.

The band gaps, E_g, of semiconductors are differences of ground-state energies (E) of N and $N \pm 1$ particle systems:

$$E_g = E(N+1) + E(N-1) - 2E(N) = I - A \tag{2.42}$$

where I represents the ionization potential and A represents the electron affinity of the system. In particular, the lowest conduction band energy is given by $\epsilon_c = E_{N+1} - E_N$ and highest valence band energy corresponds to $\epsilon_v = E_N - E_{N-1}$. Similar to metals, the highest "occupied "eigenenergy for the N-electron system $\epsilon_N(N)$ is the Fermi energy and thus $\epsilon_c = \epsilon_{N+1}(N+1)$, $\epsilon_v = \epsilon_N(N)$. Hence, the energy gap is related to the eigenenergies as -

$$E_g = \epsilon_{N+1}(N+1) - \epsilon_N(N) \tag{2.43}$$

It is different from the naive definition of the band gap in terms of only N-particle eigenenergies given by

$$\epsilon_g = \epsilon_{N+1}(N) - \epsilon_N(N) \tag{2.44}$$

This deviation is given by

$$\Delta_{XC} = \epsilon_{N+1}(N+1) - \epsilon_{N+1}(N) \tag{2.45}$$

and corresponds to the neglected derivative discontinuity Δ_{XC} by the standard local and semi-local exchange-correlation functionals [19, 20, 21, 22]. It is illustrated schematically in Fig. 2.4. Δ_{XC} is given by

$$\Delta_{XC} = \lim_{\eta \to 0} \left(\frac{\delta E_{XC}}{\delta n(\mathbf{r})}\Big|_{N+\eta} - \frac{\delta E_{XC}}{\delta n(\mathbf{r})}\Big|_{N-\eta} \right) \tag{2.46}$$

To calculate Δ_{XC}, DFT had to be extended to describe systems with fractional number of particles $N \pm \eta$ [19]. The evaluation of $\delta E_{XC}/\delta n(\mathbf{r})$ at $N \pm \eta$ ensures that the discontinuity at integer particle number N is captured. Depending on the approximation used for E_{XC} the results differ strongly. For LDA and all GGAs, $\Delta_{XC} = 0$. Therefore, the fundamental gap is given solely by the Kohn-Sham gap which is always underestimated compared to the experiment.

Chapter 3

Electronic band structure of prototype TCOs with DFT

3.1 Introduction

In this chapter, we present the electronic band structure of prototype TCOs. The calculations are performed using LDA within DFT. As stated earlier, In_2O_3, SnO_2, ZnO and CdO form a basic set of TCO host materials from which the commonly used binary, ternary and multicomponent systems are derived. These prototype binary oxides show n-type conductivity. The experimental band gap and electron effective mass of these binary oxides are listed in Table 3.1. The In_2O_3, SnO_2, and ZnO have a band gap > 3 eV, indicating transparency for visible part of electromagnetic spectrum. CdO has lower band gap, but it also has lower electron effective mass leading to higher charge carrier mobility and is thus useful in certain applications.

Table 3.1: Optical band gap and electron effective mass (in units of the electron mass, m_e) of basic binary TCOs.

Oxide	Band gap (eV)	Effective mass
In_2O_3	3.10	0.30 m_e
ZnO	3.44	0.32 m_e
SnO_2	3.60	0.29 m_e
CdO	1.2 - 2 (indirect)	0.21 m_e
	2.32 (indirect)	

The bulk crystal structures of these binary oxides are shown in Fig. 3.1. Each of these systems possesses a distinct crystal structure. In_2O_3 has body

centered cubic (bcc) bixbyite structure, ZnO has a hexagonal close packed (hcp) wurtzite structure, CdO crystallizes in the face centered cubic (fcc) rocksalt structure and SnO_2 adopts the rutile crystal structure.

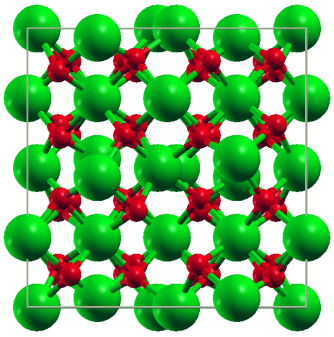

In_2O_3 - bixbyite
($Ia\bar{3}$, # 206)

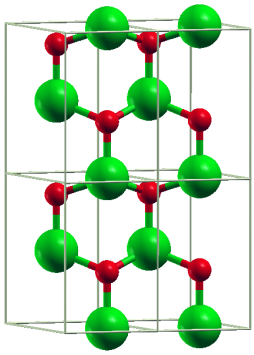

ZnO - wurtzite
($P6_3mc$, # 186)

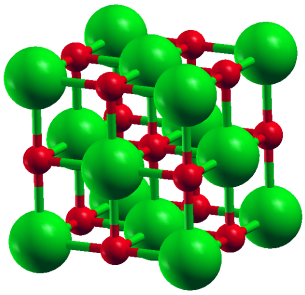

CdO - rocksalt
($Fm\bar{3}m$, # 225)

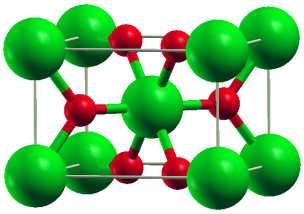

SnO_2 - rutile
($P42/mnm$, # 136)

Figure 3.1: Crystal structure of basic binary oxides, green color is for the cation while red shows the oxygen atoms.

3.1.1 Computational details

The electronic structure has been calculated using the plane wave pseudopotential code ABINIT [24, 25, 26]. For the electronic structure the plane wave cutoff is chosen using the total energy convergence criterion of 1×10^{-3} mHa. The atomic positions and structural parameters have been optimized by calculating the Hellmann-Feynman forces. The stresses are optimized with the criterion of 1×10^{-5} eV/Å^3. A regular $4 \times 4 \times 4$ Monkhorst-Pack [38] k-point mesh is used for cubic structures such as In_2O_3 and CdO, while for the

hexagonal and rutile structure we choose $3 \times 3 \times 2$ Monkhorst-Pack k-point mesh. The unit cell contains 4, 2, 6 and 40 atoms for hexagonal, rocksalt, rutile and bixbyite structures respectively.

The valence configuration of a Zn atom is $4s^2$, while that of an O atom is $2s^2$, $2p^4$. However it is essential to include the *semi-core* Zn 3-d orbitals in the valence because the localized 'd' orbitals play an important role in bonding. Therefore their inclusion as the valence orbital is essential for a correct description of structural properties [42]. This leads to a 12-electron pseudopotential for Zn [Ar] $3d^{10}$ $4s^2$. Similarly, the *semi-core* d orbital is also included in the valence for Cd and In atoms. All the pseudopotentials used in this chapter are obtained from the ABINIT pseudopotential repository and they are LDA pseudopotentials using the Trouiller-Martins scheme, generated with the help of the FHI code [43].

3.2 Zinc oxide

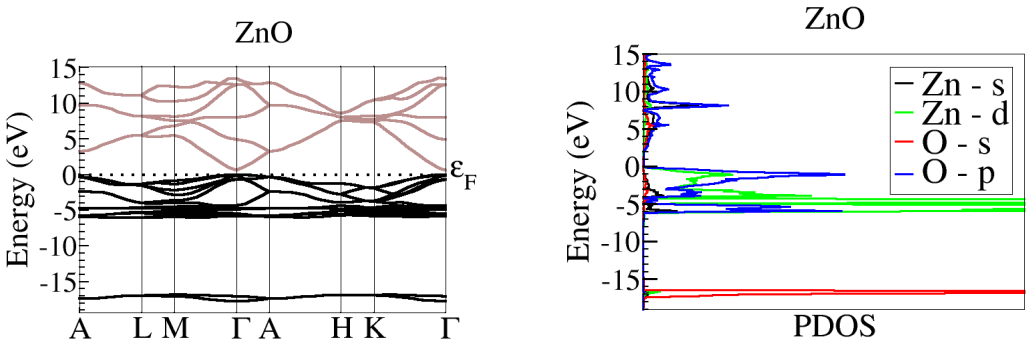

Figure 3.2: Electronic band structure of ZnO calculated using LDA within DFT.

ZnO is a material that has been widely studied. Many first principles calculations of ZnO have been published, focusing in particular on the electronic and structural properties. ZnO has a wide range of applications that exploit its electronic, optical and piezoelectric properties [44]. The ground-state, ZnO adopts the hexagonal wurtzite (wz) crystal structure (space group $P6_3mc$) with lattice constants of a = 3.25 Å and c = 5.207 Å. The Zn and O atoms are tetrahedrally coordinated. It also has other stable polymorphs including the zincblende and rocksalt (under high pressure) structure. The experimen-

tal electronic band gap of wz-ZnO is 3.44 eV [45], which is direct in nature.

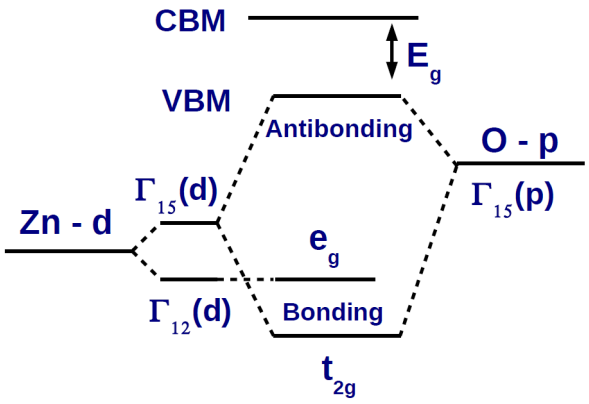

Figure 3.3: Schematic plot of p-d hybridization.

The calculated DFT band structure and projected density of states (PDOS) for the wurtzite ZnO are shown in Fig 3.2. The valence band maximum (VBM) is aligned at 0 eV in both plots. The projected density of states clearly shows significant p-d (O-2p and Zn-3d) hybridization in the range of 0 to -6 eV. The Zn-3d derived bands are split into two groups which are triply and doubly degenerate at Γ. The upper doubly degenerate (e_g) band around -4.9 eV shows strong 'd' character while the lower triply degenerate (t_{2g}) band around -6.2 eV. The semicore 'd' states of Zn have a relatively high energy in the band structure compared to the experimental value of -8.81 eV[46]. As illustrated schematically in Fig. 3.3, the Zn-d ($\Gamma_{15}(d)$) orbitals can couple with the O-p ($\Gamma_{15}(p)$) orbitals. This p-d repulsion results in upward movement of the valence band. While LDA is known to underestimate the band gap severely, it is even worse for ZnO due to this strong p-d hybridization [48]. The calculated Kohn-Sham gap of ZnO is 0.79 eV and is direct in nature.

3.3 Cadmium oxide

CdO is unusual among the IIB-VI binary compound semiconductors as it exists solely in a face-centered-cubic rocksalt structure which is more typical of the ionic insulators. All other Cd and Zn oxides and chalcogenides crystallize in either the cubic zinc-blende or the hexagonal wurtzite structure in

which the metal is tetrahedally coordinated. In CdO the metal cation is octahedrally coordinated [47]. The octahedral point group (O_h) of the rocksalt structure contains an inversion center at the Γ point[48]. As a consequence CdO has an indirect band gap which is explained in the following. The '*p*' and '*d*' states belong to a different representation at the Γ point in the rocksalt structure and do not mix. However at other points with lower symmetry, the 'p' and 'd' states can mix in the Brillouin zone. Thus in the case of CdO, the hybridization of O-2*p* derived orbitals with the Cd-4*d* states combined with the octahedral point symmetry leads to an indirect band gap.

The calculated band structure of CdO is shown in Fig 3.4. The LDA band structure shows CdO to be *semi-metallic* since the conduction band minimum (CBM) crosses the Fermi energy level (E_f). The VBM occurs along Γ-L and midway along Γ-K direction. The PDOS plot of CdO also show a strong *p*-*d* hybridization, similar to ZnO. The Cd-*d* energy levels around ∼-6.5 eV are at higher binding energy compared to the experimental result of -8.8 eV below VBM.

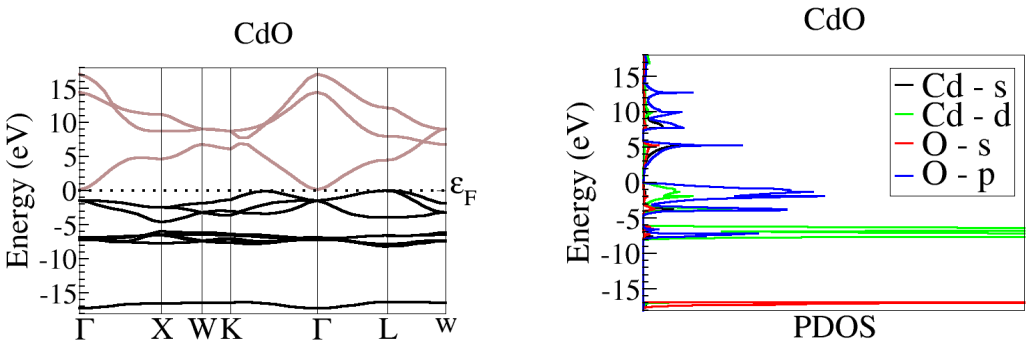

Figure 3.4: Electronic band structure of CdO calculated using LDA within DFT.

3.4 Tin dioxide

SnO_2 exists in the rutile crystal structure. The lattice constants are $a = b = 4.7374$ Å and $c = 3.1864$ Å [49]. In the bulk all Sn atoms are sixfold coordinated to threefold coordinated oxygen atoms.

The band structure shown in Fig. 3.5 yields a direct band gap of 1.18 eV for LDA. The valence bands in the range of 0 to -7 eV are composed of

mainly O-2p and admixture of Sn-4p,d orbitals, as evident from the PDOS presented. The CBM has Sn-4s character at the high symmetry Γ point. There is also hybridization between Sn-4d and O-2s orbitals for the lowest valence bands between -16 to -19 eV. These Sn-4d states are at lower binding energy in comparison with reported experimental values of 21.1 - 21.4 eV [50].

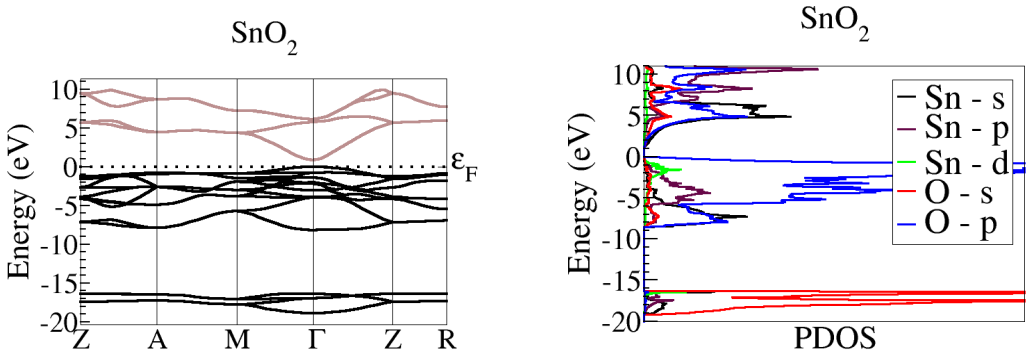

Figure 3.5: Electronic band structure of SnO_2 calculated using LDA within DFT.

3.5 Indium oxide

In_2O_3 is widely used TCO and it adopts the body-centered cubic (bcc) bixbyite lattice (space group $Ia\bar{3}$) with 8 formula units per primitive cell. Each In atom is coordinated by six oxygen atoms in a distorted octahedron. The unit cell contains 40 atoms and has lattice constant a = 10.117 Å [51].

The band structure along high symmetry lines in the Brillouin zone calculated with LDA is presented in Fig. 3.6. It shows that In_2O_3 is a direct band gap semiconductor. Although the widely quoted direct band gap of In_2O_3 is 3.75 eV and indirect gap is 2.62 eV, recent experimental reinvestigation along with theoretical studies have concluded In_2O_3 to be a direct band gap semiconductor with a band gap $\sim$ 3.1 eV [52]. The LDA band gap of 1.18 eV is consistent with earlier reported results [53]. The band structure details for In_2O_3 are more complex due to the hybridization between different atomic orbitals as is evident from the PDOS plot. For instance, the CBM at Γ starts with pure In-4s character but later mixes with the In-5p character with increasing '**k**' vector away from the Γ point. The upper part of the

valence band shows mostly O-2p character and has a bandwidth of about 6 eV. The In-4d related bands lie in the energy range of -11 to -13 eV and the lowest valence band are O-2s derived. The VBM is also influenced by the hybridization between the O-2p and In-4d orbitals.

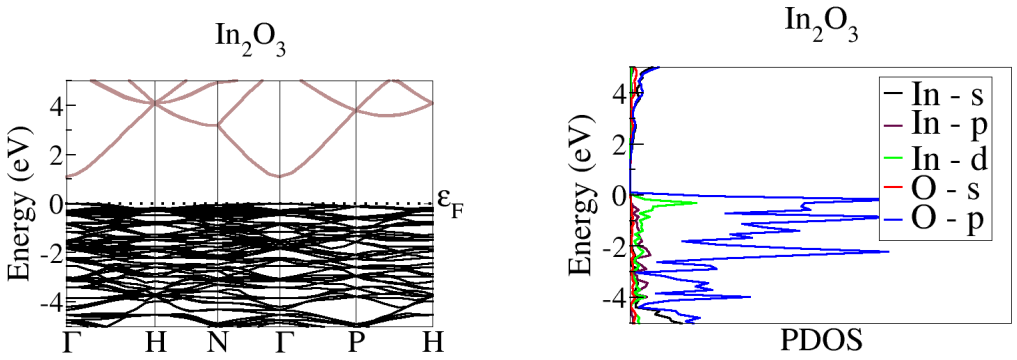

Figure 3.6: Electronic band structure of In_2O_3 calculated using LDA within DFT.

3.6 Summary

3.6.1 Structural properties

Table 3.2: Structural properties : experimental and optimized lattice parameters.

Oxide	Experiment (in Å)	Optimized (in Å)	Percentage error
In_2O_3	a=b=c=10.118	a=b=c=10.351	$\sim$ 1 %
ZnO	a=b=3.258	a=b=3.283	$\sim$ 1 %
	c=5.220; u=0.382	c=5.309; u=0.3759	
SnO_2	a=b=4.789	a=b=4.789	$\sim$ 1 %
	c=3.188; u=0.3059	c=3.220; u=0.3065	
CdO	a=b=c=4.779	a=b=c=4.825	$\sim$ 1 %

The experimental and theoretically optimized lattice constants along with the internal parameter ('u') of binary oxides are listed in the Table 3.2. The

optimized lattice constants are in agreement with the experimental counterparts. The percentage error involved in the estimation of the lattice constant is less than 1%.

3.6.2 Electronic properties

Table 3.3: The experimental and calculated band gap using DFT (in eV).

Oxide	Experiment	DFT	Percentage error
In_2O_3	3.10	1.10	$\sim$ 65 %
ZnO	3.44	0.78	$\sim$ 77 %
SnO_2	3.60	1.13	$\sim$ 68 %
CdO	1.2-2 (indirect)	-0.28	
	2.32 (direct)	0.80	$\sim$ 55 %

Table 3.4: The electron effective mass (in units of the electron mass, m_e) for prototype binary oxides.

Oxide	m_e^{LDA}	$m_e^{Expt.}$
In_2O_3	0.22	0.30
ZnO	$m_{\parallel} = 0.23$	0.32
	$m_{\perp} = 0.14$	
CdO	0.16	0.21
SnO_2	$m_{\parallel} = 0.17$	0.29
	$m_{\perp} = 0.29$	

A common feature observed in the electronic band structure of these binary oxides is the highly dispersed conduction band. This high dispersion implies the free electron character of the conduction band and thus these systems are ideal host materials for TCO applications. The calculated band gaps and band mass are listed in the Table 3.3 and 3.4. In_2O_3, ZnO SnO_2 have a direct band gap while CdO has an indirect gap. The band gaps are strongly underestimated with the LDA and this underestimation can be as large as $\sim$77% in case of ZnO. The electron effective mass obtain for each of the binary oxide studied is listed in Table 3.4. Here $m_{\parallel}$ indicates the electron effective

mass calculated parallel to the c-axis while $m_{\perp}$ refers to its value calculated perpendicular to the c-axis. The experimental measurements indicate that the band mass is $\sim 0.3\ m_e$ for these oxides except CdO which has even lower band mass ($\sim 0.2\ m_e$). The electron effective mass calculated within LDA is also systematically underestimated compared to the experiment.

However, this underestimation of the band gap is not surprising. It is well known 'band gap problem' in DFT and is discussed earlier in section 2.5. Therefore to calculate the band gap we use the GW approximation to the many body perturbation theory which is introduced in the next chapter.

Chapter 4

GW approximation: an introduction

4.1 Photoelectron spectroscopy

In experiments, the band gap can be measured with photoelectron spectroscopy. Direct photoelectron spectroscopy is a technique in which a photon impinges on the sample and knocks out an electron. The difference between the energy of an incident photon ($\hbar\omega$) and the kinetic energy of an ejected electron (E_{kin}) gives the binding energy of the electron ($\epsilon_i = \mathrm{E}_{kin} - \hbar\omega$, in a state i). In general ϵ_i equals the difference $\epsilon_i = E_0^N - E_i^{N-1}$ between the total energy E_0^N of the N-particle ground state Ψ_0^N and the energy E_i^{N-1} of the $(N-1)$-particle state Ψ_i^{N-1} that remains after the emission. The complementary process of inverse photoemission, on the other hand, involves injection of electrons into the sample. Again the energy difference $\epsilon_i = \mathrm{E}_{kin} - \hbar\omega$ can be identified as the binding energy of the electron. The number of electrons in the system thus increases from N to $N+1$. This is illustrated in Fig. 4.1

Thus a theoretical framework that deals with the change in the particle density from N particles to $N \pm 1$ particles is essential to describe the photoemission process. For this purpose we will make use of many-body perturbation theory. The central variable is the time ordered Green's function $G(\mathbf{r}t, \mathbf{r}'t')$ and in the following sections we will see that it contains the excitation energies ϵ_i and even the excitation lifetimes. Thus the GW approximation (introduced in this chapter) to the many-body perturbation theory offers a strong physical basis to correlate the calculated excitation energies with the band gaps measured with the help of photoelectron spectroscopy.

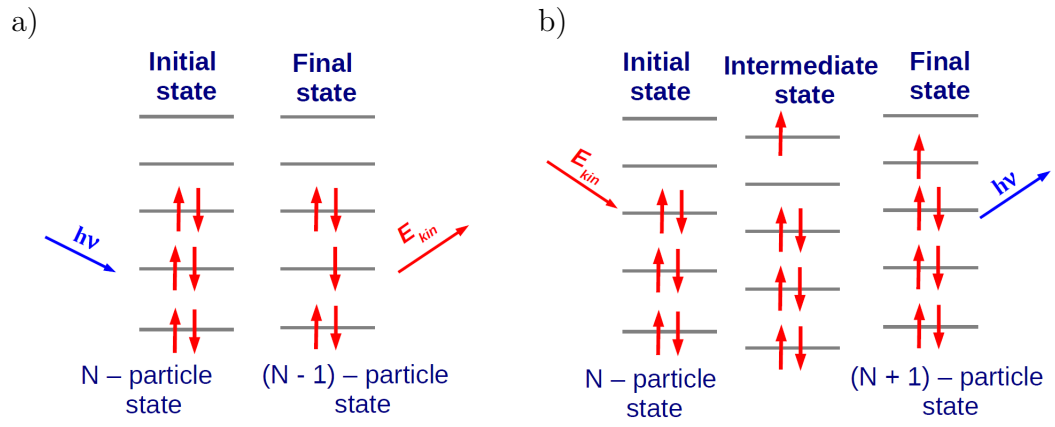

Figure 4.1: Schematic illustration of (a) direct and (b) inverse photoelectron spectroscopy.

4.2 Green's Function

The electron Green's function G describes the evolution of an excitation and is also called the single-particle propagator. The one-electron Green's function is defined as an expectation value with respect to the many-electron ground state $|\Psi_0\rangle$

$$G(\mathbf{r}_1, t_1; \mathbf{r}_2, t_2) = -i\langle\Psi_0|T[\psi(\mathbf{r}_1, t_1)\psi^\dagger(\mathbf{r}_2, t_2)]|\Psi_0\rangle \tag{4.1}$$

where $\psi(\mathbf{r}, t)$ is the field operator in the Heisenberg picture, that is,

$$\psi(\mathbf{r}, t) = e^{i\hat{H}t/\hbar}\psi(\mathbf{r})e^{-i\hat{H}t/\hbar} \tag{4.2}$$

T is the time-ordering operator defined by

$$T[\psi(\mathbf{r}_1, t_1)\psi^\dagger(\mathbf{r}_2, t_2)] = \begin{cases} \psi(\mathbf{r}_1, t_1)\psi^\dagger(\mathbf{r}_2, t_2) & t_1 > t_2 \\ -\psi^\dagger(\mathbf{r}_2, t_2)\psi(\mathbf{r}_1, t_1) & t_1 < t_2 \end{cases} \tag{4.3}$$

In this equation, $\psi^\dagger(\mathbf{r}_2, t_2)|\Psi_0\rangle$ represents an $(N+1)$-electron state in which an electron has been added to the system at point $\mathbf{r}_2$ and time t_2. When $t_2 < t_1$, the many-body Green's function gives the probability amplitude to detect an electron at point $\mathbf{r}_1$ and time t_1 when an electron has been added to the system at point $\mathbf{r}_2$ and time t_2. When $t_2 > t_1$, the Green's function describes the propagation of a many-body state in which one electron has been removed at point $\mathbf{r}_1$ and time t_1, that is, the propagation of a hole.

4.2.1 The Lehmann representation

The Lehmann representation of G gives useful physical information about the charged excitation energies of the many-body system. Moreover, it also helps in finding the connection between many-body theory and DFT. First, recall that if a state $|\Psi\rangle$ is such that $\hat{N}|\Psi\rangle = N|\Psi\rangle$ ($\hat{N}$ is the number operator, $\hat{N} \equiv \psi^\dagger\psi$), then

$$\hat{N}\hat{\psi}(\mathbf{r})|\Psi\rangle = (N-1)\hat{\psi}(\mathbf{r})|\Psi\rangle \tag{4.4}$$

Similarly, $\hat{\psi}^\dagger(\mathbf{r})|\Psi\rangle$ is a state with $N+1$ particles. According to its definition, the Green's function can be written as

$$\begin{aligned} G(\mathbf{r}_1,t_1;\mathbf{r}_2,t_2) = -\frac{i}{\hbar}\Big(&\theta(t_1-t_2)\langle\Psi_0|\psi(\mathbf{r}_1,t_1)\psi^\dagger(\mathbf{r}_2,t_2)|\Psi_0\rangle \\ &-\theta(t_2-t_1)\langle\Psi_0|\psi(\mathbf{r}_2,t_2)\psi^\dagger(\mathbf{r}_1,t_1)|\Psi_0\rangle\Big) \end{aligned} \tag{4.5}$$

Let us consider the first term. If $|\Psi_i\rangle$ is a complete set of Heisenberg states, i.e., a set of solutions to the full Hamiltonian, inserting the closure relation $\sum_i |\Psi_i\rangle\langle\Psi_i| = 1$ between field operators leads to

$$\langle\Psi_0|\psi(\mathbf{r}_1,t_1)\psi^\dagger(\mathbf{r}_2,t_2)|\Psi_0\rangle = \sum_i e^{-i(E_i-E_0)(t_1-t_2)/\hbar}\times\langle\Psi_0|\hat{\psi}(\mathbf{r})|\Psi_i\rangle\langle\Psi_i|\hat{\psi}^\dagger(\mathbf{r}')|\Psi_0\rangle \tag{4.6}$$

Here E_0 is the energy of the (N-particle system) ground state and E_i is the energy of state $|\Psi_i\rangle$. Only states with $N+1$ particles contribute, thus the summation is restricted to these states and we make this explicit by rewriting $|\Psi_i\rangle \to |\Psi_i^{N+1}\rangle$, and $E_i - E_0 \to E_i^{(N+1)} - E_0^{(N)} \equiv \epsilon_i^{(N+1)}$.

We now introduce the frequency-dependent Green's function. First, if the Hamiltonian is time independent, as is the case for the systems we are interested in, one can show $G(\mathbf{r}_1,t_1;\mathbf{r}_2,t_2) = G(\mathbf{r}_1,t_1-t_2;\mathbf{r}_2,0) \equiv G(\mathbf{r}_1,\mathbf{r}_2;t_1-t_2)$ [54]. Then, we define $G(\mathbf{r}_1,\mathbf{r}_2;\omega) = \int_{-\infty}^{\infty} d\tau e^{i\omega\tau}G(\mathbf{r}_1,\mathbf{r}_2;\tau)$. Also, given that the Heaviside function has the representation $\theta(\tau) = (i/2\pi)\int d\omega e^{-i\omega\tau}/(\omega + i\eta)$, it can be shown that the frequency dependence of the Green's function term above is given by

$$\int_{-\infty}^{\infty} d\tau e^{i\omega t}\theta(\tau)e^{-i\epsilon_i^{(N+1)}\tau/\hbar} = i\frac{1}{\omega - \epsilon_i^{(N+1)}/\hbar + i\eta}. \tag{4.7}$$

A similar treatment of the second term in Eq.(4.5) finally leads to

$$\begin{aligned} G(\mathbf{r}_1,\mathbf{r}_2;\omega) = &\frac{1}{\hbar}\sum_i \frac{\langle\Psi_0^{(N)}|\hat{\psi}(\mathbf{r})|\Psi_i^{(N+1)}\rangle\langle\Psi_i^{(N+1)}|\hat{\psi}^\dagger(\mathbf{r}')|\Psi_0^{(N)}\rangle}{\hbar\omega - \epsilon_i^{(N+1)} + i\eta} \\ &+\frac{1}{\hbar}\sum_i \frac{\langle\Psi_0^{(N)}|\hat{\psi}^\dagger(\mathbf{r})|\Psi_i^{(N-1)}\rangle\langle\Psi_i^{(N-1)}|\hat{\psi}(\mathbf{r}')|\Psi_0^{(N)}\rangle}{\hbar\omega - \epsilon_i^{(N-1)} - i\eta} \end{aligned} \tag{4.8}$$

Thus, the poles of the Green's function are the exact excitation energies that correspond to excitations of an $(N-1)$-particle and an $(N+1)$-particle system. These are measured in experiment, such as in photoemission or inverse photoemission which are mentioned earlier. Hence the Green's function offers a strong physical basis to correlate these excitation energies to those processes measured in direct and inverse photoelectron spectroscopy. In the case of semiconductors and insulators, these measurements can yield the VBM and CBM, and thus the band gap value.

4.3 Feynman diagrams

Feynman diagrams offer a convenient way to represent Green functions diagrammatically. At this stage, I will introduce the basic Feynman diagrams that will help to visualize the series of the exchange-correlation interactions in the later sections[1]. Each space time argument $(\mathbf{r}, t)$ corresponds to a node and is represented by a dot ($\bullet$). A zeroth-order Green's function, $G^0(\mathbf{r}_1, t_1; \mathbf{r}_2, t_2)$, is represented diagrammatically as a 'thin' line going from $(\mathbf{r}_2, t_2)$ to $(\mathbf{r}_1, t_1)$:

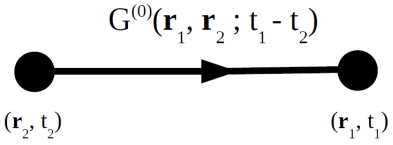

Similarly the fully interacting Green's function (G) are represented by a 'thick' line:

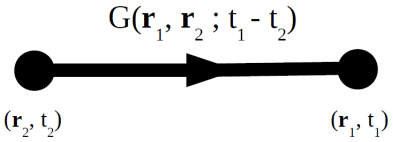

The Coulomb interaction is represented by a dotted line (a wavy line is reserved for the screened interaction):

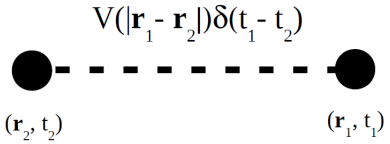

[1] The notation and diagrams are adopted from the lecture notes on the GW approximation, by Dr. Martin Stankovski (UCL, Belgium) at the University of Antwerp in the framework of the European Theoretical Spectroscopy Facility (ETSF).

Here the arrows are absent because the Coulomb interaction is symmetric. A vertex is the point where an interaction line and two Green's functions meet. Using these two graphical components, we can draw all the lines and vertices corresponding to the expansion of the Green's function. The most simple diagrams for the Green's function are the terms to first order in the interaction. It contains all self-energy diagrams with exactly one interaction line, which can be identified by the Hartree term and the exchange term as shown below:

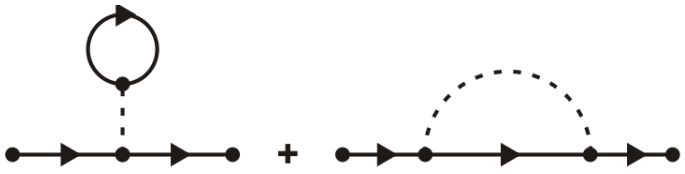

Hartree + Exchange

4.4 The Dyson equation and concept of self-energy

After introducing the Green's function - the question is how to calculate G? There are several ways to tackle the problem, one of which is the equation of motion technique. In this approach, a series of coupled differential equations are generated by differentiating the Green's function a number of times. The many-particle Hamiltonian in the second-quantization formalism is

$$\hat{H} = \sum_{i=1}^{N}(-\frac{1}{2}\nabla_i^2+\nu_{ext}(\mathbf{r}_i))+\frac{1}{2}\sum_{i\neq j}\nu(\mathbf{r}_i,\mathbf{r}_j) = \sum_{i=1}^{N}\hat{h}_0(\mathbf{r}_i)+\frac{1}{2}\sum_{i\neq j}\nu(\mathbf{r}_i,\mathbf{r}_j) \quad (4.9)$$

and can be rewritten in terms of a field operator involving the annihilation and creation operators:

$$\hat{H} = \int \hat{\psi}^\dagger(\mathbf{r})\hat{h}_0(\mathbf{r})\hat{\psi}(\mathbf{r})d\mathbf{r}+\frac{1}{2}\int\int \hat{\psi}^\dagger(\mathbf{r}_1,t)\hat{\psi}^\dagger(\mathbf{r}_2,t)\nu(\mathbf{r}_1,\mathbf{r}_2)\hat{\psi}(\mathbf{r}_2)\hat{\psi}(\mathbf{r}_1)d\mathbf{r}_1d\mathbf{r}_2 \quad (4.10)$$

where we have explicitly separated the one-electron part of the Hamiltonian

$$\hat{h}_0(\mathbf{r}) = -\frac{1}{2}\nabla^2 + \nu_{ext}(\mathbf{r}), \quad (4.11)$$

from the Coulomb interaction. The expression given by Eq.(4.10) is just a mathematical formulation of the initial Hamiltonian, introduced in order to

automatically satisfy the requirement of antisymmetry of the total fermionic wave function. At this stage we introduce following notation. The numbers (e.g. 1) are short hand notation for the position and time variables ($\mathbf{r}_1$,t_1). From the equation of motion for the field operator in the Heisenberg representation:

$$i\frac{\partial\hat{\psi}}{\partial t} = [\hat{\psi}, \hat{H}] \tag{4.12}$$

it is possible to derive the following equation, defining the time-evolution of the Green's function:

$$i\frac{\partial G(1,2)}{\partial t_1} = \delta(1,2) + \hat{h}_0(\mathbf{r})G(1,2) - i\int \nu(1^+,3)G(1,3;2,3^+)d3, \tag{4.13}$$

(here, for example, 1^+ denotes $\mathbf{r}_1, t_1^+$; where $t_1^+ = t_1 + \delta$ and δ is a positive infinitesimal real number) which involves the two-particle Green's function:

$$G(1234) = -\langle\Psi_0^N|\hat{T}\hat{\psi}(1)\hat{\psi}(2)\hat{\psi}^\dagger(4)\hat{\psi}^\dagger(3)|\Psi_0^N\rangle. \tag{4.14}$$

The presence of the two-particle Green's function in Eq.(4.13) complicates the problem, since the knowledge of the time-evolution of a four-point quantity is needed. One might think that it would be possible to obtain a closed expression for the derivative of $G(1,2)$ by analyzing the time evolution of $G(1,2,3,4)$. But unfortunately, the evolution of two-particle Green's function depends on a three-particle Green's function, the evolution of three-particle Green's function requires knowledge of a four-particle Green's function and so on. In order to terminate this iteration scheme (which is as complex as the original problem of solving the Schrödinger equation for the many-electron system), one can use many-body perturbation theory. In order to know the one-particle properties, the knowledge of one-particle Green's function should be sufficient. In order to do that, a suitable expression of the two-particle Greens function in terms of the one-particle one should be found. This is done by introducing the self-energy operator Σ as

$$\int \Sigma(1,3)G(3,2)d3 = -i\int \nu(1^+,3)G_2(1,3,2,3^+)d3, \tag{4.15}$$

so that the time-evolution of the Green's function can be rewritten as

$$\Big[i\frac{\partial}{\partial t_1} - \hat{h}_0(\mathbf{r}_1)\Big]G(1,2) - \int \Sigma(1,3)G(3,2)d3 = \delta(1,2). \tag{4.16}$$

which is the so-called Dyson equation.

This equation can be transformed to the frequency domain with the help of a Fourier transform which yields

$$[\omega - \hat{h}_0(\mathbf{r})]G(\mathbf{r},\mathbf{r}';\omega) - \int \Sigma(\mathbf{r},\mathbf{r}'';\omega)G(\mathbf{r}'',\mathbf{r}';\omega)d\mathbf{r}'' = \delta(\mathbf{r}-\mathbf{r}') \tag{4.17}$$

Finally the insertion of the Green's function in the Lehmann representation leads to the quasiparticle equation

$$\hat{h}_0(\mathbf{r})\psi_i(\mathbf{r}) + \int \Sigma(\mathbf{r},\mathbf{r}';\epsilon_i/\hbar)\psi_i(\mathbf{r}')d\mathbf{r}' = \epsilon_i\psi_i(\mathbf{r}) \tag{4.18}$$

Thus the knowledge of the self-energy operator allows one to describe the quantum-mechanical state of a renormalized electron (quasiparticle) in the many-body system. The quasiparticle wavefunctions and energies can indeed be found by solving the nonlinear system of Eq.(4.18).

These developments can also be applied to the non-interacting fermions, the equation of motion for the non-interacting Green's function (G_0) is

$$\left[i\frac{\partial}{\partial t_1} - \hat{h}_0(\mathbf{r}_1)\right]G_0(12) = \delta(1,2). \tag{4.19}$$

This proves that the non-interacting Green's function is formally the functional inverse of the operator $(\omega - \hat{h}_0)$ in frequency space. Such an interpretation of G_0^{-1} allows one to rewrite the Dyson equation as

$$[G_0^{-1}(1,3) - \Sigma(1.3)]G(3,2) = \delta(1,2). \tag{4.20}$$

Symbolically, the Dyson equation can be written as

$$G = G_0 + G_0\Sigma G \tag{4.21}$$

The self-energy (Σ) thus can be seen as the connection between the non-interacting system (with Green's function G_0) and the interacting one (G). The self-energy accounts for all the exchange-correlation effects of the interacting particles. The Feynman diagrams for the Dyson equation and the self-energy are:

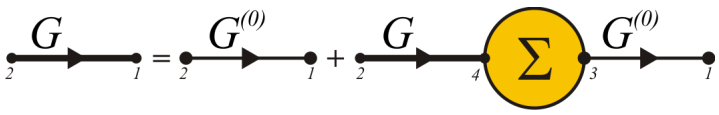

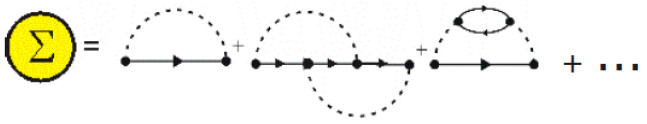

4.5 Hedin's equations

To be able to obtain the one-particle Green's function, the self-energy needs to be known. Lars Hedin first derived a set of equations that can be used to obtain this self-energy [55] and these equations are popularly known as Hedin's equations. To derive this set of equations the derivative technique of Schwinger is used. In this technique a small time dependent external potential $U(\mathbf{r}_1, \mathbf{r}_2, t)$ is introduced, that will be set to zero at the end of the derivation. The one-particle Greens function in the presence of this potential becomes

$$iG(1,2) = \frac{\langle \Psi_0 | T[\hat{S}\hat{\psi}(1)\hat{\psi}^\dagger(2)] | \Psi_0 \rangle}{\langle \Psi_0 | T[\hat{S}] | \Psi_0 \rangle} \tag{4.22}$$

where the creation and annihilation operator (respectively $\hat{\psi}^\dagger$ and $\hat{\psi}$) are as previously defined. Because of the presence of the time-dependent potential, they are now given in the interaction picture, so they still contain the time dependence of the equilibrium Hamiltonian, but the time dependence due to the additional potential is contained in the time evolution operator $\hat{S}$. The definition of this operator is

$$T[\hat{S}] = T\left[exp\Big(-i \int_{-\infty}^{\infty} dt \int \hat{\psi}^\dagger(\mathbf{r}_1, t^+) U(\mathbf{r}_1, \mathbf{r}_2, t) \hat{\psi}(\mathbf{r}_2, t) d\mathbf{r}_1 d\mathbf{r}_2 \Big) \right] \tag{4.23}$$

The complete dependence on U is in this operator only. If $U = 0$, this gives again the previously used equilibrium Green's function (Eq.(4.1)). The first-order variation of $\delta G(1,2)$ with respect to $\delta U(\mathbf{r}_3, \mathbf{r}_4, t_3)$ (variation of a product) is thus given by

$$i\delta G(1,2) = \frac{\langle \Psi_0 | T[\delta\hat{S}\hat{\psi}(1)\hat{\psi^\dagger}(2)] | \Psi_0 \rangle}{\langle \Psi_0 | T[\hat{S}] | \Psi_0 \rangle} - iG(1,2) \frac{\langle \Psi_0 | T[\delta\hat{S}] | \Psi_0 \rangle}{\langle \Psi_0 | T[\hat{S}] | \Psi_0 \rangle} \tag{4.24}$$

and the variation $\delta\hat{S}$ can be evaluated as

$$T[\delta\hat{S}] = -iT\Big[\hat{S} \int_{-\infty}^{\infty} dt \int \hat{\psi}^\dagger(\mathbf{r}_3, t^+) \delta U(\mathbf{r}_3, \mathbf{r}_4, t) \hat{\psi}(\mathbf{r}_4, t) d\mathbf{r}_3 d\mathbf{r}_4 \Big] \tag{4.25}$$

Combining Eq.(4.24) and Eq.(9.2) and inserting the definition of one-particle and two-particle Green's functions gives

$$\begin{aligned} \delta G(1,2) = -\int_{-\infty}^{\infty} dt \int \delta U(\mathbf{r}_3, \mathbf{r}_4, t) [G_2(1, \mathbf{r}_4 t; 2, \mathbf{r}_3 t^+) \\ - G(1,2) G(\mathbf{r}_4 t, \mathbf{r}_3 t^+)] d\mathbf{r}_3 d\mathbf{r}_4 \end{aligned} \tag{4.26}$$

From this equation we can obtain the final result of the Martin-Schwinger functional differentiation technique, which is also valid for $t_3 \neq t^+$

$$\frac{\delta G(1,2)}{\delta U(3,4)} = -G_2(1,4;2,3) + G(1,2)G(4,3) \tag{4.27}$$

This equation gives the connection between the two-particles Green's function and the one-particle Green's function. For a local potential $U(3)\delta(3,4)$ this gives

$$\frac{\delta G(1,2)}{\delta U(3)} = -G_2(1,3;2,3^+) + G(1,2)G(3,3^+) \tag{4.28}$$

which can be used to rewrite the equation of motion Eq.(4.13)

$$\begin{aligned}\Big[i\frac{\partial}{\partial t_1} - \hat{h}_0(\mathbf{r}_1)\Big]G(1,2) + i\int \nu(1,3)G(3,3^+)G(1,2)d3 \\ -i\int \nu(1^+,3)\frac{\delta G(1,2)}{\delta U(3)}d3 = \delta(1,2)\end{aligned} \tag{4.29}$$

Introducing the identity $\int G^{-1}(4,5)G(5,2)d5 = \delta(4,2)$ finally gives

$$\begin{aligned}\Big[i\frac{\partial}{\partial t_1} - \hat{h}_0(\mathbf{r}_1) + i\int \nu(1,3)G(3,3^+)d3\Big]G(1,2) \\ -i\Big[\int \nu(1^+,3)\frac{\delta G(1,4)}{\delta U(3)}G^{-1}(4,5)d345\Big]G(5,2) = \delta(1,2)\end{aligned} \tag{4.30}$$

The third term in this expression is the Hartree potential, as $iG(3,3^+)$ is the electronic density. Comparing this expression with Eq.(4.20), gives an equation for the self-energy

$$\Sigma(1,2) = i\int \nu(1^+,3)\frac{\delta G(1,4)}{\delta U(3)}G^{-1}(4,5)d345 \tag{4.31}$$

or by using the identity

$$\frac{\partial}{\partial U}(G^{-1}G) = G^{-1}\frac{\partial G}{\partial U} + \frac{\partial G^{-1}}{\partial U}G = 0 \tag{4.32}$$

this is

$$\Sigma(1,2) = i\int \nu(1^+,3)G(1,4)\frac{\delta G^{-1}(4,5)}{\delta U(3)}d345 \tag{4.33}$$

To be able to evaluate this expression, a perturbative approach will be used, based on the interacting Green's function G and the dynamical screened Coulomb interaction. Earlier attempts to expand it using the non-interacting

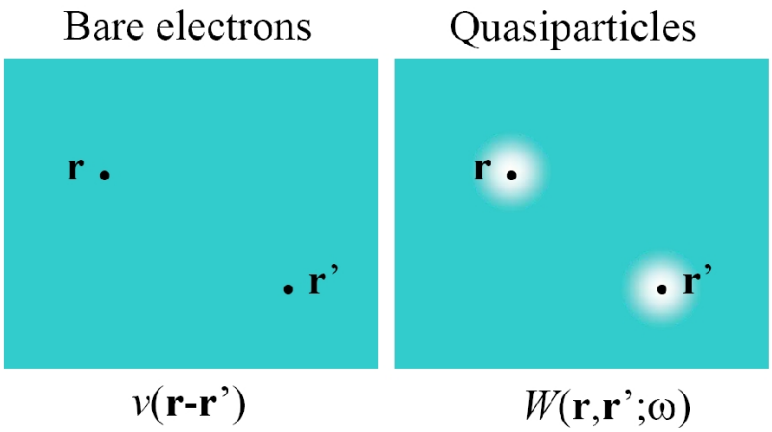

Figure 4.2: Schematic picture that shows the difference between (a) the bare Coulomb interaction ν and (b) the screened interaction W [adopted from Ref. [56]].

Greens function G_0 and the bare Coulomb potential ν have proved unsuccessful because the Coulomb interaction is strong and long ranged, high order terms in the expansion are expected to decay slowly.

On the other hand, each particle in a many-body system does not react to the applied external potential, but to the total potential. This includes the response of the other particles, which significantly reduces the effective potential. Thus, a more realistic answer valid even for low orders should be obtained if we consider the change of the Green's function with respect to the total potential, rather than the external potential. This is the basic idea behind the formulation of the many-body problem proposed by Hedin [55]. Intuitively the screened Coulomb interaction W can be seen as being smaller than the bare one, as interactions between electrons are reduced by the screening of the other electrons. Here we introduce the concept of 'quasiparticle'. The exchange and correlation effects form a Coulomb hole around each electron. This combination of the Coulomb hole and the electron can be seen as a quasiparticle as shown in Fig. 4.2. These quasi-particles interact via the weaker screened interaction W.

This derivation follows Hedin. First a local classical potential V, which is the sum of the perturbation U and the Hartree potential is defined

$$V(1) = U(1) - i \int \nu(1,2) G(2,2^+) d2 \tag{4.34}$$

This will be used to replace all references to U with references to V . Doing this by applying the chain-rule of derivatives in Eq.(4.33) of the self-energy,

gives

$$\Sigma(1,2) = -i \int \nu(1^+,3) \frac{\delta G^{-1}(1,4)}{\delta V(5)} \frac{\delta V(5)}{\delta U(3)} G(4,2) d345 \tag{4.35}$$

This can be rewritten by defining the time-ordered inverse dielectric function ϵ^{-1}

$$\epsilon^{-1}(1,2) = \frac{\delta V(1)}{\delta U(2)} \tag{4.36}$$

the irreducible vertex function $\tilde{\Gamma}$

$$\tilde{\Gamma}(1,2;3) = -\frac{\delta G^{-1}(1,2)}{\delta V(3)} \tag{4.37}$$

and the dynamical screened Coulomb interaction W

$$W(1,2) = \int \nu(1,3)\epsilon^{-1}(3,2) d3 \tag{4.38}$$

Here 'irreducible' means that the differentiation is done with respect to V and not to U. The self-energy then becomes

$$\Sigma(1,2) = i \int G(1,4) W(3,1^+) \tilde{\Gamma}(4,2;3) d34 \tag{4.39}$$

and the diagram for the self-energy with the screened interaction contains a three-point object - $\Gamma(4,2;3)$.

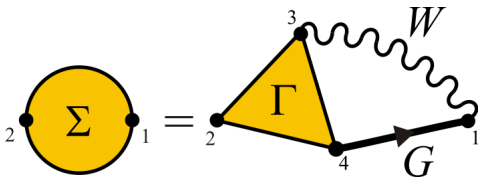

Now the irreducible vertex function $\tilde{\Gamma}$ and the inverse dielectric function ϵ^{-1} will be worked out. For this the Dyson equation $G^{-1} = G_0^{-1} - V - \Sigma$ is used in Eq.(4.37)

$$\begin{aligned}
\tilde{\Gamma}(1,2;3) &= \delta(1,2)\delta(1,3) + \frac{\delta\Sigma(1,2)}{\delta V(3)} \\
&= \delta(1,2)\delta(1,3) + \int \frac{\delta\Sigma(1,2)}{\delta G(4,5)} \frac{\delta G^{-1}(6,7)}{\delta V(3)} d45 \\
&= \delta(1,2)\delta(1,3) + \int \frac{\delta\Sigma(1,2)}{\delta G(4,5)} G(4,6) \frac{\delta G(4,5)}{\delta V(3)} d4567 \\
&= \delta(1,2)\delta(1,3) + \int \frac{\delta\Sigma(1,2)}{\delta G(4,5)} G(4,6) G(7,5) \tilde{\Gamma}(6,7;3) d4567
\end{aligned}$$

In the second line the chain rule was used. The third line is obtained after using the identity in Eq.(4.32) and in the last line the definition of the irreducible vertex function from Eq.(4.37) was used.

For ϵ^{-1}, the definition of V is used

$$\begin{aligned}\epsilon^{-1}(1,2) &= \frac{\delta(U(1) - i\int \nu(1,3)G(3,3^+)d3)}{\delta U(2)} \\ &= \delta(1,2) + \int \nu(1,3)P^{red.}(3,2)d3\end{aligned} \tag{4.40}$$

where

$$P^{red.}(1,2) = -i\frac{\delta G(1,1^+)}{\delta U(2)} \tag{4.41}$$

is the reducible (as the bare potential U is used) polarizability of the system. Similarly the irreducible polarizability P can be defined

$$P(1,2) = -i\frac{\delta G(1,1^+)}{\delta V(2)} \tag{4.42}$$

The connection between these two polarizabilities can be found by applying the chain-rule

$$\begin{aligned}P(1,2) &= -i\int \frac{\delta G(1,1^+)}{\delta V(3)}\frac{\delta V(3)}{\delta U(2)}d3 \\ &= \int P(1,3)\epsilon^{-1}d3 \\ &= P(1,2) + \int P(1,3)\nu(3,4)P^{red.}(4,2)d34\end{aligned} \tag{4.43}$$

Here the definitions Eq.(4.42) and Eq.(4.36) are used. The last line is obtained by inserting the Eq.(4.40).

The last remaining quantity P can be obtained from Eq.(4.42), by applying the identity Eq.(4.32) and inserting the irreducible vertex function Eq.(4.37)

$$\begin{aligned}P(1,2) &= i\int G(1,3)\frac{\delta G^{-1}(3,4)}{\delta V(2)}G(4,1)d34 \\ &= -i\int G(1,3)G(4,1)P(3,4;2)d34\end{aligned} \tag{4.44}$$

The inverse dielectric function, Eq.(4.40), can now be rewritten by inserting Eq.(4.43) repeatedly

$$\epsilon^{-1} = \delta(1,2) + \int \nu(1,3)P^{red.}(3,4)d34 \times \Big[\delta(4,2) + \int \nu(4,5)P^{red.}(5,6)\delta(6,2) + \cdots d56\Big] \tag{4.45}$$

$$= \delta(1,2) + \int \nu(1,3) P^{red.}(3,4) \epsilon^{-1}(4,2) d34 \tag{4.46}$$

which can be used to get rid of the ϵ^{-1} dependency of W

$$\begin{aligned} W(1,2) &= \int \delta(1,3)\nu(3,2)d3 + \int \nu(1,3)P^{red.}(3,4)\epsilon^{-1}(4,3)\nu(3,2)d345 \\ &= \nu(1,2) + \int \nu(1,3)P^{red.}(3,4)W(4,2)d34 \end{aligned} \tag{4.47}$$

This has the Feynman diagram:

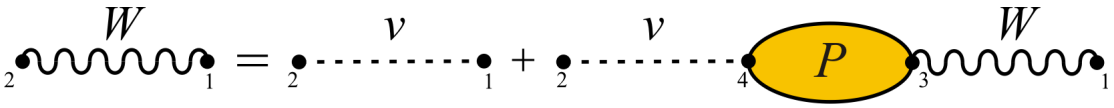

As all quantities are now properly defined, the limit of U going to zero can be safely taken.

In summary the five Hedin equations are given below.

- The Dyson equation:

$$G(1,2) = G_0(1,2) + \int G_0(1,3)\Sigma(3,4)G(4,2)d34$$

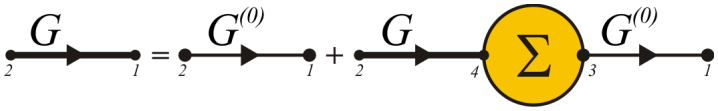

- Self-energy:

$$\Sigma(1,2) = i \int G(1,4)W(3,1^+)\tilde{\Gamma}(4,2;3)d34$$

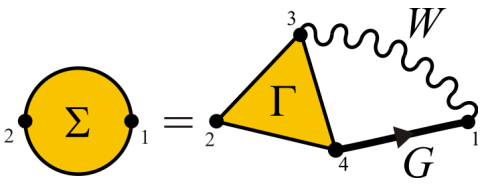

- Screened interaction:

$$W(1,2) = \nu(1,2) + \int \nu(1,3)P(3,4)W(4,2)d34$$

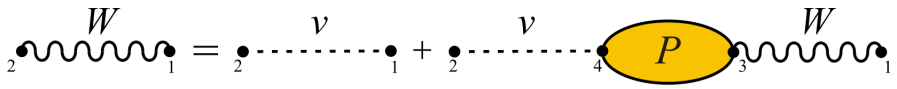

- Irreducible polarization:

$$P(1,2) = -i \int G(2,3)G(4,2)\tilde{\Gamma}(3,4;1)d34$$

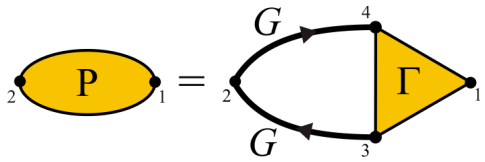

- Vertex function:

$$\tilde{\Gamma}(1,2;3) = \delta(1,2)\delta(1,3) + \int \frac{\delta\Sigma(1,2)}{\delta G(4,5)} G(4,6)G(7,5)\tilde{\Gamma}(6,7;3)d4567$$

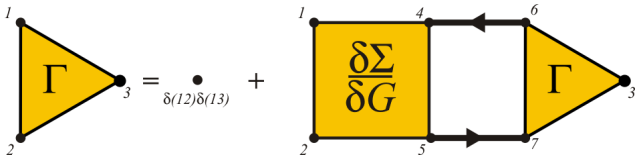

4.5.1 The GW approximation

Hedin's set of equations can be used to, starting from a certain approximation of the self-energy Σ, obtain higher order approximations by iterating through the equations. This is schematically depicted in Fig. 4.3, which is also called the Hedin's 'pentagon' . Unfortunately they are not numerical equations, as they contain a functional derivative. Therefore they can not be solved self-consistently by a computer code, but have to be iterated analytically to obtain an approximation. The simplest approximation is to start with

$$\tilde{\Gamma}(1,2;3) = \delta(1,2)\delta(1,3) \tag{4.48}$$

as the vertex equation, which yields the GW approximation:

- Vertex function:

$$\tilde{\Gamma}(1,2;3) = \delta(1,2)\delta(1,3)$$

- Irreducible polarization:

$$P(1,2) = -i \int G(1,2)G(2,1)$$

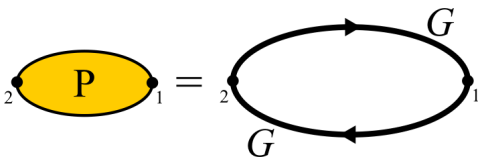

- Screened interaction:

$$W(1,2) = \nu(1,2) + \int \nu(1,3)P(3,4)W(4,2)d34$$

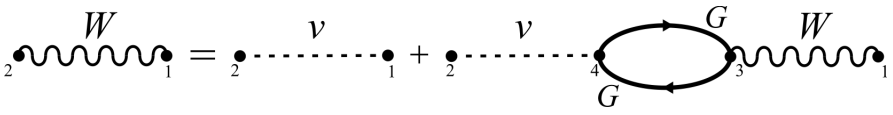

- Self-energy:

$$\Sigma(1,2) = i \int G(1,2)W(2,1^+)$$

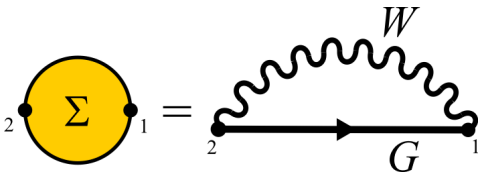

The naming of this approximation refers to the self-energy, which is given by iGW.

The G_0W_0 approximation

Solving the GW equations self-consistently can be very computationally demanding. To make things easier, we can approximate the self energy by replacing the full Green's functions with non-interacting thin-line Green's functions instead. In doing this we can construct four possible different approximations as illustrated in Fig. 4.4. The choice depends on whether we choose $G^{(0)}$ or G. If only one iteration is performed, starting from $\Sigma = 0$, so that $G = G_{KS} = G_0$, one obtains the G_0W_0 approximation or single-shot GW, with main equations described as:

$$P(1,2) = -i \int G(_0 1,2)G_0(2,1) \tag{4.49}$$

$$W_0(1,2) = \nu(1,2) + \int \nu(1,3)P_0(3,4)W_0(4,2)d34 \tag{4.50}$$

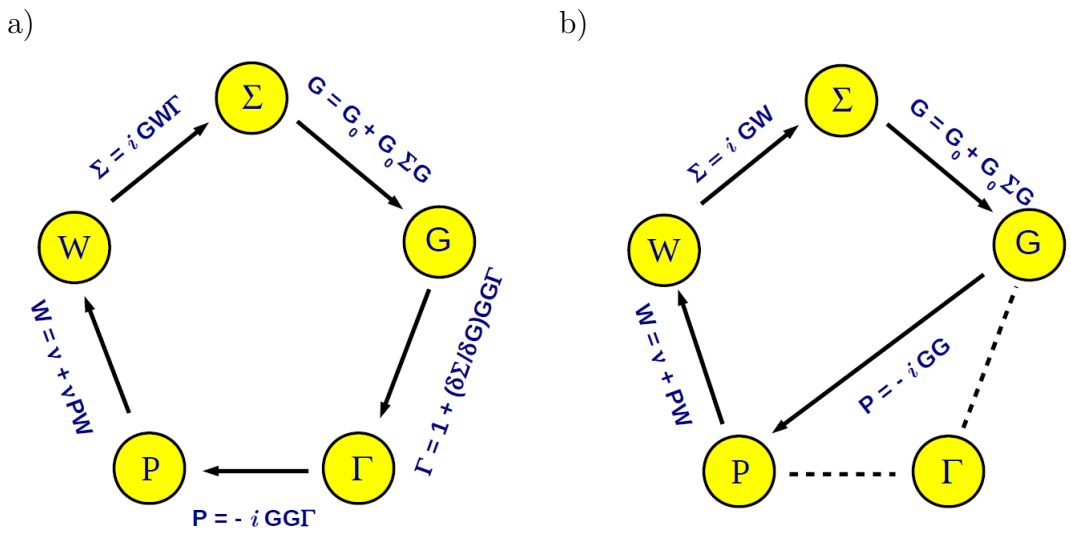

Figure 4.3: Schematic representation a) Hedin's pentagon and b) the GW approximation.

$$\Sigma(1,2) = i \int G_0(1,2) W_0(2,1^+) \tag{4.51}$$

Eq.(4.50) of the irreducible polarizability is equal to the one of independent particles (denoted by P_0). This approximation is only justified if the sum of higher order terms of W is small compared to the first order result. This approximation can be seen as a generalization of the Hartree-Fock approximation, where the bare Coulomb interaction is replaced by the screened one. From the full formula for the polarization, containing the vertex function, it follows that the *GW* approximation is equivalent to the situation where only the contribution of the electron-hole pair excitations to the polarizability are taken into account. All other interactions, such as the interaction between electron and hole and between electron-hole pairs are neglected.

The G_0W_0 approximation works remarkably well for a variety of semiconductors and insulators as observed in Fig. 4.5. Motivated with this fact we start applying it to the TCO materials and the results obtained are presented in the successive chapters.

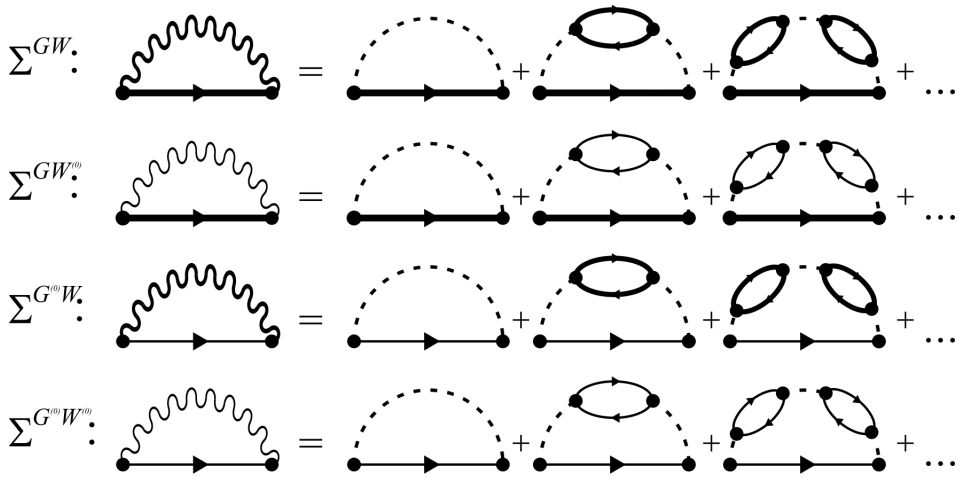

Figure 4.4: Level of self-consistency within the GW approximation

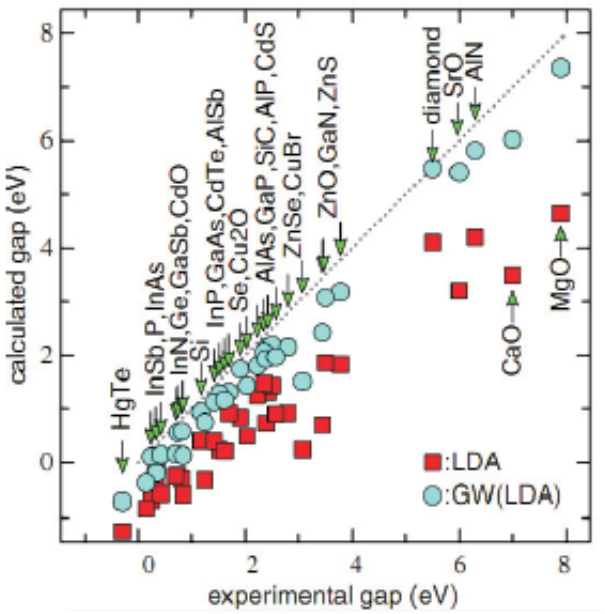

Figure 4.5: Comparison between the experimental gap and the G_0W_0 gap calculated for semiconductors and insulators [from Ref. [57]].

4.6 The GW approximation in practice

The GW self-energy, which is a simple product in time, becomes a convolution in the frequency domain. The evaluation of

$$\Sigma(\mathbf{r},\mathbf{r}',\omega) = \lim_{\eta\to 0}\frac{i}{2\pi}\int d\omega' e^{i\omega'\eta} G(\mathbf{r},\mathbf{r}',\omega+\omega')W(\mathbf{r},\mathbf{r}',\omega') \tag{4.52}$$

is a complicated task. Here the screened interaction is given by

$$W(\mathbf{r},\mathbf{r}',\omega) = \int d\mathbf{r}''\epsilon^{-1}(\mathbf{r},\mathbf{r}'';\omega)\nu(\mathbf{r}''-\mathbf{r}') \tag{4.53}$$

This indicates that the interaction between quasi-particles is much weaker than the "bare" Coulomb interaction between the electrons, due to the repulsion of the electrons in the neighborhood of an electron, i.e. an exchange-correlation hole that is created which screens the interaction. The dielectric function in the frequency domain is

$$\epsilon(\mathbf{r},\mathbf{r}';\omega) = \delta(\mathbf{r}-\mathbf{r}') - \int d\mathbf{r}''\nu(\mathbf{r}''-\mathbf{r}')P(\mathbf{r},\mathbf{r}';\omega), \tag{4.54}$$

where the irreducible polarizability (in the random phase approximation (RPA)) can be shown [23] to be equal to

$$\begin{aligned} P_0(\mathbf{r},\mathbf{r}';\omega) = &\sum_{n\mathbf{k},n'\mathbf{k}'} \phi_{n\mathbf{k}}(\mathbf{r})\phi^*_{n'\mathbf{k}'}(\mathbf{r})\phi^*_{n\mathbf{k}}(\mathbf{r}')\phi_{n'\mathbf{k}'}(\mathbf{r}') \\ &\times\Big[\frac{f_{n\mathbf{k}}(1-f_{n'\mathbf{k}'})}{\epsilon^0_{n\mathbf{k}}-\epsilon^0_{n'\mathbf{k}'}+\omega+i\eta} - \frac{(1-f_{n\mathbf{k}})f_{n'\mathbf{k}'}}{\epsilon^0_{n'\mathbf{k}'}-\epsilon^0_{n\mathbf{k}}+\omega-i\eta}\Big] \end{aligned} \tag{4.55}$$

where $f_{n\mathbf{k}}$ are the Fermi factors.

We begin by solving the quasiparticle equation within a DFT approach, using a standard local approximation to the self-energy

$$\Sigma(\mathbf{r},\mathbf{r}',\omega) = \delta(\mathbf{r}-\mathbf{r}')V_{xc}(\mathbf{r}) \tag{4.56}$$

the quasiparticle equation then becomes a Kohn-Sham equation

$$(\hat{h}+V_{xc})\psi^{KS}_i = \epsilon^{KS}_i\psi^{KS}_i \tag{4.57}$$

where $V_{xc}(\mathbf{r})$ is the local exchange-correlation potential. In many cases the Kohn-Sham eigenvalues ϵ^{KS}_i already provide a reasonable estimate of the band structure and are in qualitative agreement with experiment. For systems where the quasiparticle wave functions are known, one also finds that

the Kohn-Sham wave functions and quasiparticle wave functions are approximately equal [58] (however, it should be noted that there are notable exceptions, such as Cu_2O, where better calculations are necessary and a self-consistent GW (scGW) approach is used [59]). These observations indicates that the self-energy correction is small and justifies the use of first-order perturbation theory to obtain approximate energies

$$\epsilon_i \approx \epsilon_i^{KS} + \langle \psi_i^{KS} | \Sigma(\mathbf{r}, \mathbf{r}', \epsilon_i) - V_{xc} | \psi_i^{KS} \rangle \tag{4.58}$$

This equation indicates that one does not need to calculate the complete Σ matrix, as one element is sufficient to calculate one corrected energy. This is however a nonlinear equation, as Σ depends on the quasi-particle energy. This can be simplified by using a linear expansion of Σ around the Kohn-Sham eigenenergy ϵ_i^{KS}

$$\Sigma(\mathbf{r}, \mathbf{r}', \epsilon_i) \approx \Sigma(\mathbf{r}, \mathbf{r}', \epsilon_i^{KS}) + (\epsilon_i - \epsilon_i^{KS}) \frac{\partial \Sigma(\mathbf{r}, \mathbf{r}', \epsilon_i^{KS})}{\partial \epsilon_i} \Big|_{\epsilon_i^{KS}} \tag{4.59}$$

Using this in the equation above we get

$$\epsilon_i \approx \epsilon_i^{KS} + Z_i \langle \psi_i^{KS} | \Sigma(\mathbf{r}, \mathbf{r}', \epsilon_i) - V_{xc} | \psi_i^{KS} \rangle \tag{4.60}$$

where the quasi-particle renormalization factor (also called the quasi-particle weight) Z_i is given by

$$Z_i = \Big(1 - \langle \psi_i^{KS} | \frac{\partial \Sigma(\mathbf{r}, \mathbf{r}', \epsilon_i^{KS})}{\partial \epsilon_i} \Big|_{\epsilon_i^{KS}} | \psi_i^{KS} \rangle \Big) \tag{4.61}$$

In practice all calculations are carried out in momentum space, so the formulations need to be transformed by applying Fourier transforms. The Fourier transform for the two variable function G^0 is defined as

$$G^0(\mathbf{r}, \mathbf{r}', \omega) \rightarrow G^0_{\mathbf{G}\mathbf{G}'}(\mathbf{q}, \mathbf{q}', \omega) = \frac{1}{\Omega} \int d\mathbf{r} d\mathbf{r}' e^{-i(\mathbf{G}+\mathbf{q}\cdot\mathbf{r})} G^0(\mathbf{r}, \mathbf{r}', \omega) e^{-i(\mathbf{G}'+\mathbf{q}'\cdot\mathbf{r}')} \tag{4.62}$$

where $\mathbf{G}$ denotes a reciprocal lattice vector and $\mathbf{q}$ wave vectors in the irreducible Brillouin zone. Applying this to the real space expression for the polarizability P^0 in Eq.(4.52) gives

$$\begin{aligned} P^0_{\mathbf{G}\mathbf{G}'}(\mathbf{q}, \omega) = \frac{2}{\Omega} \sum_{nn'\mathbf{k}} & \langle n\mathbf{k} | e^{-i(\mathbf{G}+\mathbf{q})\cdot\mathbf{r}} | n'\mathbf{k}+\mathbf{q} \rangle \langle n'\mathbf{k}+\mathbf{q} | e^{-i(\mathbf{G}'+\mathbf{q})\cdot\mathbf{r}'} | n\mathbf{k} \rangle \\ & \times \Big[\frac{f_{n\mathbf{k}}(1 - f_{n'\mathbf{k}'})}{\epsilon^0_{n\mathbf{k}} - \epsilon^0_{n'\mathbf{k}'} + \omega + i\eta} - \frac{(1 - f_{n\mathbf{k}}) f_{n'\mathbf{k}'}}{\epsilon^0_{n'\mathbf{k}'} - \epsilon^0_{n\mathbf{k}} + \omega - i\eta} \Big] \end{aligned} \tag{4.63}$$

Similarly one obtains, using Eq.(4.40) and Eq.(4.38),

$$\epsilon_{\mathbf{GG'}}(\mathbf{q},\omega) = \delta_{\mathbf{GG'}} - \frac{4\pi}{|\mathbf{G}+\mathbf{q}|^2} P^0_{\mathbf{GG'}}(\mathbf{q},\omega) \tag{4.64}$$

$$W_{\mathbf{GG'}}(\mathbf{q},\omega) = \frac{4\pi}{|\mathbf{G}+\mathbf{q}|^2} \epsilon^{-1}_{\mathbf{GG'}}(\mathbf{q},\omega) \tag{4.65}$$

In order to obtain the self energy at a given frequency, the convolution in Eq.(4.52) needs to be calculated. Therefore one needs to calculate ϵ^{-1} for different $\mathbf{q}$-points and for all frequencies. This is computationally very time consuming, especially because the function $P^0(\omega)$ has many poles close to the real axis. In order to avoid this burden, a plasmon-pole model will be used in order to model the inverse dielectric function. The idea behind this approach is that this function is dominated by the peaks at which $\epsilon = 0$, i.e. the plasmon peaks. An additional benefit of using such a plasmon-pole model is that it allows to perform the convolution analytically.

The model used in this thesis is the Godby-Needs plasmon-pole model [60], which models ϵ^{-1} as follows

$$\epsilon^{-1}_{\mathbf{GG'}}(\mathbf{q},\omega) = \delta_{\mathbf{GG'}} + \frac{\Omega^2_{\mathbf{GG'}}(\mathbf{q})}{\omega^2 - (\tilde{\omega}_{\mathbf{GG'}}(\mathbf{q}) - i\eta)^2} \tag{4.66}$$

The two parameters $\Omega^2_{\mathbf{GG'}}$ and $\tilde{\omega}_{\mathbf{GG'}}$ are determined in ABINIT by performing the RPA calculation at two frequencies: at $\omega = 0$ and at $\omega \sim i\omega_p$, where ω_p is the classical plasmon frequency. These frequencies are convenient as these are far away from the poles of P^0, so that the fit is more stable. Alternative choices for determining the fitting parameters exist [61] as well as alternate plasmon-pole models (e.g. Ref. [62]).

If W is split in the bare Coulomb interaction ν and the remainder $W - \nu$ the self-energy can be split in an exchange (Σ^x) and a correlation (Σ^c) part. Symbolically this is

$$\Sigma = iG^{KS}_0 W = iG^{KS}_0 \nu + iG^{KS}_0 (W - \nu) = \Sigma^x + \Sigma^c \tag{4.67}$$

The exchange part of the self-energy reads

$$\Sigma^x(\mathbf{r},\mathbf{r}',\omega) = \frac{i}{2\pi} \int d\omega' G^{KS}_0(\mathbf{r},\mathbf{r}',\omega+\omega')\nu(\mathbf{r},\mathbf{r}')e^{i\omega'\eta} \tag{4.68}$$

which can be evaluated analytically. This leads to the Hartree-Fock exchange term

$$\langle \psi_{n\mathbf{k}} | \Sigma^x | \psi_{n\mathbf{k}} \rangle = -\sum_{m\mathbf{q}}^{occ.} \int d\mathbf{r} d\mathbf{r}' \frac{\psi^*_{n\mathbf{k}}(\mathbf{r})\psi_{m\mathbf{q}}(\mathbf{r})\psi^*_{m\mathbf{q}}(\mathbf{r}')\psi_{n\mathbf{k}}(\mathbf{r}')}{|\mathbf{r}-\mathbf{r}'|} \tag{4.69}$$

Similarly the correlation part of the self-energy is given by

$$\Sigma^c(\mathbf{r},\mathbf{r}',\omega) = \lim_{\eta\to 0}\frac{i}{2\pi}\int d\omega' G_0^{KS}(\mathbf{r},\mathbf{r}',\omega+\omega')[W(\mathbf{r},\mathbf{r}',\omega)-\nu(\mathbf{r},\mathbf{r}')]e^{i\omega'\eta} \quad (4.70)$$

In order to give an expression for the matrix elements of these self-energy parts, it is convenient to define the matrix elements $M^{\nu c}_{\mathbf{G}}(\mathbf{k},\mathbf{q})$ between the occupied valence ($n = v$) and the unoccupied conduction ($n = c$) states

$$\begin{aligned} M^{\nu c}_{\mathbf{G}}(\mathbf{k},\mathbf{q}) &= \int d^3r \psi^*_{\nu\mathbf{k}-\mathbf{q}}(\mathbf{r})e^{-i(\mathbf{q}+\mathbf{G})\cdot\mathbf{r}}\psi_{c\mathbf{k}} \\ &= \sum_{\mathbf{G}'} c^*_{\nu\mathbf{k}-\mathbf{q}}(\mathbf{G}'-\mathbf{G})c_{c\mathbf{k}}(\mathbf{G}') \end{aligned} \quad (4.71)$$

Using this notation the matrix elements of the exchange part can be written in momentum space as

$$\langle\psi_{n\mathbf{k}}|\Sigma^x|\psi_{m\mathbf{k}}\rangle = -\frac{4\pi}{\Omega}\sum_{l}^{occ.}\sum_{\mathbf{q}}\sum_{\mathbf{G}}\frac{M^{ln}_{\mathbf{G}}(\mathbf{k},\mathbf{q})[M^{ln}_{\mathbf{G}}(\mathbf{k},\mathbf{q})]^*}{|\mathbf{G}+\mathbf{q}|^2} \quad (4.72)$$

The correlation part, using the Godby-Needs approximation is given by

$$\begin{aligned} \langle\psi_{n\mathbf{k}}|\Sigma^c|\psi_{m\mathbf{k}}\rangle = -\frac{2\pi}{\Omega}\sum_{l\mathbf{q}}\sum_{\mathbf{G}\mathbf{G}'}\frac{M^{ln}_{\mathbf{G}}(\mathbf{k},\mathbf{q})[M^{ln}_{\mathbf{G}}(\mathbf{k},\mathbf{q})]^*}{|\mathbf{G}+\mathbf{q}||\mathbf{G}'+\mathbf{q}|} \\ \times\frac{\Omega^2_{\mathbf{G}\mathbf{G}'}(\mathbf{q})}{\omega_{\mathbf{G}\mathbf{G}'}(\mathbf{q})(\omega-\epsilon_{l\mathbf{k}-\mathbf{q}}+\mathrm{sgn}(\mu-\epsilon_{l\mathbf{k}-\mathbf{q}})\omega_{\mathbf{G}\mathbf{G}'}(\mathbf{q}))} \end{aligned} \quad (4.73)$$

The sgn function in combination with the electron chemical potential μ is 1 when considering a valence band and -1 for a conduction band. With these self-energy matrix elements calculated, one can calculate the GW corrections to the eigenvalues by using Eq.(4.60).

Chapter 5

ZnO: quasiparticle corrections to the band gap

5.1 Introduction

Having introduced the GW technique to calculate the band gap, we will now start to apply it to the TCO materials. ZnO offers a natural choice to start with[1]. It is an important material in optoelectronic device technology and is used in a number of applications such as visual displays, solar cells and so on. It has also been emerged as an economical alternative to In_2O_3 which is an expensive material due to limited availability of In. Thus *ab initio* first-principles calculations are highly desired to design new devices cost effectively. To reach this goal, it is necessary to have reliable *ab initio* techniques for the prediction of the band gap. Therefore here a thorough study of the quasiparticle energy corrections to the DFT band gap of ZnO is presented. Although the ground state of ZnO has the wurtzite (WZ) structure, the metastable zincblende (ZB) and high pressure rocksalt (RS) phases have growing experimental interest [64, 65]. The zincblende phase of ZnO can be grown using molecular beam epitaxy. The zincblende phase may solve the challenge of controlling p-type conductivity in the optoelectronic devices [64]. Thus, in this chapter we present the quasiparticle corrections to the

[1]This chapter is based on the work published as - **1**] H. Dixit, R. Saniz, D. Lamoen and B. Partoens: "*The quasiparticle band structure of zincblende and rocksalt ZnO*", J. Phys.: Condens. Matter 22, 125505 (2010) **2**] H. Dixit, R. Saniz, D. Lamoen and B. Partoens: "*Accurate pseudopotential description of the GW bands tructure of zincblende and rocksalt ZnO*", Computer Physics Communications 182, 2029 (2011) **3**] M. Stankovski, G. Antonius, D. Waroquiers, A. Miglio, H. Dixit, K. Sankaran, M. Giantomassi, X. Gonze, M. Côté, and G.-M. Rignanese: "*The G0W0 band gap of ZnO: effects of plasmon-pole models*", Phys. Rev. B 84, 241201(R) (2011).

band gap for these three crystal structures of ZnO. We use the pseudopotential plane-wave method to calculate the GW band gap at the Γ point. The DFT-LDA wavefunctions are used to construct the Green's function.

In the case of II^B-VI semiconductor materials, it is important to include the localized 'd' orbitals in the cation pseudopotential (PP). The localized 'd' orbitals play an important role in bonding, hence their inclusion as valence orbital is essential for a correct structure [42]. However the DFT band structure, calculated using the pseudopotential with semicore 'd' states and the plane wave basis, shows serious underestimation of the band gap as discussed earlier in chapter 3. We further observe that the calculated quasiparticle band gap using the GW approximation, is also underestimated for ZnO. This observation is in agreement with the literature and is discussed below in detail. Thus although use of the PP with semicore 'd' states yields the correct structure, it results in a poor quasiparticle correction questioning the validity of such PP. We analyze this problem with a systematic study of the PP used and corresponding GW corrections to the band gap for the ZnO. Further, the different phases of ZnO considered allow us to compare between the crystal symmetry and the effect of *p*-*d* hybridization on the quasiparticle corrections. We also consider ZnS in the zincblende structure that provides an interesting comparison due to change of chemical species from oxygen to sulfur. Thus this chapter is organized as follows. First, we discuss the poor quasiparticle correction with the standard 12-electron Zn PP followed by a systematic study of self-energy dependence on the number of valence electrons used in the PP for two polymorphs - zincblende and rocksalt ZnO. We find that a modified 20-electron PP of Zn, which treats the entire semi-core shell as the valence, is essential for adequate treatment of the self-energy operator. Thereafter we discuss the accuracy of the newly generated 20-electron PP. Finally in section 5.5, we also analyze the effect of the plasmon-pole model used within the GW approximation on the calculated GW band gap of wz-ZnO.

5.2 Computational details

The electronic structure and the quasiparticle correction to the band gap at the Γ point have been calculated using the plane wave pseudopotential code ABINIT [24, 25, 26]. For the electronic structure the plane wave cutoff is chosen using the total energy convergence criterion of 2×10^{-2} eV. The atomic positions and structural parameters have been optimized by calculating the Hellmann-Feynman forces. The stresses are optimized with the criterion of

2×10^{-5} eV/Å^3. We choose 4x4x4 Monkhorst-Pack [38] $k-point$ mesh which yields 10 k-points in the irreducible Brillouin zone.

All PP's used are generated with the OPIUM [40] code according to the Troullier-Martins [67] method with Perdew-Zunger LDA [68]. The electronic configuration of the zinc atom is $[Ne]3s^2 3p^6 3d^{10} 4s^2$. The standard DFT PP treats the 3d and 4s electrons as valence and results in the Zn^{12+} PP. In this work we construct the Zn-PP with 2 ($3s^2 3p^6 3d^{10} 4s^2$), 12 ($3d^{10} 4s^2$), 18 ($3p^6 3d^{10} 4s^2$) and 20 ($3s^2 3p^6 3d^{10} 4s^2$) valence electrons. To generate the 20-electron PP (Zn^{20+} PP), a radius cutoff of 0.42 Å for 3s, 3p and 3d is chosen. It should be noted that we do not construct our 20 electron pseudopotential for the neutral zinc atom, but rather for the Zn ion with the 4s state unoccupied. This radius cutoff shows the smallest transferability error for ionic configurations of Zn (neutral, +1 and +2), at the cost of an increased plane-wave cutoff. We have used 135 Ha as the energy cutoff for plane waves, when Zn^{20+} PP is used. The radial cutoff used in the construction of 2, 12 and 18-electron PP are 1.05 Å 0.42 Å and 0.42 Å for 4s, 3p and 3d states respectively. We use the plane wave cutoff 30, 60 and 95 Ha for 2, 12 and 18-electron PP respectively. The PP becomes harder with the inclusion of localized core orbitals in the valence.

The parameters used within ABINIT to calculate the self-energy, are optimized with convergence criterion of 0.01 eV for the band gap at Γ. We have found that, for both the screening and the self-energy calculation, 300 bands are sufficient to converge the GW band gap. A detailed convergence study of all the GW parameters used in the calculation is presented in Appendix A. The dielectric matrix is calculated with the Godby-Needs (GN) plasmon-pole model (PPM) [23] and is used to calculate the screening. We also calculate the dielectric matrix explicitly with 20 points along the real and 4 points along the imaginary part of the frequency axis, avoiding the use of the plasmon-pole model. We observe that the difference in the GW band gaps obtained with and without plasmon-pole model is less than 0.05 eV. Hence we first report the GW band gaps calculated using the GN plasmon-pole model.

5.3 Result and discussion

The optimized lattice constant, as listed in Table 8.1, shows that the 12 electron PP accurately describes the structural parameter of ZnO and ZnS.

Table 5.1: Optimized lattice constants with the standard Zn^{12+} PP of ZnO and ZnS.

Structure	Lattice constant (Theoretical)Å	Lattice constant (Experiment) Å
ZB-ZnO	4.53	4.47[a]
RS-ZnO	4.25	4.28
ZB-ZnS	5.33	5.42

[a]Experimental lattice constant is smaller than theoretical value due to the strain kinetics and lattice mismatch involved in growing ZB-ZnO films [64].

The calculated DFT band structure and projected density of states (PDOS) for the zincblende and the rocksalt structure are shown in Fig. 5.1. The PP used involves the 3d and 4s states in the valence of zinc. The DFT band structure shows that the upper part of the valence band of ZnO consists of extended $Zn-3d$ and $O-2p$ orbitals. The projected density of states clearly shows significant $p-d$ ($O-2p$ and $Zn-3d$) hybridization in the range of 0 to -6 eV. To get more insight into the $p-d$ hybridization we have listed the projected weights of the Kohn-Sham wave functions at the Γ, K and L point and can be found as appendix B. The $Zn-3d$ derived bands are split into two groups which are triply and doubly degenerate at Γ. The upper (doubly degenerate) band around -4.9 eV shows strong 'd' character while the lower (triply degenerate) band around -6.2 eV is hybridized with $O-p$. The semicore 'd' states of Zn have a relatively high energy in the band structure compared to the experimental value of -8.81 eV, measured for WZ-ZnO [46]. Up to now there is no experimental measurement of the 'd' energy levels for ZB-ZnO and RS-ZnO. However, we believe that the result for WZ-ZnO is also relevant for ZB-ZnO, as both electronic band structures are very similar [66]. ZB-ZnO has a calculated direct bandgap of 0.79 eV while RS-ZnO shows an indirect gap of 1.16 eV and the direct gap at Γ of 2.54 eV.

The nature of the band gap changes from direct to indirect going from the zincblende to the rocksalt phase. This change can be understood on the basis of the symmetry dependence of the interaction between anion 'p' states and cation 'd' states. In the ZB structure, the point group (T_d) does not contain an inversion center, thus the anion 'p' states and cation 'd' states can mix at any point in the Brillouin zone, because there are always 'p' or 'd' states belonging to the same representation [48]. This *p-d* interaction results in a fairly uniform upward shift of the upper valence bands. On the other hand the point group (O_h) of the RS structure contains an inversion center

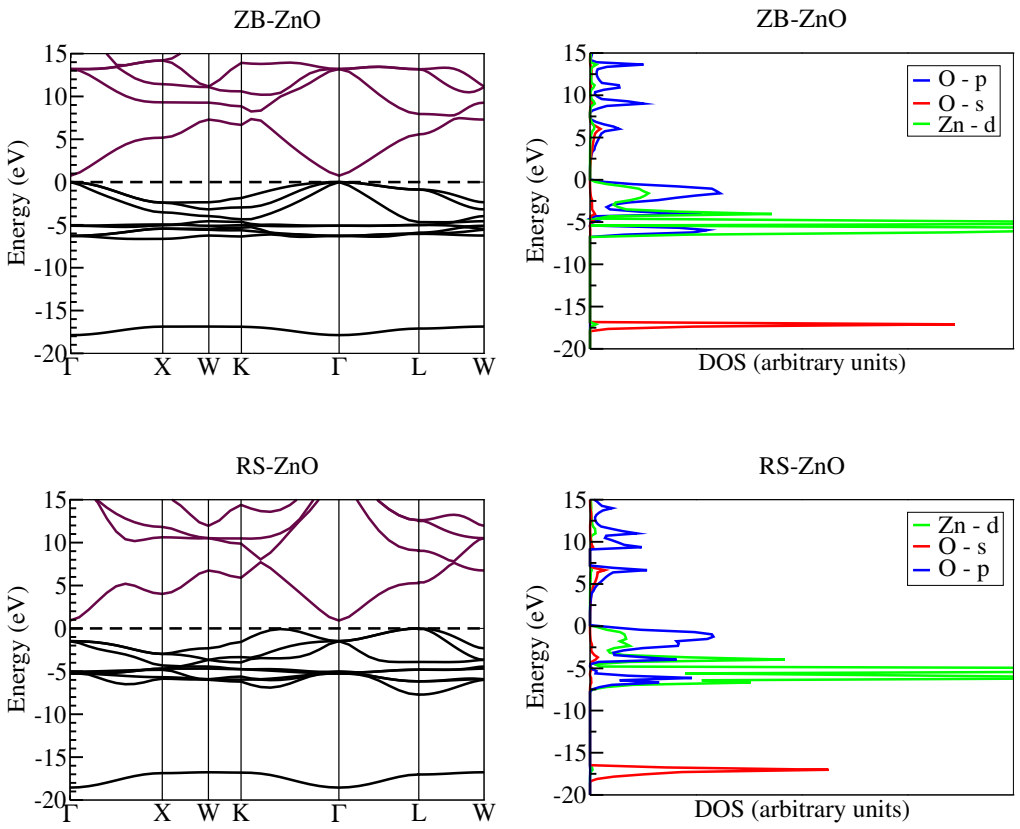

Figure 5.1: Band structure and projected density of states of the ZB and RS ZnO (with 12-electron Zn-PP).

at the Γ point. The 'p' and 'd' states belong to a different representation at the Γ point in the RS structure and do not mix. At other points with lower symmetry, the 'p' and 'd' states can mix in the Brillouin zone. The *p-d* interaction depends on the electron wave-vector and the resulting $p-d$ repulsion leads to an upward dispersion of the top valence bands in the direction $\Gamma - K$ and $\Gamma - L$ of the Brillouin zone. At the Γ point, five valence bands show a strong 'd' character and the top three valence bands have a strong 'p' character (see appendix B). However at the K and L point they mix with each other. The valence band maximum thus occurs away from the Γ point and the RS-ZnO has an indirect band gap.

We calculate the quasiparticle correction at the Γ point for ZB and RS-ZnO with Zn^{12+} PP for zinc. The quasiparticle band gaps and the *Zn-d* energies, obtained with the Zn^{12+} PP, are shown in Table 5.2. Such straightforward

Table 5.2: The DFT-LDA and GW bandgap (E_g) at Γ and $Zn-d$ energy (E_d) level with Zn^{12+} PP (all in eV) calculated at optimized lattice constant.

Structure	E_g^{LDA}	E_g^{LDA+GW}	E_d^{LDA}	E_d^{LDA+GW}	$E_d^{Exp.}$	$E_{gap}^{Exp.}$
ZB-ZnO	0.79	**1.00**	-5.68	-4.57	-8.81	3.27
RS-ZnO	2.54	**3.72**				4.5

application of the GW approximation yields poor results for ZnO. The quasiparticle correction to the band gap for the RS-ZnO is approximately 1.2 eV whereas it results in a 0.2 eV shift for the ZB-ZnO. We also observe that the $Zn-3d$ energy level in the quasiparticle band structure is shifted upwards compared to the DFT result and is away from the experimental value. This problem has been identified in the case of CdS by Rohlfing *et al.*[69]. The unreasonable shift of the d-energy levels is due to an inadequate treatment of the nonlinear exchange-correlation interaction in the self-energy. They have shown that when cation core states are successively included in the valence electron shell, the GW correction improves. The GW band gap is in excellent agreement with experiments for CdS, when Cd 4s, 4p, 4d and 5s states are used as valence in the PP. In case of ZnS a similar analysis holds and the GW band gap obtained is 3.5 eV in close agreement to the experimental value of 3.8 eV [70]. We apply a similar study to ZB and RS-ZnO along with ZnS which has a ZB structure. The change in the chemical environment, achieved by replacing oxygen with sulfur, leads to a weaker $p-d$ hybridization between anion and cation, which is discussed later.

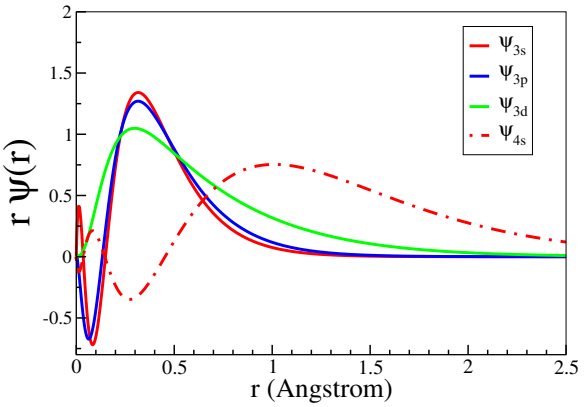

Figure 5.2: All electron wavefunction plot for the Zn atom.

The all-electron wavefunction plot for atomic Zn shows (Fig. 5.2) large spatial overlap of the 3s, 3p and 3d wave functions. Thus separating 3d orbitals from the core and therefore making an artificial division of 3d, 4s as valence is considered to be the cause of the poor quasiparticle correction [69, 71]. The nonlinear exchange-correlation interaction, which depends on the spatial overlap of atomic orbitals, is not properly described in the self-energy when the Zn^{12+} PP is used. To analyze this fact we consider three different ionic Zn pseudopotentials with the 2, 18 and 20 valence electrons respectively. The quasiparticle correction for the band gap and the $Zn-d$ energy are listed in Table 8.5. The inclusion of 3p and 3s states in the valence description of the Zn atom results in the lowering of the $Zn-d$ energy and an improved quasiparticle correction for the band gap. The GW band gaps presented in this table are calculated at the experimental lattice constant of the ZB-ZnO to focus on the effect of the PP's change, but the DFT lattice constants are listed in the last column. It should be noted that the experimental lattice constant used is less than the optimized lattice constant (due to film growth conditions), thus the corresponding DFT and GW band gaps are higher. The 2-electron PP of Zn ($4s^2$), shows that the GW bandgap overestimates the experimental value. Also the optimized lattice constant 3.27 Å, with this PP, is too small compared to the experimental value of 4.47 Å. Since the Zn-d atomic energy lies in between the O-s and O-p atomic energy levels, the Zn-d electrons play an important role in the bonding. Thus treating the 'd'-electrons as core, thereby removing the $p-d$ hybridization, leads to a GW gap too wide compared to experiment. The system is not screened enough in absence of the 'd'-electrons. For the 12 electron PP of Zn ($3d^{10}$, $4s^2$), the GW correction yields practically no shift. This is due to the fact that with the Zn^{12+} PP, the exchange energy contribution due to spatial overlap of '3d' with the '3p' and '3s' orbitals is neglected in the self-energy. This is supported by Zn^{18+} PP, where the GW gap is opened further and the $Zn-3d$ energy level is now realigned with DFT-LDA energy. It should be noted that the DFT lattice constant obtained with the Zn^{18+} PP is larger than the experimental value. There is no physical reason to separate the '3p' orbital from '3s' and in the construction of PP and we have added Zn^{18+} PP result for completeness. Finally we construct 20-electron PP to describe the exchange interaction properly in the self-energy calculation. With the 20-electron PP, the $Zn-3d$ energy level is positioned around -6.53 eV, about 1 eV lower than the DFT-LDA result and is now closer to the experimental value. The calculated GW band gap is 2.53 eV, which is still lower by $\sim$0.8 eV than the experimental value (3.27 eV). However, this compares well with the all-electron result, 2.44 eV, for the WZ-ZnO [72]. Also the DFT optimized lattice constant with the 20-electron PP is in agreement with the experiment.

Table 5.3: The DFT-LDA and GW bandgap and $Zn-d$ energy (all in eV) at Γ, with four different pseudopotentials for ZB-ZnO (at experimental lattice constant(4.47 Å)).

Zn PP	E_g^{LDA}	E_g^{LDA+GW}	E_d^{LDA}	E_d^{LDA+GW}	Optimized lattice con.
Zn^{2+}	3.10	5.26	–	–	3.27 Å
Zn^{12+}	0.83	1.09	-5.96	-4.90	4.53 Å
Zn^{18+}	0.66	1.57	-6.36	-6.83	4.71 Å
Zn^{20+}	0.88	2.53	-5.67	-6.53	4.50 Å

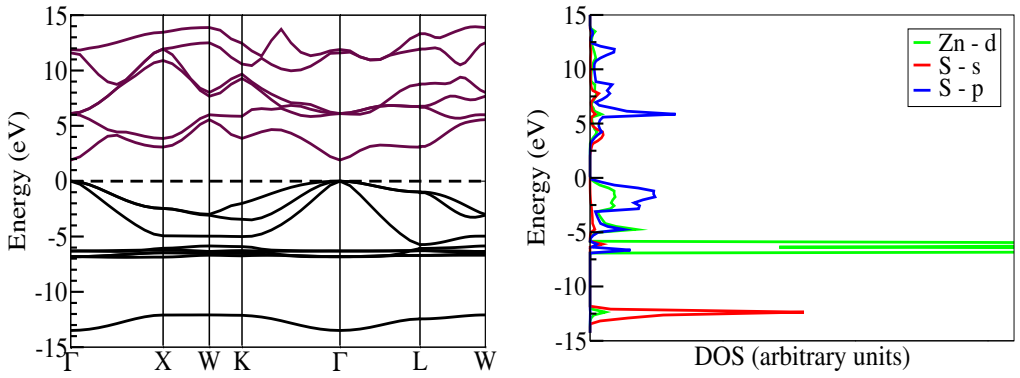

Figure 5.3: Band structure and projected density of states of ZnS (with 12-electron Zn-PP).

Table 5.4: Atomic orbital eigenvalues (in eV) for zinc, oxygen, and sulfur along with the energy difference between the anion-p (ϵ_p^a) and cation-d (ϵ_d^c) levels.

Zn 4s	-6.06	O 2s	-23.69	S 3s	-15.26
Zn 3d	-10.84	O 2p	-9.20	S 3p	-7.12
ϵ_p^a - ϵ_d^c			**1.64**		**3.72**

The underestimation of the GW bandgap in ZB-ZnO, when the Zn^{20+} PP is used, can be attributed to the strong $p-d$ hybridization between the anion and cation. To show this, we make a similar study for the RS-ZnO and ZnS.

These two prototype systems are of interest because for RS-ZnO, the $O-p$ and the $Zn-d$ states do not mix at the Γ point. The five valence bands have strong $Zn-d$ character and the top three conduction bands have strong $O-p$ character and illustrate the absence of $p-d$ mixing at the Γ. The change of chemical species from oxygen to sulfur shows a weaker $p-d$ hybridization in the electronic structure of ZnS as can be seen from the band structure and PDOS in Fig. 5.3. The PDOS shows that the strongly dispersed valence bands in the energy range of 0 to -5 eV have a dominant $S-p$ character and the $Zn-d$ energy is located around -6.5 eV. The atomic orbital energies for zinc, oxygen and sulfur, calculated within LDA using the OPIUM code, are listed in Table-5.4. The $p-d$ energy difference for ZnO is 1.64 eV compared to 3.72 eV for ZnS. Hence the electronic structure of ZnS shows a weaker hybridization compared to that of ZB-ZnO.

Table 5.5: The DFT-LDA and GW bandgap and $Zn-d$ energy (all in eV) at Γ, for RS-ZnO and ZnS with four pseudopotentials (at experimental lattice constant).

Zn PP	E_g^{LDA}	E_g^{LDA+GW}	E_d^{LDA}	E_d^{LDA+GW}	Optimized lattice con.
			RS-ZnO		Experiment = 4.28 Å
Zn^{2+}	2.66	4.26	–	–	2.85 Å
Zn^{12+}	2.38	3.52	-4.07	-1.74	4.25 Å
Zn^{18+}	2.05	2.94	-4.71	-5.40	4.39 Å
Zn^{20+}	2.39	3.77	-3.78	-5.21	4.21 Å
			ZnS		Experiment = 5.42 Å
Zn^{2+}	2.60	4.01	–	–	4.68 Å
Zn^{12+}	1.87	2.64	-6.63	-4.30	5.33 Å
Zn^{18+}	1.70	2.71	-7.27	-7.47	5.60 Å
Zn^{20+}	1.77	3.38	-6.56	-7.16	5.32 Å

We now calculate the quasiparticle correction with the same set of PP for RS-ZnO and ZnS. Table 5.5 lists the quasiparticle corrections and position of $Zn-3d$ states. All the calculations are again done at the fixed value of the experimental lattice constant for a meaningful comparison of the bandgap and $Zn-3d$ level. We observe a similar trend for RS-ZnO and ZnS. The Zn^{2+} PP overestimates the GW band gap. The Zn^{12+} PP gives an insufficient quasiparticle correction due to inadequate treatment of the exchange interaction in the self-energy. With the inclusion of 3p and 3s orbitals, the

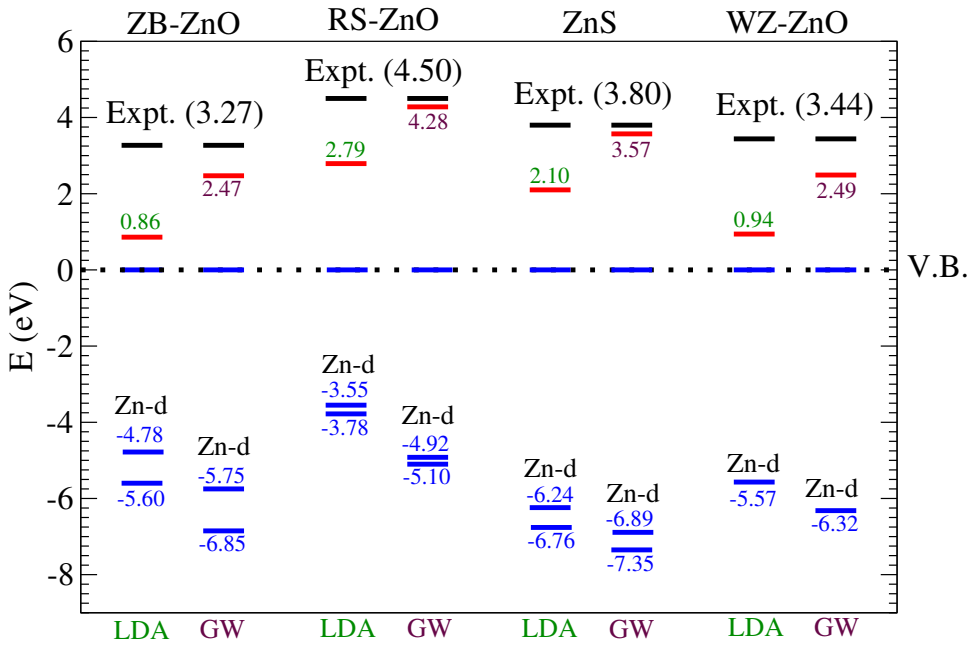

Figure 5.4: Schematic band structure showing the DFT-LDA and GW band gap along with position of Zn-d energies at the Γ point, calculated at optimized lattice constant using 20-electron Zn-PP.

exchange interaction is now properly treated which leads to lowering of the 'd'-energy level compared to DFT-LDA result and opening of the GW band gap. This confirms the dependence of the self-energy on the spatial overlap of the atomic orbitals. Thus Zn^{20+} pseudopotential yields the best GW result.

Finally we calculate the GW band gap at the optimized lattice constant with the Zn^{20+} PP. The optimized lattice constants are 4.50, 4.21 and 5.32 Å for ZB-ZnO, RS-ZnO and ZnS respectively. These lattice constants are within an error of ∼1.5% compared to the experimental value. Schematic overview of the quasiparticle band structure is shown in Fig. 5.4. The $Zn-d$ energy level in the GW band structure is lower than DFT-LDA counterpart for all the systems. The GW band gap, at the Γ point, for ZB-ZnO is 2.47 eV compared to 3.27 eV from experiment. This bandgap can be compared and is in agreement with the non-self-consistent GW bandgap of 2.46 eV [73] and the all-electron result of 2.44 eV [72] for WZ-ZnO, as both structures are similar. For completeness, we have also obtained the GW gap of 2.49 eV for WZ-ZnO with this Zn^{20+} PP. The optimized lattice parameters for WZ-ZnO are *a=b=3.192 Å , c=5.162 Å* and *u=0.380*, which compares well

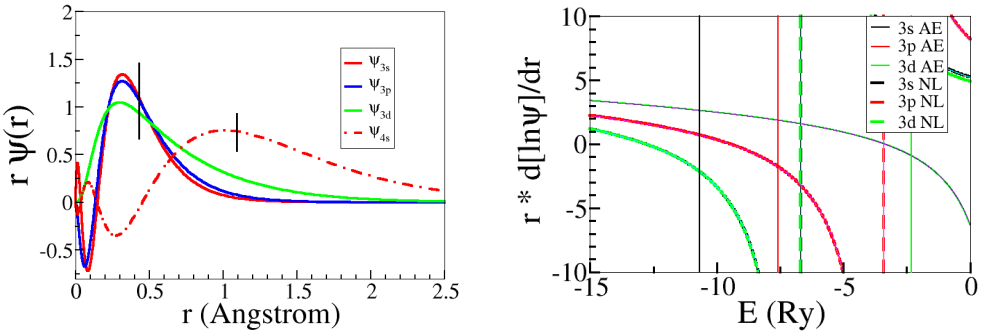

(a) (b)

Figure 5.5: (a) All electron wavefunction and (b) logarithmic derivative plot.

with the experimental values *a=b=3.258 Å , c=5.220 Å* and *u=0.382* [74]. For RS-ZnO we obtain a GW band gap of 4.27 eV, at the Γ point, compared to the experimental value of 4.5 eV. The GW band gap, at Γ, of ZnS is 3.57 eV which is in agreement with 3.54 eV published in the literature [75], and also compares with the experimental value of 3.8 eV. These results clearly show that the non-self-consistent GW correction depends on the extent of hybridization.

5.4 Details of 20-electron PP

The norm-conserving 20-electron PP is highly accurate as is evident from its ability to provide an accurate description of the structural properties and the quasiparticle correction mentioned above. Here we present further details of this PP. As stated earlier, it is generated with the OPIUM code according to the Troullier-Martins method with Perdew-Zunger LDA. A radius cutoff of 0.42 Å for 3s, 3p, 3d and 1.08 Å for 4s orbital is chosen.

An efficient PP should be transferable among a variety of chemical environments. A way to qualitative check the transferability of the PP is to plot the logarithmic derivatives of the all-electron and pseudo wave-function. The condition for good transferability is to have the all-electron and pseudo logarithmic derivatives agree closely for a region of about 1-2 Ry around the eigenvalues. We can see that this is true for Zn^{20+} PP (see Fig. 5.5(b)). The cutoff radius (r_c) plays an important role in the computation. We have chosen

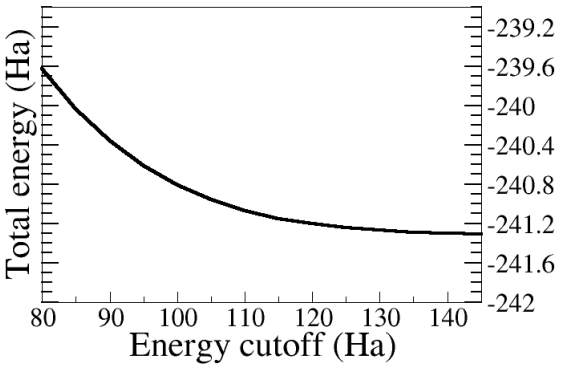

Figure 5.6: Total energy versus plane-wave cutoff.

the r_c value to achieve a convergence error of between 10-100 meV/electron between the pseudo and all-electron eigenvalues and tested it w.r.to accurate description of the structural parameters. This strict convergence criterion, however, results in a hard PP and the plane-wave cutoff increases correspondingly. The total energy for this PP converges rather slowly and we have used the plane-wave cutoff of 135 Ha ($\sim$4 times larger compared to the standard Zn^{12+} PP). The convergence of the total energy as a function of the plane-wave cutoff is shown in Fig. 5.6

5.5 Effect of plasmon-pole model

Shortly after we published our results, Shih *et al.* [76] claimed that a reasonable theoretical gap ($\sim$ 3.6 eV) for WZ-ZnO could be obtained by using conventional perturbative G_0W_0 approach and including a Hubbard U parameter to account for the strongly correlated Coulomb repulsion between the Zn semicore d states and the valence shell p states. This result seems promising and the authors have suggested a reexamination of previously reported LDA+G_0W_0 results where the band gap of WZ-ZnO is underestimated. We have obtained LDA+G_0W_0 band gap of 2.49 eV which is underestimated compared to the experimental band gap of 3.44 eV. Thus the implication of Ref. [76] is that our calculations might have been under-converged. In their work, Shih *et al.* used Hybertsen-Louie (HL) plasmon-pole model (PPM), whereas we use the GN PPM to account for the frequency dependence of

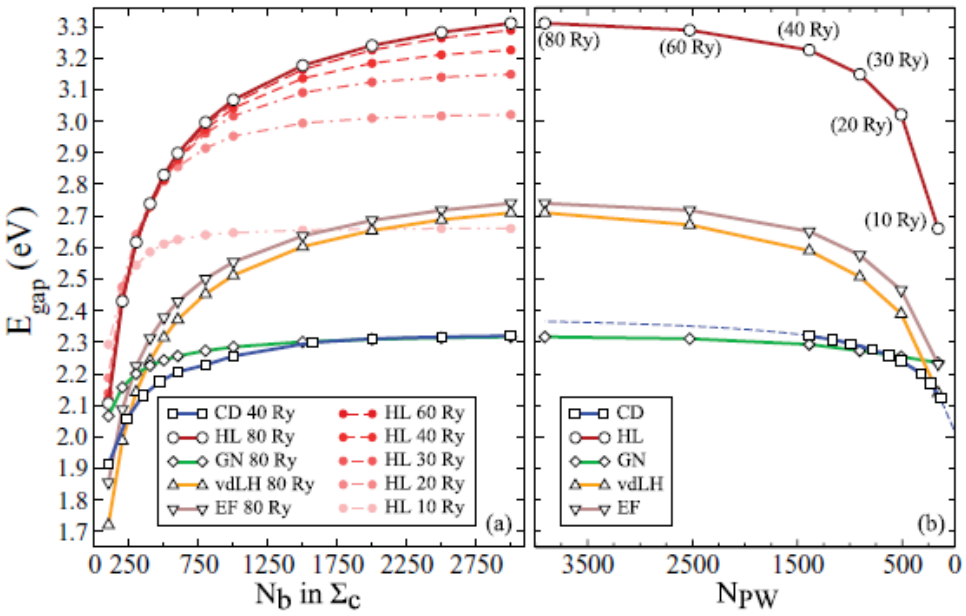

Figure 5.7: (a) Convergence of the LDA + G_0W_0 band gap vs the number of bands included in the sum over unoccupied bands in the self-energy, and (b) convergence of the band gap vs the energy cutoff of the dielectric matrix (parameter *ecutwfn*, see appendix A). Contour deformation (CD) is the actual result, i.e., using a full-frequency treatment without a plasmon-pole model (PPM). The Hybertsen-Louie (HL), Godby-Needs (GN), von der Linden-Horsch (vdLH), and Engel-Farid (EF) PPMs seek to emulate the CD result. The CD curve in (a) is taken at 40 Ry, whereas the result at 80 Ry is expected to be where the extrapolated CD curve (squares) in (b) levels out [*Taken from Ref. [79]*].

the inverse dielectric function of the material. However, results can vary greatly depending on the exact PPM used [77, 78]. Thus to confirm that our results calculated using GN PPM are not under-converged and analyze the effect of different PPM used, here I will describe a detailed study of PPM and G_0W_0 band gap. These results are obtained by M. Stankovski *et al.* [79] and co-workers at Université Catholique de Louvain. I collaborated in this work and provided the same 20 electron PP as described above. We study in great detail, and to a high numerical accuracy, exactly what effect different plasmon-pole models have on the value of the band gap. In order to compare our results closely with those of Ref. [76], we use the same numerical parameters, and we also perform full-frequency calculations (i.e. without any PPM).

The quasiparticle corrections to the band gap are calculated using the DFT-LDA band structure as the starting point. For an easy comparison we first reproduce the convergence behavior of the G_0W_0 band gap reported by Shih *et al.* [see Fig. 5.7] using HL PPM. Next, we recalculate the G_0W_0 band gap using GN PPM and also other two PPM available namely the von der Linden-Horsch (vdLH) PPM and the Engel-Farid (EF) PPM. With these two PPMs used, the G_0W_0 band gap obtained (2.71 and 2.73 eV respectively) is significantly lower compared to the result with HL PPM (3.3 eV). From Fig. 5.7, we observe that the convergence behavior of the vdLH and EF PPM are similar to that of the HL PPM, i.e., the G_0W_0 band gap converges very slowly with respect to the number of bands and the plane-wave cutoff used in the computation. For the GN PPM this behavior is milder, and only $\sim$800 unoccupied bands is sufficient to converge the value of the gap to within 0.02 eV. The converged value for the GN PPM is 2.35 eV. This study confirms the fact that the G_0W_0 band gap of WZ-ZnO depends on the PPM used in the computation. At last, I will mention an interesting result obtained using the model-free contour deformation (CD) technique, which is computationally expensive. The G_0W_0 band gap using the CD technique is 2.4 eV with a slightly slower convergence rate than the GN PPM ($\sim$1700 unoccupied bands are sufficient to converge). Clearly, the PPM which best reproduces the CD result is the GN PPM and moreover it requires smaller number of unoccupied bands to achieve the converged result.

5.6 Summary

The systematic study of the PP and corresponding GW correction show that Zn^{20+} PP is essential to describe the localized d-levels correctly in ZnO. The GW band gap obtained with Zn^{20+} PP is in agreement with the all electron single-shot GW result [72, 73]. The ZB and RS phase of ZnO provide an interesting comparison between crystal symmetry and hybridization. The underestimation of the GW band gap in ZB-ZnO is correlated with the $p-d$ over-hybridization within the LDA. The RS phase includes the inversion symmetry at the Γ point in the Brillouin zone. The 'p' and 'd' states do not mix at the Γ point and therefore the GW correction at the Γ point is better for the RS-ZnO compared to the ZB counterpart. Also the weakly hybridized system ZnS is well described with the Zn^{20+} PP and the GW approximation. The detailed study of the dependence of the GW band gap on the plasmon-pole model used, performed by our collaborators at the Université Catholique de Louvain, further validates the underestimation of the band gap within the G_0W_0 approach. In conclusion, ZnO is still an example of a system where one has to be careful about the choice of PPM, and where the LDA + G_0W_0 approach fails in contrast to other semiconductors which show a good agreement between the G_0W_0 and the experimental gap (refer Fig. 4.5).

Chapter 6

Quasiparticle band structure of SnO_2 and CdO

6.1 Introduction

Next, we have studied two other systems namely SnO_2 and CdO using the GW approximation[1]. As stated earlier in Chapter 3, CdO has rocksalt structure and the nature of the band gap is indirect while SnO_2 crystallizes in the rutile structure with reported optical band gap of 3.6 eV. Here I will present the quasiparticle band structure calculated for these two materials. We have learned in the previous chapter that for adequate treatment of the self-energy operator a special care is essential with the plane-wave pseudopotential approach. A large spatial overlap of the semi-core atomic orbitals is also observed in the case of both the Cd and Sn atom. Thus we construct Sn^{22+} and Cd^{20+} PP in a similar way we constructed the Zn^{20+} PP for adequate treatment of the self-energy in the GW approximation. These PP are tested for their accuracy and they correctly describe the structural properties. For SnO_2, an early calculation using the GW approximation found a band gap of $\sim$ 3.4 eV [80]. However, this calculation did not take into account the effect of Sn core electron levels now known to be relevant. This results in uncertainty regarding the values in Ref. [80]. In SnO_2, furthermore, the c/a ratio is very important [82, 83], and it is of interest to study the effects of uniaxial pressure on its electronic structure. Note that such a pressure indirectly causes biaxial strain perpendicular to its axis of application. This is of further interest because in optoelectronic applications with TCO thin

[1]Part of this chapter is based on the work published as - R. Saniz, H. Dixit, D. Lamoen and B. Partoens: "*Quasiparticle energies and uniaxial pressure effects on the properties of SnO_2* ", Applied Physics Letters 97, 261901 (2010).

films, the substrate often subjects the film to biaxial strain with great effect on the electronic properties of the film. Therefore, we use a state-of-the-art implementation of the GW approximation to determine the quasiparticle energy spectrum of SnO_2 in its ground state and study the effects of applied uniaxial pressure along the c-axis. The calculations for SnO_2 are performed by Dr. Rolando Saniz and I collaborated in this work during the generation and testing of Sn^{22+} PP and partly in the band structure calculations.

For CdO, it is important to calculate the full quasiparticle band structure since it has an indirect band gap. However, a complete band structure calculation for large number of k-points is computationally demanding and time consuming due to use of the modified PP that requires a high plane-wave cutoff (E_{cut}). Thus we have made use of the Wannier functions (the detailed description follows in a later section) to interpolate the quasiparticle band structure from the initial calculation performed over a coarse k-point mesh.

6.2 Computational details

Our study starts with a DFT calculation within the LDA to the exchange-correlation potential using the ABINIT code. For this, we first generate a 22 electron ($4s^2$ $4p^6$ $4d^{10}$ $5s^2$ $5p^2$ valence states) norm-conserving PP for Sn and 20 electron ($4s^2$ $4p^6$ $4d^{10}$ $5s^2$ valence states) norm-conserving PP for Cd. We use the OPIUM code for construction of the PPs choosing the TroullierMartins procedure and the Perdew-Zunger LDA. We use core radii of 1 bohr for the n=4 shell and 2.28 bohr for the n=5 shell. The pseudopotential thus produced is hard, requiring a cutoff energy of 125 Ha for eigenvalues to be converged within a meV. To assess the reliability of our pseudopotential, we study the structural properties and the structural parameters are listed in Table 6.1. SnO_2 has a rutile structure in its ground state (space group P42/mnm, No. 136) with two formula units per unit cell and an internal parameter, u, fixing the positions of the O ions. CdO has rocksalt structure (space group $P6_3mc$, No. 186) with experimental lattice constant of 4.69 Å. As seen from this table, the calculated structural parameters are in excellent agreement with experiment.

6.3 Results and discussion

First, we will discuss the quasiparticle band structure together with the effects of applied uniaxial pressure along the c-axis on the GW band gap for

Table 6.1: Optimized and experimental values of structural parameters.

	Theory	Expt.
SnO_2	a = 4.73 Å	4.71 Å
	c = 3.18 Å	3.18 Å
	u = 0.305	0.306
CdO	a=b=c= 4.65 Å	4.69 Å

SnO_2. Thereafter, in the later section, we will discuss the Wannier interpolated quasiparticle band structure of CdO.

6.3.1 SnO_2

The DFT electronic structure we obtain (referred to below as LDA) is used to calculate the quasiparticle energies within the (single-shot) GW approximation. In Fig. 6.1 (a), we compare the LDA band structure and the GW quasiparticle energies along high symmetry lines in the first Brillouin zone.

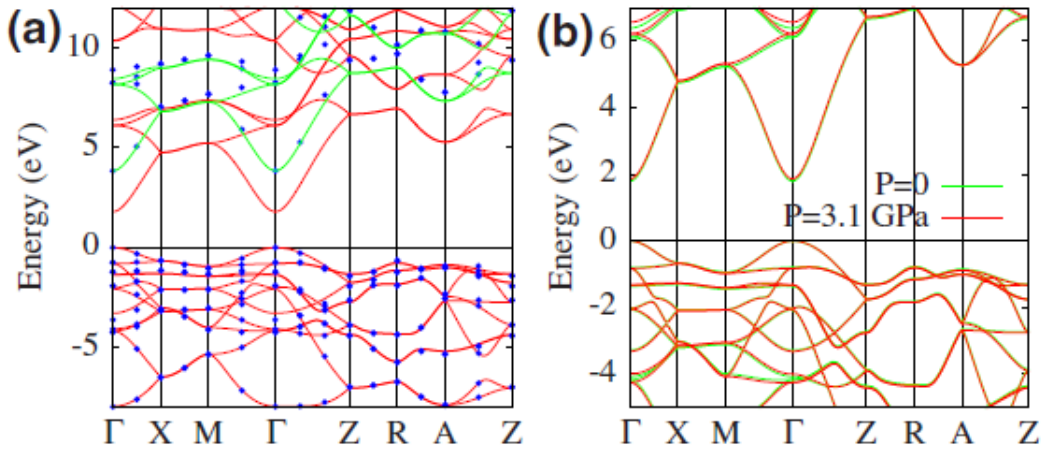

Figure 6.1: (a) Electronic structure of SnO_2. The red lines indicate the LDA band structure. The blue dots are the GW quasiparticle energies. The green lines represent the upward shifted LDA conduction bands so as to match the lowest conduction band level with the GW result. (b) Effect of uniaxial pressure along the *c*-axis on the LDA electronic structure of SnO_2.

Table 6.2: Quasiparticle energy corrections (ΔE = $E_g^{GW} - E_g^{LDA}$) at high symmetry points (values are in eV).

k point	Γ	X	M	Z
LDA	1.80	5.42	6.17	7.99
GW	3.85	7.69	8.72	10.81
ΔE	2.05	2.27	2.55	2.82
GW (P=3.1 GPa)	3.94	7.78	8.87	10.89
ΔE (P=3.1 GPa)	2.08	2.30	2.57	2.84

The dark red line gives our LDA values. The band gap is direct and at the Γ point, with a value of 1.80 eV. This is close to results in previous work, such as Ref. [80] (1.71 eV) and [81] (1.70 eV). In the former, a pseudopotential including nonlinear core corrections is used to describe the Sn 4d electrons, while the latter uses an all-electron method. Note that these values are significantly different from the result obtained with DFT-projector augmented-wave (PAW) approaches, where values of 0.69 and 0.65 eV are reported (see Refs. [84] and [85]). The origin of the discrepancy is not understood, particularly because PAW results should in principle be close to all-electron results. The blue dots in Fig. 6.1(a) give the GW values calculated using the GN PPM. For a quantitative comparison, in Table 6.2 we give the LDA and GW direct gaps at high symmetry points in the first Brillouin zone. Note that our gaps at Γ and Z are higher than the GW results in Ref. [80] (3.38 and 10.32 eV, respectively) by almost 0.5 eV. The difference is considerable. This arises because although the 4d electrons are included in the pseudopotential in Ref. [80], the 4s and 4p are not. The contribution of the latter, mainly to the exchange interaction, is thus absent and leads to the expected underestimation of the gap values [69, 86] Our result suggests, most interestingly, that the optical gap of 3.6 eV of Ref. [87] results from excitonic effects, which cause a redshift of the optical absorption energies compared to what would be observed if electron-hole interactions were negligible. Note that a very recent work, proposing a novel approximation scheme to excited levels within single-shot GW, uses the more expensive self-consistent Coulomb hole plus screened exchange (COHSEX) band structure as a starting point to find E_g=3.8 eV [88]. This is very close to our result and further supports the idea of an optical gap smaller than E_g. Table 6.2 further shows that the GW gap corrections at the X, M, and Z points are increasingly larger away from Γ. For a broader comparison, the green curves in Fig. 6.1 (a) show that the LDA conduction bands rigidly shift upward, aligning the LDA and GW conduc-

tion band minima. This shows that a scissors operator approach is not ideal with discrepancies increasing as one moves away from Γ and as one moves up from the lowest conduction band. The above notwithstanding, Fig. 6.1 (a) also shows that very close to Γ, the energy dispersion of the highest valence band and the lowest conduction band deviates little from the GW results. This suggests that the electron and hole effective masses (m_e^* and m_h^*, respectively) may be well approximated by the LDA values. We calculate m_e^* (m_h^*) by fitting the lowest conduction (highest valence) band dispersion around Γ with an even polynomial of order 6. As seen in Table 6.3, the theoretical results are close to experiment, but somewhat lower. The difference can be

Table 6.3: Quasiparticle effective masses at Γ (in units of the electron mass, m_e). Experimental data from Ref. [89].

	$m^*_{e\perp}$	$m^*_{e\parallel}$	$m^*_{h\perp}$	$m^*_{h\parallel}$	m_p
Expt.	0.299	0.234			0.275
Theory	0.253	0.223	1.228	1.655	0.271
Theory (P=3.1 GPa)	0.260	0.227	1.215	1.701	

understood as follows. Button and co-workers [89] pointed out that SnO_2 is a polar material and that, therefore, the effective masses they reported are, in fact, polaron effective masses (m_p^*). In intermediate coupling theory, m_p^* and m_e^* obey to $m_p^* = m_e^*(1 + \alpha/6)$, where α is the electron-phonon coupling parameter [90]. Taking $m_e^* = (m_{e\perp}^{*2} m_{e\parallel}^*)^{(1/3)}$ (the density of states m_e^*) and α =0.7, as estimated in Ref. [90] for SnO2, we find that m_e^*=0.271m_e in very good agreement with Ref. [89].

We turn now to the effects of uniaxial pressure along the c-axis. We simulate this by decreasing the value of c and relaxing the values of a and u until the forces over the atoms are below 1 meV/Å. The corresponding pressure is calculated using the compliance tensor. In Fig. 6.2 (a) we plot the (normalized) structural parameters versus pressure. The changes in the lattice parameters are of the same order of magnitude of those found in, e.g., TiO_2 [91]. We note that the expansion of the a parameter agrees remarkably well with the values predicted by the compliance tensor. The change in the u, which determines the Sn-O distance in the ab-plane, is weaker in magnitude than the change in a. This just indicates that it is more difficult to stretch the Sn-O bonds than to reduce the rectangular distortion of the base of the SnO_6 octahedra [82]. Figure 6.1 (b) compares the LDA band structures at P=0 and P=3.1 GPa, the latter corresponding to a 1% decrease of the c

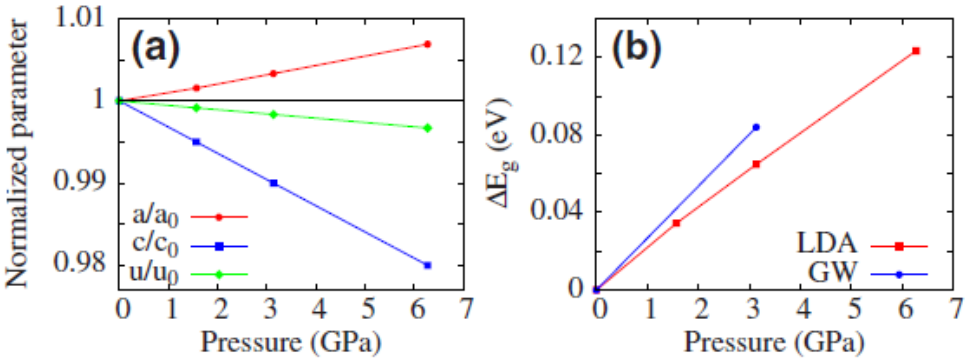

Figure 6.2: Effect of applied uniaxial pressure along the c-axis on (a) the structural parameters and (b) the band gap value.

value. For comparison, the valence band maxima at Γ are aligned. The band gap increases to 1.86 eV. As discussed in previous work [83, 85], the valence and conduction bands are mainly of bonding and antibonding characters, respectively. Hence, pressure tends to increase the bonding-antibonding split. Besides increasing the band gap, pressure affects more noticeably the states around -4 and 6 eV, which arise from the O(2p) states determining the structure of the SnO_6 octahedra. To take measure of the ability of the LDA to describe the change in energies due to pressure, we have also calculated the GW corrections at P=3.1 GPa. The values found at high symmetry points are indicated in Table 6.2. The change in quasiparticle energies is generally >1%. The change is, thus, important, given that the change in structural parameters is ≤1%. As can be seen, the GW corrections tend to increase overall. Regarding E_g, it raises to 3.94 eV. This corresponds to a rate of increase with a pressure of 27 meV/GPa, while it is of 21 meV/GPa in the LDA case, i.e., ∼29% lower. These rates are comparable to those of other semiconductors, such as TiO_2 and CdSe [91, 92]. We caution, however, that more accurate estimations may be needed. Indeed, in Fig. 6.2 (b) we show the change of the LDA band gap with pressure, ΔE_g, for several pressure values. It appears that it is slightly nonlinear in the pressure range shown (the rate of change at low pressure would be 22 meV/GPa). We have also calculated m_e^* and m_p^* for P=3.1 GPa. The values found are given in Table 6.3. The increase of the m_e^* with pressure obeys to band repulsion. The change in the m_h^* , on the other hand, is more intriguing. The upper valence bands arise essentially from the O(2p) lone-pair states [83], which extend in the

ab-plane and do not participate in bonding. The increase of a with pressure allows these states to delocalize more, thus reducing $m^*_{h\perp}$. Concomitantly, the reduction of c tends to increase the repulsion between these states in the direction parallel to c, thereby enhancing $m^*_{h\parallel}$. In conclusion, the GW approximation predicts an E_g that is larger than the optical gap by at least 0.25 eV. Also, the GW approximation indicates that the effects of pressure on the quasiparticle energies are larger than predicted by the LDA. The quasiparticle effective masses, on the other hand, appear to be well estimated by the LDA. These findings are important for the understanding of greatly relevant properties of doped SnO_2 films in many optoelectronic applications.

6.3.2 CdO

To determine the quasiparticle band gap in CdO one should calculate the complete band structure since the VBM occurs along the Γ-L direction with the CBM located at Γ. However, in practice, the exact evaluation of the GW band structure for large number of k-points which constitutes different symmetry lines in the Brillouin zone can be an extremely demanding task compared to LDA calculation. Moreover the situation is further demanding due to the high value of plane-wave cut-off required by the modified Cd PP (Cd^{20+} PP) that is essential for a correct treatment of the self-energy operator. Thus in order to reduce the computational effort and time one can make use of Maximally-Localized Wannier Functions (MLWFs). The MLWFs offer a highly accurate method to interpolation of the LDA or GW band structure from a coarse k-point mesh in the irreducible Brillouin zone resulting in a much reduced computational effort. Here follows a brief introduction to the MLWFs, and to the procedure of interpolating GW band structure using MLWFs.

Wannier functions

The electronic ground state of a periodic solid is represented with Bloch functions $\psi_{n\mathbf{k}}$ at each band n and $\mathbf{k}$-point with norm-conserving PPs. An alternative representation of Bloch functions can be given in terms of spatially localized functions known as Wannier functions (WF) [93]. The WF centered on a lattice site $\mathbf{R}$, $\mathcal{W}_{n\mathbf{R}}(\mathbf{r})$, is written in terms of the set of Bloch states as

$$\mathcal{W}_{n\mathbf{R}}(\mathbf{r}) = \frac{V}{(2\pi)^3}\int_{BZ}\left[\sum_m U^{(\mathbf{k})}_{mn}\psi_{m\mathbf{k}}(\mathbf{r})\right]e^{-i\mathbf{k}\cdot\mathbf{R}}d\mathbf{k} \tag{6.1}$$

where V is the unit cell volume, the integral is over the Brillouin zone, and $U^{(\mathbf{k})}$ is a unitary matrix that mixes the Bloch states at each $\mathbf{k}$. $U^{(\mathbf{k})}$ is not

uniquely defined and different choices will lead to WF with varying spatial localizations. WFs are the solid-state equivalent of localized molecular orbitals [94, 95], and thus provide a chemical picture of the system. Following the method of Marzari and Vanderbilt [96], the MLWFs can be constructed by minimizing the spread, Ω, of the N generalized WFs defined as

$$\Omega = \sum_{n=1}^{N} \left[\langle \mathcal{W}_{n\mathbf{0}}(\mathbf{r}) | r^2 | \mathcal{W}_{n\mathbf{0}}(\mathbf{r}) \rangle - |\langle \mathcal{W}_{n\mathbf{0}}(\mathbf{r}) | \mathbf{r} | \mathcal{W}_{n\mathbf{0}}(\mathbf{r}) \rangle|^2 \right] \tag{6.2}$$

where we refer to the unit cell at the origin, since all sets of Wannier functions are equivalent within a lattice-vector translation, $\mathcal{W}_{n\mathbf{R}}(\mathbf{r}) = \mathcal{W}_{n\mathbf{0}}(\mathbf{r} - \mathbf{R})$.

As it is shown in Ref. [96] the spread functional Ω can be expressed in terms of $U_{mn}^{(\mathbf{k})}$ and the overlap matrix:

$$M_{mn}^{(\mathbf{k},\mathbf{b})} = \langle \psi_{m\mathbf{k}} | e^{i\mathbf{b}\cdot\mathbf{r}} | \psi_{\mathbf{k}+n\mathbf{b}} \rangle \tag{6.3}$$

where $\mathbf{b}$ are vectors connecting each $\mathbf{k}$-point to its near neighbors. Having Ω in terms of $U_{mn}^{(\mathbf{k})}$ and $M_{mn}^{(\mathbf{k},\mathbf{b})}$, the gradient of the spread functional can also be obtained from these quantities. Therefore, $M_{mn}^{(\mathbf{k},\mathbf{b})}$ becomes the principal ingredient used in the algorithm to minimize the spread.

The minimization algorithm is started from an initial approximation to $U_{mn}^{(\mathbf{k})}$. A set of N localized trial orbitals $g_n(\mathbf{r})$ is chosen corresponding to some rough initial guess for the MLWFs. This initial guess is given to the algorithm in the form of a $N_\mathbf{k} \times N$ matrix:

$$A_{mn}^{(\mathbf{k})} = \langle \psi_{m\mathbf{k}} | g_n \rangle \tag{6.4}$$

ABINIT builds the $M_{mn}^{(\mathbf{k},\mathbf{b})}$ matrix after a ground state calculation. It is then transformed to the Wannier90 [97] code, which minimizes the spread Ω with respect to the set of $U_{mn}^{(\mathbf{k})}$ to obtain MLWFs.

Given a set of LDA or GW eigenvalues, $\epsilon_{n\mathbf{k}}$, calculated on a homogeneous grid of $\mathbf{k}$-points, we express the Hamiltonian $H_{mn}^{(\mathbf{k})} = \epsilon_{n\mathbf{k}}$ in the Wannier gauge representation,

$$H_{mn\mathbf{k}}^{\mathcal{W}} = \sum_{i=1}^{N} (U_{im}^{(\mathbf{k})})^\dagger U_{in}^{(\mathbf{k})} \epsilon_{n\mathbf{k}}, \tag{6.5}$$

where $U_{mn}^{(\mathbf{k})}$ are the matrices that minimize the spread of the Wannier Functions. We then obtain the Hamiltonian in real space using a discrete Fourier transform,

$$H_{mn\mathbf{R}}^{\mathcal{W}} = \frac{1}{N_\mathbf{k}} \sum_{\mathbf{k}} e^{-i\mathbf{k}\cdot\mathbf{R}} H_{mn\mathbf{k}}^{\mathcal{W}}, \tag{6.6}$$

where $N_{\mathbf{k}}$ is the number of $\mathbf{k}$-points in the mesh.

Assuming $|H^{\mathcal{W}}_{mn\mathbf{k}}|$ to decay fast with $|\mathbf{R}|$, we apply an inverse Fourier transform to calculate the Hamiltonian at any arbitrary $\mathbf{k}'$ point,

$$H^{\mathcal{W}}_{mn\mathbf{k}'} = \sum_{\mathbf{R}} e^{i\mathbf{k}'\cdot\mathbf{R}} H^{\mathcal{W}}_{mn\mathbf{k}'} \tag{6.7}$$

The final step is to diagonalize $H^{\mathcal{W}}_{mn\mathbf{k}'}$ to find the interpolated energies $\epsilon_{n\mathbf{k}'}$.

Interpolation procedure

GW or LDA band structure interpolation based on MLWFs is a highly accurate method because it preserves valuable information about band connectivity. Hence, band crossings, avoided crossings and degeneracies are treated correctly at a low computational cost [98, 99]. In the LDA case, MLWFs are constructed by passing the LDA wavefunctions $\psi^{LDA}_{n\mathbf{k}}$ and the LDA eigenvalues $\epsilon^{LDA}_{n\mathbf{k}}$ in the full irreducible Brillouin zone to the Wannier90 code. Then, one uses the post-processing tools of Wannier90 to interpolate the band structure. In the GW case, the procedure is equivalent; one has to pass to Wannier90 the GW quantities instead of the LDA ones. It should be noted that since we perform the G_0W_0 calculations, only the LDA eigenvalues are replaced by the GW eigenvalues. Thus to construct the quasiparticle band structure we just calculate the GW corrections at a reduced set of k-points of the irreducible Brillouin zone, ABINIT further uses symmetry operations to obtain the corrections corresponding to the full irreducible Brillouin zone. Finally the post-processing tools of the Wannier90 code lead to the interpolated quasiparticle band structure.

Results

Let us first consider the LDA band structure, as shown in Fig. 6.3(a), calculated with the modified Cd^{20+} PP at the optimized lattice constant of 4.65 Å. The Cd^{20+} PP leads to a marginal opening of the band gap in contrast to the Cd^{12+} PP where the CBM crosses the Fermi energy indicating semimetallic nature (refer to Section 3.3 in chapter 3). The LDA band gap at the Γ point is 1.47 eV larger than 0.80 eV obtained with the Cd^{12+} PP. Thus we obtain an indirect band gap of 0.13 eV with the Cd^{20+} PP. The Cd-*d* energy levels lie around $\sim$-7 eV and are at higher binding energy compared to the experimental result of -9.1 eV below the VBM.

Now we move on to the Wannier interpolation scheme. In order to determine the number of k-points to realize a converged band structure using MLWFs, we first apply the technique to LDA results. We have used a regular

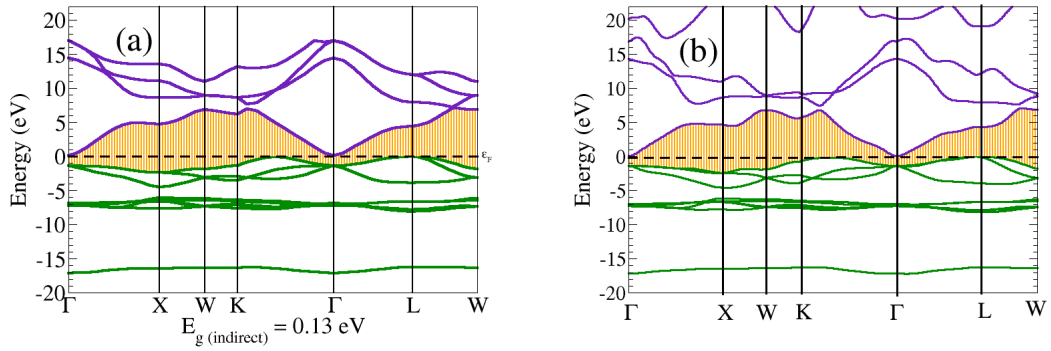

Figure 6.3: (a) LDA and (b) Wannier interpolated LDA band structure (using 4x4x4 Monkhorst-Pack k-point mesh) of CdO. The valence bands are virtually indistinguishable and the CBM dispersion is also well reproduced. However the higher conduction bands in the interpolated band structure are different from their LDA counterpart since they lie outside the energy window considered for interpolation.

4x4x4 Monkhorst-Pack k-point mesh which yield 8 k-points in the irreducible Brillouin zone and 64 k-points in the complete Brillouin zone. The MLWFs are constructed from Cd centered s, p, d and O centered s, p guiding functions and further, using the post-processing tools of the Wannier90 code, the Wannier-interpolated band structure is calculated. We exclude the deep lying semi-core bands corresponding to Cd $4s$ and $4p$ orbitals in the computation of band structure. The Wannier interpolated LDA band structure is presented in Fig. 6.3(b). The interpolated band structure is virtually indistinguishable compared to the LDA counterpart for all the valence bands and CBM. Thus the 4x4x4 Monkhorst-Pack k-point mesh, i.e. computation at 8 k-points in the irreducible Brillouin zone, is sufficient to reconstruct the band structure using the Wannier interpolation scheme.

Next, we calculate the quasiparticle corrections in the full irreducible Brillouin zone selected using the same 4x4x4 Monkhorst-Pack k-point mesh. For a quantitative comparison, in Table 6.5 we give the LDA and GW direct gaps at high symmetry points in the first Brillouin zone. With the Cd^{20+} PP we obtain significant quasiparticle corrections to the LDA eigenvalues. The GW band gap at the Γ point is 2.88 eV. It should be noted that the quasiparticle corrections depend on the k-point.

Table 6.4: Quasiparticle energy corrections to the energy gap at high symmetry points (values are in eV).

k point	Γ	X
LDA	1.47	7.12
GW	2.88	9.21
ΔE	1.41	2.09

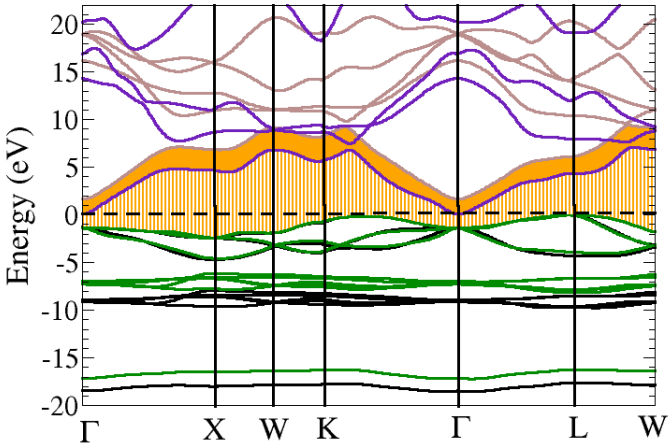

Figure 6.4: Wannier interpolated LDA and GW band structure of CdO.

Again, the MLWFs are constructed from Cd centered s,p,d and O centered s,p guiding functions and the Wannier-interpolated GW band structure is calculated further, using the post-processing tools of the Wannier90 code. We only supply the GW eigenvalues at 8 k-points in the irreducible Brillouin zone for this computation.

The full Wannier-interpolated LDA and GW band structures are compared in Fig. 6.4. The LDA valence band is shown with green lines while the GW valence bands are shown by black lines. The conduction bands are depicted using blue curves for the LDA part while brown curves show the GW counterpart. Also the striped orange part represents the band gap for LDA part and solid orange area represents the quasiparticle correction to the CBM.

Table 6.5: Wannier-interpolated band gap, position of Cd-d states (in eV) and the band mass (in units of the electron mass, m_e).

	LDA	GW	Expt.
E_g (indirect)	0.13	1.68	1.2 -2
E_g (direct)	1.2	2.88	2.32
E_d	$\sim$ -7	$\sim$ -9	-9.1
m_e^* (along Γ-X)	0.22	0.22	0.21

The band dispersion with LDA and GW are similar for the upper part of the valence band. The Cd-d energy levels, however, are shifted downwards and positioned at $\sim$-9 eV in the GW band structure. These levels show a good agreement with the reported experimental value of -9.1 eV. The conduction band dispersion in the LDA and GW band structure are quantitatively different at high symmetry points, such as X, L, reflecting the k-point dependence of the quasiparticle energy corrections. The indirect band gap obtained using the Wannier-interpolated GW band structure is $\sim$ 1.68 eV and is in agreement with the reported range of 1.2-2 eV in the experiments [47]. We have also calculated the electron effective mass along the Γ-X direction for the Wannier interpolated CBM. The calculated band mass (along Γ-X), for both the LDA and GW band structure is 0.22 m_e and is also in good agreement with the experimental value of 0.21 m_e [100].

Chapter 7

TCOs based on ZnX_2O_4 (X=Al,Ga and In) spinel structure

7.1 Introduction

Zinc aluminate ($ZnAl_2O_4$) and Zinc gallate ($ZnGa_2O_4$) are wide band gap semiconductors with reported band gaps of 3.8-3.9 eV and 4.4-5.0 eV, respectively [101]. These wide band gap structures are useful in photoelectronic and optical applications and are being studied as candidate materials for reflective optical coatings in aerospace applications [102, 103]. Because of their wide band gap, they have attracted particular interest as possible TCO materials[1][104, 105]. For an effective materials design for this purpose, a sound knowledge of the electronic properties of these materials is essential. The structural properties and electronic structure of these materials have been studied previously [105, 106, 107] within the framework of standard density functional theory (DFT) [31, 32]. But these studies have been hampered by the well known problem that within that framework the band gap of semiconductors and insulators is severely underestimated [23]. Indeed, although structural parameters obtained within DFT are in quite good agreement with experiment, the band gaps are not. For instance, the calculated DFT band gap for $ZnGa_2O_4$ is 2.79 eV [106], an underestimation of 42% with respect to the experimental value. Interestingly, in the case of $ZnAl_2O_4$, the DFT band

[1]This chapter is based on the work published as - H. Dixit, Nandan Tandon, R. Saniz, S. Cottenier, D. Lamoen, B. Partoens, V. Van Speybroeck and M. Waroquier: "*Electronic structure and band gap of zinc spinel oxides beyond LDA: $ZnAl_2O_4$, $ZnGa_2O_4$, and $ZnIn_2O_4$* ", New Journal of Physics, 13, 063002 (2011).

gap is found to be 4.11 eV [106], which is roughly 5% higher than the experimental value. This is in stark contrast with the common trend and has lead Sampath *et al.* [106] to indicate that since the band gaps in Ref. [101] were derived from reflectance measurements of powder samples, a correction due to the particle-size dependence of light scattering may be necessary. Thus, the exact band gap value in $ZnAl_2O_4$ is presently an open question.

Fortunately, there are currently first-principles techniques that have been demonstrated to describe accurately the electronic structure of semiconductors and insulators. First we mention the G_0W_0 results and thereafter the results obtained using the recently proposed Tran-Blaha Modified Becke-Johnson (TB-mBJ) potential [108, 109]. This TB-mBJ potential will be discussed in detail in the following chapter. At present we may consider it as a scheme which reliably estimates the band gaps in solids at much reduced computational effort. Thus, here we apply these two methods to study systematically the series ZnX_2O_4, where X=Al, Ga and In are successively heavier elements from group III of the periodic table. We focus not only on obtaining accurate values of the fundamental band gap in these materials, but also on other key properties in TCOs, such as the second band gap (between the two lowest conduction bands) and the electron effective mass.

Transition metal oxides can be particularly challenging for first-principles calculations and this remains true for the GW method as well. Indeed, while there is ample evidence that the non-self-consistent GW approximation works well in combination with pseudopotentials (PPs) and a plane wave basis set within DFT-LDA [71], it has been observed that it can underestimate band gaps in transition metal oxides if no particular care is taken. The exchange part of the self-energy operator within the GW approximation is inadequately treated if only cation d-states are included as valence states [69]. Therefore, a 'standard' PP with only semi-core d-states is not suitable to calculate a GW band gap in transition metal oxides. For ZnO, we have found before that the 20-electron cation PP is essential for an adequate treatment of the exchange part of the self-energy within the GW approximation [86]. In this chapter we also address the question whether the complete $n = 3(4)$ shell must be included in the Ga(In) PP to obtain accurate GW results. Thus, in this chapter we present the non-self-consistent GW band gap calculated with two sets of PP's. First, with the 'standard' PP containing the semi-core states ($3d^{10}, 4s^2$ for Zn, $3d^{10}, 4s^2, 4p^1$ for Ga and $4d^{10}, 5s^2, 5p^1$ for In) and then with the entire $n = 3(4)$ shell treated as valence ($3s^2, 3p^6, 3d^{10}, 4s^2$ for Zn, $3s^2, 3p^6, 3d^{10}, 4s^2, 4p^1$ for Ga and $4s^2, 4p^6, 4d^{10}, 5s^2, 5p^1$ for In). We

discuss how these different PP's affect structural properties as well as the GW band gap. The accuracy of these PP's is examined by comparison with all-electron calculations with LDA and TB-mBJ potential.

7.2 Computational details

7.2.1 Pseudopotentials

We use two sets of *ab initio* norm-conserving PP's for Zn, Ga, and In as defined below:

(a) the 'standard' Zn^{12+}, Ga^{13+} and In^{13+} PP's in which the semi-core $3d(4d)$ state is treated as valence. The inclusion of the wide $d-$orbital is necessary for a correct description of the structural properties by DFT for group-IIB and IIIA elements. Hereafter this set of PP will be referred as PP1.

(b) the Zn^{20+}, Ga^{21+} and In^{21+} PP generated with the entire $n = 3(4)$ shell as valence. Since the exchange energy contribution to the self-energy operator depends on the spatial overlap of atomic orbitals, the 's' and 'p' states are also included in the valence for the adequate treatment of the self-energy. It should be noted that we do not construct our Zn^{20+}, Ga^{21+} and In^{21+} PP for the neutral Zinc and Gallium(Indium) atom, but rather for the ion with the $4s(5s)$ and $4p(5p)$ state unoccupied. The cut-off radius for the Zn and Ga atom is chosen to be 0.43 Å for $3s, 3p$ and $3d$ orbitals and 1.38 Å for $4s$ and $4p$ orbitals. For the In atom we choose a cut-off radius of 0.52 Å for $4s, 4p$ and $4d$ orbitals and 1.2 Å for $5s$ and $5p$ orbitals. These values for the cut-off radius show the smallest transferability error for ionic configurations of Zn/Ga/In (neutral, +1 and +2), at the cost of an increased plane wave cut-off. We have used 90 Ha as the cut-off energy for plane waves, when $Zn^{20+}/Ga^{21+}/In^{21+}$ PP is used. The PP becomes harder with the inclusion of localized core orbitals in the valence. These pseudopotentials are generated with the OPIUM [40] code according to the Troullier-Martins [67] method with Perdew-Zunger LDA [68]. Hereafter this set of PP will be referred as PP2.

7.2.2 DFT, GW and TB-mBJ

The electronic structure and the quasiparticle(GW) correction to the band gap at the Γ point have been calculated using the plane wave pseudopotential code ABINIT [24, 25, 26]. For the electronic structure the plane wave cutoff is chosen by using the total energy convergence criterion of 2×10^{-2}

eV. The atomic positions and structural parameters have been optimized by calculating the Hellmann-Feynman forces. The stresses are minimized with the criterion of 2×10^{-5} eV/Å^3. We choose a 4x4x4 Monkhorst-Pack [38] k-point mesh, which yields 10 k-points in the irreducible Brillouin zone.

The parameters used within ABINIT to calculate the self-energy, are optimized with a convergence criterion of 0.01 eV for the band gap at Γ. We have found that, for both the screening and the self-energy calculation 600 bands are sufficient to converge the GW band gap. The dielectric matrix is calculated with the plasmon-pole model [23] and is used to calculate the screening.

All-electron calculations with the APW+lo method were performed using the WIEN2k code [110, 111]. In this method, the wavefunctions are expanded in spherical harmonics inside non overlapping atomic spheres of radius R_{MT} and in plane waves in the remaining space of the unit cell (the interstitial region). The radii for the muffin tin spheres were taken as large as possible without overlap between the spheres: $R_{MT}^{Zn} = 2.0$, $R_{MT}^{Al} = 1.9$, $R_{MT}^{Ga} = 2.0$, $R_{MT}^{In} = 2.3$ and $R_{MT}^{O} = 1.6$ bohr. The maximum ℓ for the expansion of the wave function in spherical harmonics inside the spheres was taken to be ℓ_{max} =10. The charge density was Fourier expanded up to G_{max} =16 Ry. Atomic positions were relaxed until the forces were below 0.5 mRy/bohr. The plane wave expansion of the wave function in the interstitial region was truncated at K_{max}= 4.7 bohr^{-1}. A converged k-mesh of 16 k points in the irreducible part of Brillouin zone was used.

7.3 Result and discussion

7.3.1 Structural properties and electronic band structure using DFT

The ZnX_2O_4 (X=Al, Ga, and In) adopt the normal spinel structure (space group $Fd\bar{3}m$). They are characterized by the lattice parameter a and an internal parameter u. The Zn atoms are located at Wyckoff positions 8a (1/8, 1/8, 1/8) tetrahedral sites, whereas Al, Ga or In atoms are located at the 16d (1/2, 1/2, 1/2) octahedral sites and the O atoms at 32e (u, u, u) of the face-centered cubic structure as shown in Fig. 7.1. It has been shown by experiment [113] as well as theory [114] that for these compounds ($ZnAl_2O_4$ and $ZnGa_2O_4$) the normal spinel structure is more favorable than the inverse spinel structure, where the tetrahedral sites are occupied by the X atoms

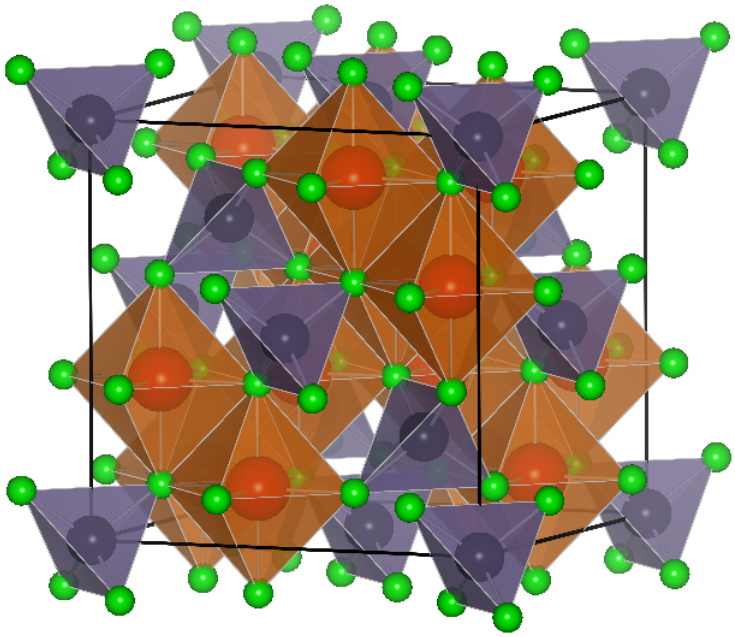

Figure 7.1: ZnX_2O_4 spinel structure: the Zn atoms in blue color are tetrahedrally coordinated with the oxygen atoms shown in green and the X atom (in red) are octahedrally coordinated with the oxygen atoms. The image is generated using VESTA [112].

Table 7.1: Optimized lattice constant (in Å) and internal coordinate (u) of the three spinel compounds calculated using either pseudopotentials (PP1 and PP2, see text) or an all-electron method (AE).

Compound	PP1	PP2	AE	Experiment[113]
$ZnAl_2O_4$	7.9893	7.9849	8.0464	8.086
u	0.2642	0.2647	0.2638	0.2636
$ZnGa_2O_4$	8.2644	8.3284	8.2693	8.33
u	0.2611	0.2611	0.2612	0.2617
$ZnIn_2O_4$	8.8420	8.8790	8.9297	–
u	0.2553	0.2556	0.2558	–

and the octahedral sites are occupied by equal numbers of Zn and O atoms. We therefore consider only the normal spinel structure in this work. The structural properties are summarized in Table 8.1, which shows the optimized lattice constant and 'u' parameter for both sets of PP's and for an all-electron calculation, in all cases with plain LDA. For comparison the experimental values are also listed. Experimental data are not available for $ZnIn_2O_4$. Lattice constants and internal parameters for both pseudopotentials are in good agreement with the corresponding all-electron data and all calculated values are in good agreement with experiment, apart from the usual over binding behavior of LDA. The small differences between the results obtained by the two pseudopotentials and by the all-electron calculations, suggest that our newly generated $Zn^{20+}/Ga^{21+}/In^{21+}$ PP (PP2) is of an acceptable accuracy.

The electronic structure and projected density of states (PDOS) for ZnX_2O_4 (X=Al, Ga, and In) oxides, calculated using DFT/LDA, are shown in Fig. 7.2. $ZnAl_2O_4$ is direct band gap material with both the valence band maximum and the conduction band minimum at Γ, while $ZnGa_2O_4$ and $ZnIn_2O_4$ have an indirect band gap as the valence band maximum is along Γ-K direction (see inset). The PDOS shows a significant p-d hybridization between the Zn-d and O-p orbitals. This is one of the reasons why the DFT-LDA band gap of $ZnGa_2O_4$ is strongly underestimated compared to the experimental value as shown in Table 7.3. The calculated band gap at the Γ point is 2.82 eV compared to the experimental values of 4.4-5.0 eV. The PDOS for $ZnAl_2O_4$ also shows the p-d hybridization, however the calculated band gap of 4.25 eV overshoots the experimental value of 3.8-3.9 eV. It is well known that DFT typically underestimates the band gap, as mentioned above, but it does even more so in the case of p-d hybridized systems.

Thus the apparent band gap overestimation by the DFT-LDA in the case of $ZnAl_2O_4$ is anomalous. Previous theoretical calculations on LDA level [106, 107, 105] found results similar to ours and have suggested that the experimental results require revision. In the case of $ZnIn_2O_4$, the DFT-LDA band gap is found to be 1.71 eV. No experimental information is available to compare with, as this material has not been synthesized experimentally.

The electron effective mass is listed in Table 7.2 for ZnX_2O_4. The effective mass is calculated along [111] direction and it compares well with the known TCO materials such as ZnO ($0.23m_e$) and In_2O_3:Sn ($0.30m_e$). The effective mass with TB-mBJ is larger than LDA; as also observed by Kim *et al.*[115].

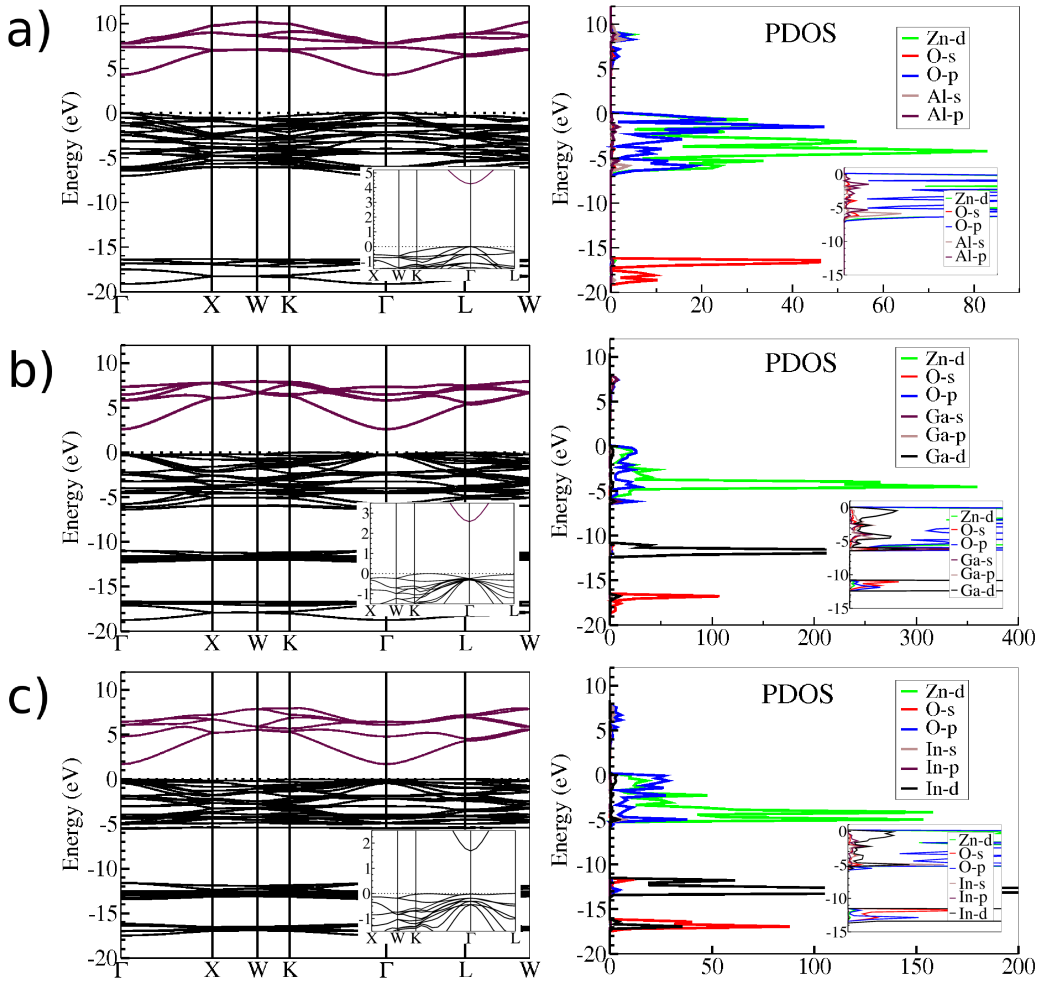

Figure 7.2: LDA (PP2) - electronic band structure and projected density of states (PDOS) for a) $ZnAl_2O_4$ b) $ZnGa_2O_4$ and c) $ZnIn_2O_4$ spinel. The inset figure in the band structure plot shows direct/indirect nature of the band gap, while the inset figure in the PDOS plot shows the detailed composition for upper part of the valence band.

Another key property of a good TCO is a large second band gap between the two lowest conduction bands. The larger value of the second band gap lowers the plasma frequency and results in reduced optical absorption [53]. We find the second band gap ($E_g^{(2)}$) is 3.08 eV for $ZnAl_2O_4$, 3.10 eV for $ZnGa_2O_4$ and 3.13 eV for $ZnIn_2O_4$ with LDA. This shows that the ZnX_2O_4

Table 7.2: Effective mass of electron (in units of free electron mass m_e) calculated along [111] direction.

Compound	m_e^* (PP1)	m_e^* (APW+lo)	m_e^* (TB-mBJ)
$ZnAl_2O_4$	0.37	0.35	0.44
$ZnGa_2O_4$	0.23	0.25	0.35
$ZnIn_2O_4$	0.17	0.22	0.34

spinels can be n-type conducting and remain transparent over the visible spectrum, making them attractive host materials for TCO.

To predict the band gap values accurately, and to describe the conduction bands, we performed a calculation of the excited states using the GW approximation as well as the TB-mBJ potential. Our findings are reported in the following sections.

7.3.2 GW and TB-mBJ band gaps

In the following we present the quasiparticle band gaps obtained with the two set of PP's (PP1 and PP2) for Zn, Ga and In (Table 7.3). We discuss $ZnGa_2O_4$ first. The band gap with plain LDA is about 2.6 eV, with minor influences due to the type of PP or the use of an all-electron method. This gap is 2 eV below the experimental value. When the GW method is used for the standard PP (PP1), the resulting band gap is 1.2 eV larger. This is considerably closer to experiment, but still almost 1 eV too small. If however, we use the Zn^{20+} and Ga^{21+} PP (PP2), we obtain a band gap of 4.57 eV, which agrees nicely with the experimental value. Hence, we confirm that similar to ZnO [86], the Zn^{20+} and Ga^{21+} PP (PP2) are essential for an adequate treatment of the self energy. The TB-mBJ band gap is similar to the GW (PP2) band gap. To elucidate the contribution of the Ga^{21+} PP to the self-energy, we now provide an interesting comparison. We have also calculated the GW band gap of $ZnGa_2O_4$ using a combination of Zn^{20+} and Ga^{13+} PP. The calculated GW band gap is 4.39 eV and the quasiparticle correction to the band gap is 1.54 eV which is lower than 1.74 eV when the Zn^{20+} and Ga^{21+} PP is used. This confirms that PP2 should be used for both the cations: Zn and Ga.

For $ZnAl_2O_4$, the situation is somewhat different. As mentioned in Section 7.3.1, the LDA band gap is larger than the experimental value, which is an anomalous situation. LDA is known to provide band gaps that are

considerably too small. Indeed, applying GW with the standard PP (PP1) gives a 1.6 eV increase of the band gap. Using the Zn^{20+} and Al^{3+} PP (PP2) increases the band gap further by yet another 0.7 eV. The final value of 6.55 eV is somewhat larger than the TB-mBJ value of 6.18 eV, and either of both is more than 2 eV larger than the reported experimental value. This strongly suggests that the experimental value is indeed incorrect, and a re-measurement is suggested.

$ZnIn_2O_4$ shows qualitatively similar behavior: using GW with the standard PP increases the band gap, while using PP2 rather than PP1 gives an additional increase. In contrast to the previous two compounds, the second step introduces the larger change. This is consistent with the observation that even at the LDA level the introduction of PP2 increased the band gap by 0.5 eV. The TB-mBJ band gap is again similar to the GW+PP2 value.

Table 7.3: The DFT-LDA, all-electron, GW and TB-mBJ band gap (E_g) at Γ, calculated with the optimized lattice constant (in eV).

DFT				
Compound	E_g^{PP1}	E_g^{PP2}	E_g^{APW+lo}	$E_g^{Expt.}$
$ZnAl_2O_4$	4.26	4.25	4.11	3.80-3.90
$ZnGa_2O_4$	2.63	2.82	2.53	4.40-5.00
$ZnIn_2O_4$	1.22	1.71	1.12	–
GW and TB-mBJ				
Compound	E_g^{PP1+GW}	E_g^{PP2+GW}	E_g^{TB-mBJ}	$E_g^{Expt.}$
$ZnAl_2O_4$	5.88	6.55	6.18	3.80-3.90
$ZnGa_2O_4$	3.88	4.57	4.71	4.40-5.00
$ZnIn_2O_4$	1.77	3.27	3.51	–

As Table 7.3 shows, the TB-mBJ band gaps fall within a range of at most 7% from the GW band gaps (PP2). This is a fair agreement when considering the large difference with the plain LDA band gaps. Possible reasons for the GW and TB-mBJ differences are (a) the fact that both band gaps are determined at the equilibrium lattice parameter as predicted by the corresponding code (ABINIT/WIEN2k) at LDA-level (Table 8.1), (b) the direct influence of the PP on the band gap, and (c) the fact that the GW band gaps are non-self-consistent values. The band gap evolution in ZnX_2O_4 when X moves down the group (X=Al,Ga,In) is shown in Fig. 7.3. The DFT, GW and TB-mBJ results show a similar trend. The band gap

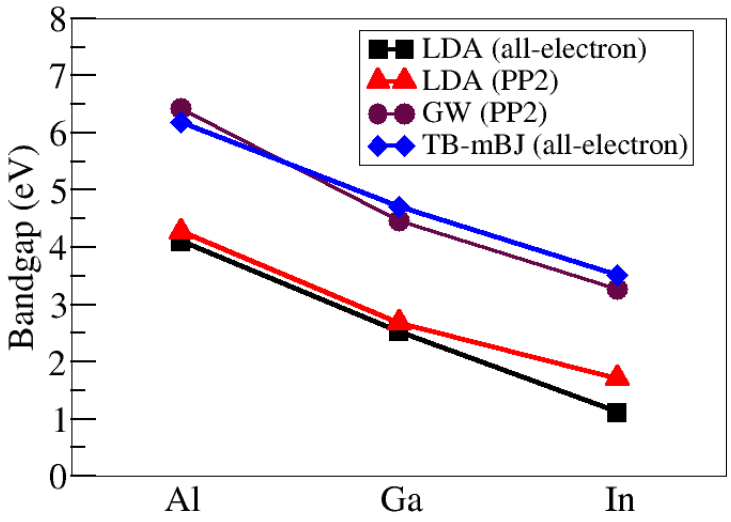

Figure 7.3: DFT-LDA, all-electron, GW and TB-mBJ band gap of ZnX_2O_4 (X=Al,Ga and In) in spinel oxides.

decreases with heavier cation substitution in the ZnX_2O_4 spinel oxide. Al has no d-states, while both Ga and In possess filled semi-core d-states which lie mainly around -12 eV in the valence band. However, note from the PDOS shown in the insets in Fig. 7.2 that these d-states are also present in the region -5 to 0 eV in the valence band. This indicates that these d-states increase the coupling with the O-2p levels. Therefore we suggest that the fundamental electronic band gap decreases through enhanced *p-d* coupling below the valence band while moving from Al to Ga. Since the In-d orbitals have larger spatial extension compared to the Ga-d orbital, the band gap is decreased further when Ga is replaced by In.

7.3.3 Formation enthalpy

Table 7.4: Calculated reaction energies of ZnX_2O_4 (X= Al, Ga and In) spinel oxide.

Reaction	Reaction energy (eV)
$ZnO + Al_2O_3 \rightarrow ZnAl_2O_4$	-0.83
$ZnO + Ga_2O_3 \rightarrow ZnGa_2O_4$	-0.90
$ZnO + In_2O_3 \rightarrow ZnIn_2O_4$	+0.53

Experimentally the $ZnIn_2O_4$ spinel structure has not been observed and thus there are no experimental reports on the band gap of $ZnIn_2O_4$. To examine the stability of ZnX_2O_4 spinel oxides we calculate the enthalpy of the following reaction with standard PP (PP1) at the LDA-level:

$$ZnO + X_2O_3 \rightarrow ZnX_2O_4$$

The enthalpy of the reaction is obtained by taking the difference between the total energy of the systems constituting the reaction. ZnO (wurtzite), α-Al_2O_3(corundum), β-Ga_2O_3 and In_2O_3(bixbyite) are all well-known compounds. The total energy of these compounds is calculated at optimized lattice parameters. The calculated enthalpy of this reaction is listed in Table 7.4. The calculated enthalpies are -0.83 and -0.90 eV for $ZnAl_2O_4$ and $ZnGa_2O_4$ respectively, indicating that these spinel structures are stable. However for the $ZnIn_2O_4$ the reaction enthalpy is +0.53 eV indicating that the formation of the $ZnIn_2O_4$ spinel structure is thermodynamically unfavorable. This appears to be correlated with the crystal geometry as explained below. A building block of the spinel structure is a distorted oxygen octahedron that contains one atom of element X. Tab.7.5 lists how the average O-O distance and O-X distance for this octahedron depend on X: the bond lengths are almost identical for X=Al and X=Ga, and increase by more than 10% for X=In. A similar octahedron appears in the corundum structure. The corresponding average bond lengths are given as well: there is 5% increase when Al is replaced by Ga, and more than 10% increase when Al is replaced by In. The latter agrees with the spinel case. The difference between corundum and spinel are the small bond lengths for the $ZnGa_2O_4$ spinel. Apparently such small bond lengths cannot be maintained for $ZnIn_2O_4$, which renders this crystal unstable.

Table 7.5: Average bond lengths (Å) for the X-containing distorted oxygen octahedron in the spinel-type ZnX_2O_4 and the corundum-type X_2O_3. The data for the spinel stem from calculations in this work. The corundum data are experimental values from Refs.[116, 117, 118].

Bond	ZnX_2O_4			X_2O_3		
	Al	Ga	In	Al	Ga	In
$X-O$	1.88	1.89	2.17	1.92	2.00	2.16
$O-O$	2.66	2.68	3.07	2.68	2.80	3.03

7.4 Conclusions

We calculate the quasiparticle band gap with two sets of PP's for Zn, Ga and In. The quasiparticle corrections for ZnX_2O_4 (X=Al, Ga and In) are presented. Our results show that the Zn^{20+}, Ga^{21+} and Ga^{21+} PP's are essential to calculate the GW band gap. The calculated GW and TB-mBJ band gaps for $ZnGa_2O_4$ are 4.57 and 4.71 eV, respectively. These band gap values agree well with the experimental report of 4.40 - 5.00 eV. The predicted GW and TB-mBJ band gap for $ZnAl_2O_4$ are 6.55 and 6.18 eV respectively. It will be of great interest to see if future experimental work confirms these values. The DFT (PP and all-electron), GW and TB-mBJ band gaps for ZnX_2O_4 all show a similar trend: a band gap decrease upon substitution by a heavier cation. The TB-mBJ band gaps are in agreement with the GW counterparts for these compounds, which corroborates the claim that TB-mBJ provides accurate band gaps for only a small computational effort. The calculated formation enthalpy for the ZnX_2O_4 spinel oxide structure indicates that $ZnAl_2O_4$ and $ZnGa_2O_4$ are stable. However the formation of the $ZnIn_2O_4$ spinel structure is unlikely which is consistent with the fact that experimentally the $ZnIn_2O_4$ spinel structure has not been observed.

Chapter 8

Electronic structure with TB-mBJ scheme

8.1 Introduction

The electronic structure of TCOs has been a subject of enduring interest[1]. One important feature is the hybridization between metal d orbitals and oxygen p orbitals. DFT calculations can assess the strength of this hybridization and we have seen that the calculated Kohn-Sham [31, 32] band gaps obtained using popular approximations such as the LDA or the GGA are strongly underestimated. To correct this 'band gap problem' in DFT, two approaches may be adopted. First one is to follow the proper procedure and obtain the one-particle excitation from the self-energy operator using the G_0W_0 method. With the case studies of ZnO, CdO, SnO_2 and ZnX_2O_4 (X=Al,Ga and In) spinel we have seen that application of the G_0W_0 method is computationally very demanding. Moreover, a special care needs to be taken in the pesudopotentials used for adequate treatment of the self-energy. This makes the G_0W_0 method computationally inefficient when a large class of material systems needs to be studied. Thus use of G_0W_0 method is a challenging task for high throughput materials design [119] in which one creates a large database to establish the correlations between the structural and electronic properties of materials. Second approach is to improve the Kohn-Sham band gap itself. There are different schemes available, such as the optimized effective potential (OEP) [120, 121] method, hybrid functionals as proposed by Heyd,

[1]This chapter is based on the work published as - H. Dixit, R. Saniz, S. Cottenier, D. Lamoen and B. Partoens: "*Electronic structure of transparent oxides with the Tran-Blaha modified Becke-Johnson density functional*", J. Phys.: Condens. Matter 24, 205503 (2012).

Scuseria, and Ernzerhof (HSE) [35, 36], etc. to do that. Unfortunately, these schemes are computationally expensive compared to LDA or GGA. However, the recently proposed Tran-Blaha modified version of the Becke-Johnson potential (TB-mBJ) [109] has proved to be a successful method for accurate band gaps of semiconductors and insulators, and computationally it is as economical as LDA or GGA although its self-consistency cycle converges slower and therefore requires more iterations (a factor of 2-3). The TB-mBJ scheme is rapidly gaining popularity and a significant number of studies reporting the improvements in the band gaps have been published [122]-[131] since the original publication in 2009. An overview of all results available in the literature at present, is given in Fig.9.1. It is obvious from this data set that TB-mBJ predicts reasonable band gaps up to about 6 eV. In a few cases there are minor overestimations. Most of the deviations are small underestimations. For band gaps larger than 6 eV, the available data set suggests a tendency towards a small yet significant systematic underestimation. Occasionally there are cases where the deviation is rather large (Cu_2O, $NaCl$). Overall, TB-mBJ is a decent alternative for GW or hybrid functionals, achieving a comparable accuracy at a far lower cost.

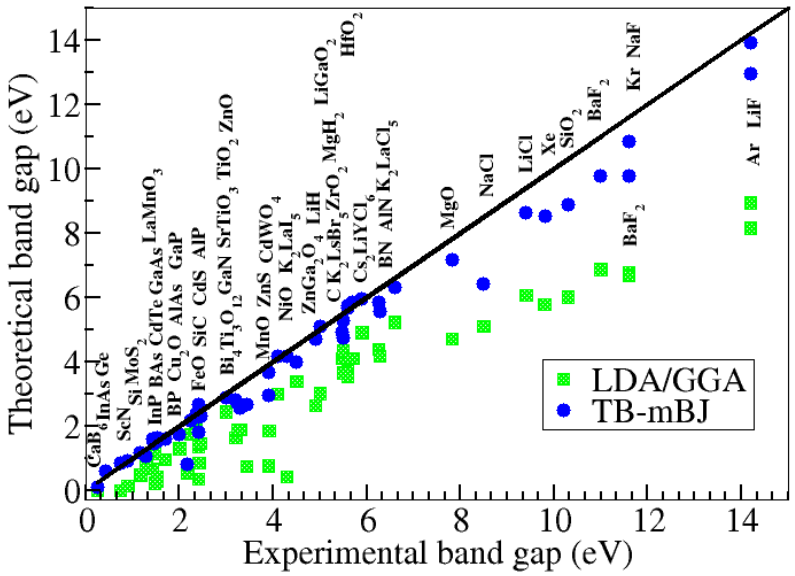

Figure 8.1: LDA/GGA and TB-mBJ versus experimental band gaps obtained from Ref. [122] to [131].

In the present chapter, we apply TB-mBJ to a group of oxides that are either used for their optical properties, or that have the potential to be so. These include n-type binary oxides namely - In_2O_3, ZnO, CdO and SnO_2 along with the p-type ternary oxides - the delafossite family $CuXO_2$ (X=Al,Ga,In) [3, 4, 5, 6, 7] and ZnX_2O_4 (X=Co,Rh,Ir) in the spinel structure [7, 8, 9]. Band gaps, band structures and effective electron masses obtained in this way are compared with what is predicted by the common PBE functional, and – where available – by G_0W_0. Trends in differences will be discussed.

8.2 Theory

The electronic structure of a periodic solid can be calculated using the well known Kohn-Sham equations given by

$$\left(-\frac{1}{2}\nabla^2 + \nu_{eff,\sigma}^{Kohn-Sham}(\mathbf{r})\right)\psi_{i,\sigma}(\mathbf{r}) = \epsilon_{i,\sigma}\psi_{i,\sigma}(\mathbf{r}) \tag{8.1}$$

where $\psi_{i,\sigma}$ are the one-electron wave functions. The Kohn-Sham effective potential, $V_{eff,\sigma}^{KS} = V_{ext} + V_H + V_{xc,\sigma}$, is the sum of external, Hartree and exchange-correlation (xc) terms. In this, the last term needs to be approximated while the other two terms are calculated accurately. The popular approximation for the exchange-correlation energy are LDA and GGA. Although the Kohn-Sham DFT is a fast and reliable method to calculate the electronic structure, the excited state properties like the band gap are severely underestimated for many semiconductors and insulators. Recently, Tran and Blaha have proposed an alternative scheme to improve the band gap calculation within DFT by modifying the Becke-Johnson potential which reads as follows:

$$\nu_{x,\sigma}^{BJ}(\mathbf{r}) = \nu_{x,\sigma}^{BR}(\mathbf{r}) + \frac{1}{\pi}\sqrt{\frac{5}{6}}\sqrt{\frac{t_\sigma(\mathbf{r})}{\rho_\sigma(\mathbf{r})}} \tag{8.2}$$

Here, $\rho_\sigma = \sum_{i=1}^{N_\sigma} |\psi_{i,\sigma}|^2$ is the electron density, $t_\sigma = (1/2)\sum_{i=1}^{N_\sigma} \nabla^*\psi_{i,\sigma} \cdot \nabla^*\psi_{i,\sigma}$ is the kinetic-energy density and

$$\nu_{x,\sigma}^{BR}(\mathbf{r}) = -\frac{1}{b_\sigma(\mathbf{r})}\left(1 - e^{-x_\sigma(\mathbf{r})} - \frac{1}{2}x_\sigma(\mathbf{r})e^{-x_\sigma(\mathbf{r})}\right) \tag{8.3}$$

is the Becke-Roussel (BR) exchange potential, which was proposed to model the Coulomb potential created by the exchange hole. In Eq.(8.3), x_σ is determined from a nonlinear equation involving $\rho_\sigma, \nabla\rho_\sigma, \nabla^2\rho_\sigma$ and t_σ. The b_σ is calculated with $b_\sigma = [x_\sigma^3 e^{-x_\sigma}/(8\pi\rho_\sigma)]^{1/3}$.

Tran and Blaha have introduced a parameter 'c' to change the relative weights of the two terms in the BJ potential and the modified potential (TB-mBJ) reads

$$\nu_{x,\sigma}^{TB-mBJ}(\mathbf{r}) = c\nu_{x,\sigma}^{BR}(\mathbf{r}) + (3c-2)\frac{1}{\pi}\sqrt{\frac{5}{6}}\sqrt{\frac{t_\sigma(\mathbf{r})}{\rho_\sigma(\mathbf{r})}} \tag{8.4}$$

The actual value of c in the TB-mBJ is calculated by

$$c = \alpha + \beta\left(\frac{1}{V_{cell}}\int_{cell}\frac{|\nabla\rho(\mathbf{r}')|}{\rho(\mathbf{r}')}d^3r'\right) \tag{8.5}$$

where V_{cell} is the unit cell volume and α and β are two free parameters whose values are α= -0.012 and β=1.023 bohr$^{1/2}$ according to a fit to experimental results.

8.3 Computational details

All-electron calculations with the APW+lo method were performed using the WIEN2k code [110, 111]. In this method, the wave functions are expanded in spherical harmonics inside non overlapping atomic spheres of radius R_{MT} and in plane waves in the remaining space of the unit cell (the interstitial region). The radii for the muffin tin spheres were taken as large as possible without overlap between the spheres: $R_{MT}^{In} = R_{MT}^{Sn} = R_{MT}^{Ga} = R_{MT}^{Cu} = R_{MT}^{Rh} = R_{MT}^{Ir}$ = 2.1, $R_{MT}^{Zn} = R_{MT}^{Cd} = R_{MT}^{Co}$ = 1.9, R_{MT}^{Al} = 1.6, and R_{MT}^{O} = 1.5 bohr. The charge density was Fourier expanded up to G_{max} =12 bohr^{-1}. The plane wave expansion of the wave function in the interstitial region was truncated at $R_{MT}K_{max}$= 9. A regular $4\times4\times4$ Monkhorst-Pack [38] k-point mesh is used for cubic structures such as In_2O_3, CdO, ZnX_2O_4 and also for the rhombohedral unit cell ($CuXO_2$). For the hexagonal unit cell a $3\times3\times2$ Monkhorst-Pack k-point mesh is used. All calculations are performed at the experimental lattice parameters, for a meaningful comparison.

8.4 Results

8.4.1 n-type binary oxides

Indium oxide:

In_2O_3 has a body centered cubic bixbyite structure, with 8 formula units per primitive cell. Each In atom is coordinated by six oxygen atoms in a distorted

octahedron. The unit cell contains 40 atoms and the lattice constant is 10.12 Å.

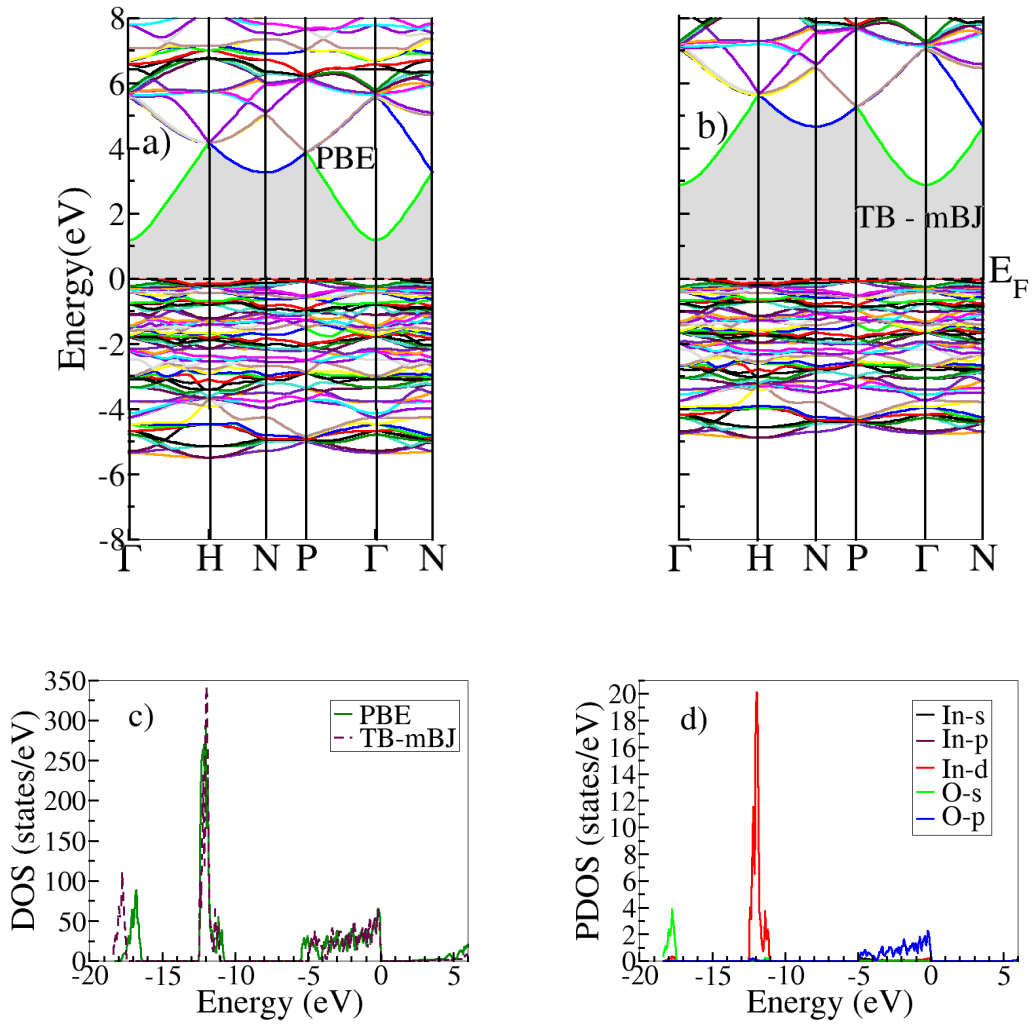

Figure 8.2: a) PBE and b) TB-mBJ band structure along with the c) total DOS with PBE and TB-mBJ and d) PDOS with TB-mBJ for In_2O_3.

The band structures along high symmetry lines in the Brillouin zone calculated with PBE and TB-mBJ are presented in Fig.8.2. It shows that In_2O_3 is a direct band gap semiconductor. Although the widely quoted direct band gap of In_2O_3 is 3.75 eV and indirect gap is 2.62 eV, recent experimental reinvestigation along with theoretical studies have concluded In_2O_3 to be a direct

band gap semiconductor with a band gap $\sim$ 3.1 eV [52]. The PBE band gap of 1.18 eV and is consistent with earlier reported results [53]. The TB-mBJ band structure shows a significant opening of the band gap and the calculated TB-mBJ gap is 2.90 eV, which compares well with both experimental and G_0W_0 result of 3.1eV [138].

We further analyze the band structure with the help of the density of states (DOS) and projected density of states (PDOS) plot as shown in the same figure. The PDOS shows that the valence band maximum (VBM) shows strong O-2p character and also an In-4d contribution indicative of p-d hybridization in In_2O_3. The low lying energy bands - around -12 eV have a strong In-4d character while the lowest energy band around -18 eV has O-2s character. A comparison with the DOS obtained by PBE shows that the valence band dispersion in TB-mBJ band structure has been narrowed by about 1eV in the region 0 to -6 eV. The In-4d levels have similar position while O-2s band has moved to higher binding energy of -19 eV with TB-mBJ.

Zinc oxide:

The lattice parameters used to calculate the band structure of wz-ZnO are: a=3.2489 Å, c=5.2049 Å, with the internal parameter u=0.381. From the band structure plot presented in Fig. 8.3, we observe that the band dispersion for the entire valence bands are similar in the PBE and TB-mBJ plot. The CBM at the high symmetry Γ point, however appears flattened in the TB-mBJ plot indicating havier band mass compared to PBE counterpart. The PBE band gap is 0.80 eV which opens up to 2.68 eV in the TB-mBJ band structure. The TB-mBJ gap is underestimated by 22% in comparison with experiment; however, it matches with the G_0W_0 results 2.49-2.51 eV [86, 73].

The PDOS calculated with TB-mBJ (see Fig. 8.3(d)) shows a strong p-d hybridization between Zn-3d and O-2p states in the region 0 to -6 eV. The Zn-3d states are placed around -5 eV and are shallow compared to the experimental estimate of $\sim$7-8 eV below the VBM. The O-2s states are positioned around $\sim$ -19 eV. The lowest valence band plotted in the TB-mBJ band structure is around -5.4 eV which is $\sim$ 0.8 eV higher than corresponding band in the PBE band structure. It is also clear from the comparison between total DOS plot as presented in Fig. 8.3(c), that the valence band dispersion in TB-mBJ is narrowed compared to PBE. This narrowing is suggested to be the origin of the remaining discrepancy between the TB-mBJ and experimental band gap by David J. Singh[126]. The O-2s state which form the lowest valence band is, however, at a higher binding energy in the TB-mBJ band structure compared to its PBE counterpart.

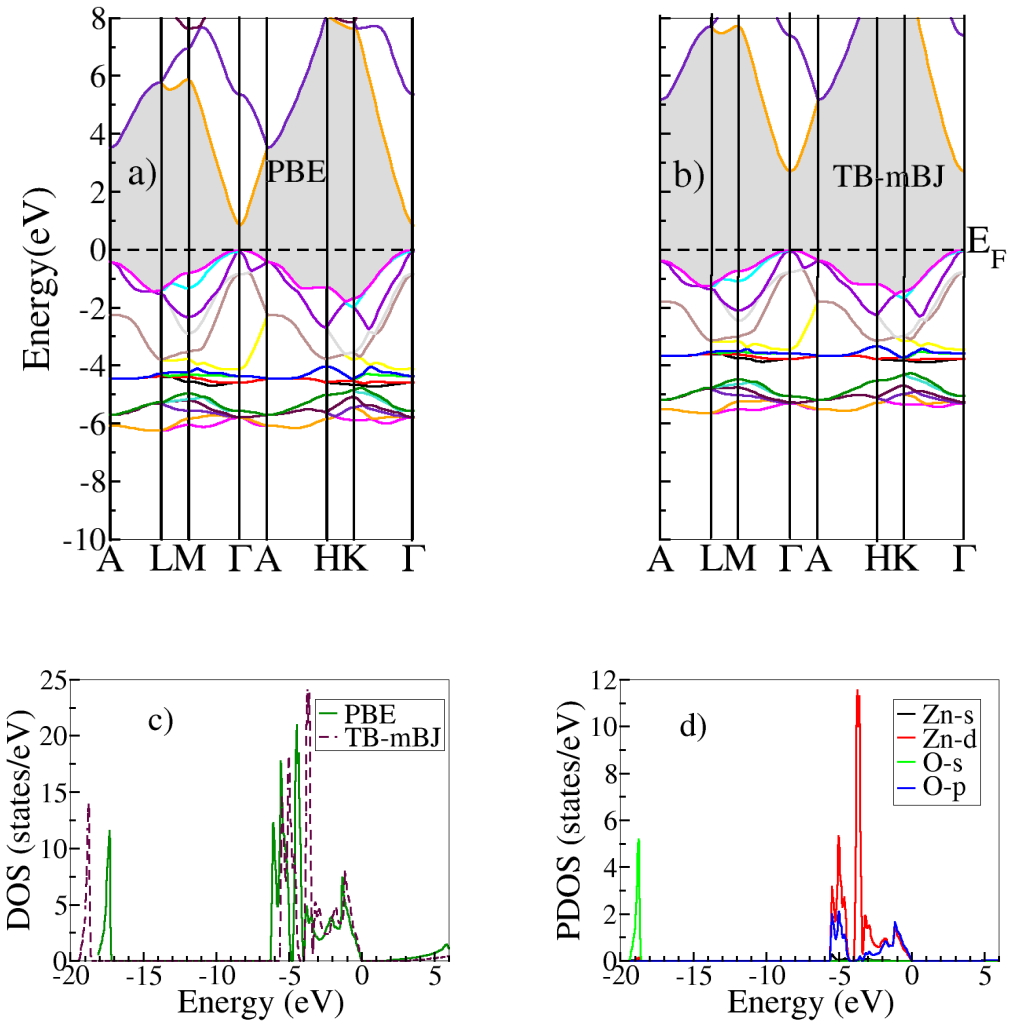

Figure 8.3: a) PBE and b) TB-mBJ band structure along with the c) total DOS with PBE and TB-mBJ and d) PDOS with TB-mBJ for ZnO.

Cadmium oxide:

CdO has the rocksalt structure and the experimental value of the lattice constant used is 4.64Å. The PBE band structure (see Fig.8.4(a)) shows CdO to be *semi-metallic* since the conduction band minimum (CBM) crosses the Fermi energy level (E_f). We obtain an indirect band gap of 1.82 eV with TB-mBJ. Although the band gap is widely quoted to be 0.55 eV at room temperature and 0.84 eV at 100 K, McGuinness et al. [47] have suggested a value

of ∼1.2 eV, while their own x-ray emission and absorption measurements on high purity samples yield a value of almost 2 eV. Also, recent G_0W_0 calculation results in a much larger value of 1.07 eV for the indirect gap [132]. Thus the calculated TB-mBJ gap is in agreement with the reported experimental range of 1.2-2 eV.

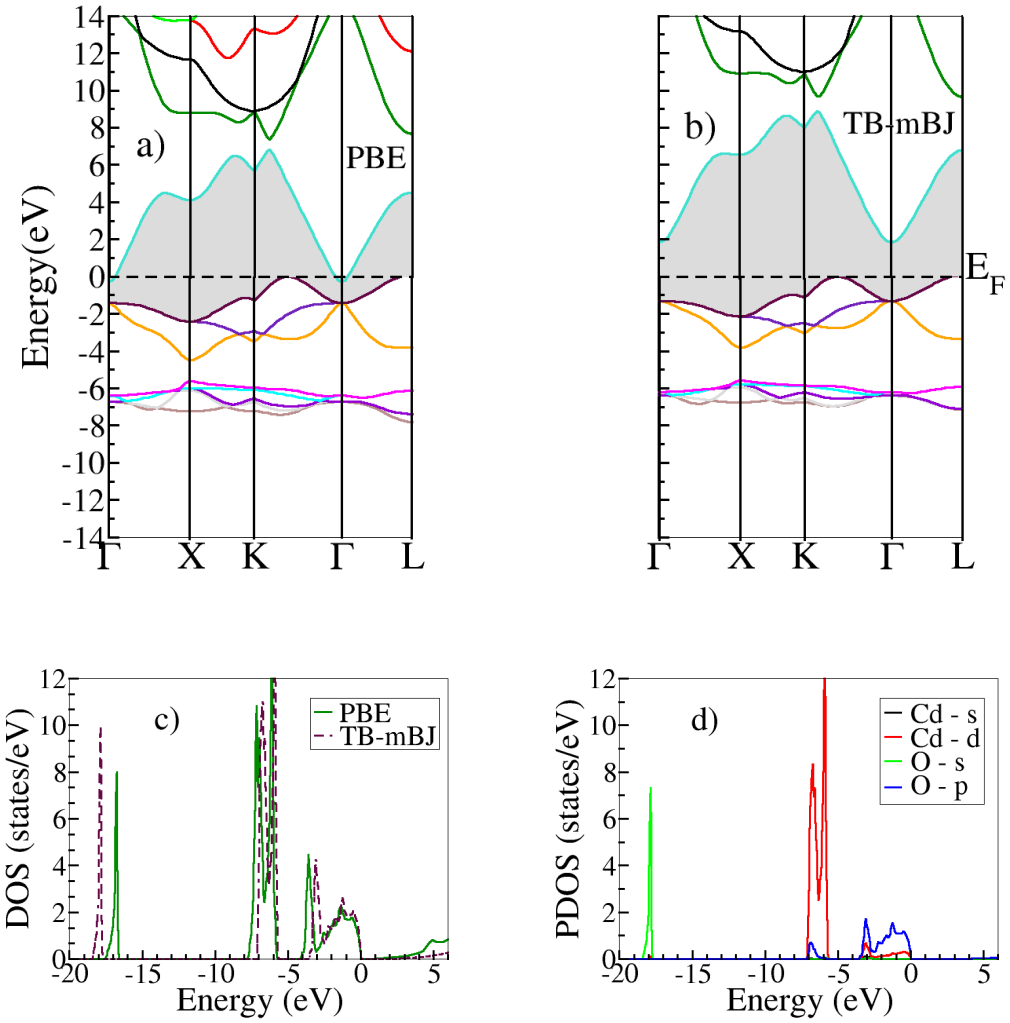

Figure 8.4: a) PBE and b) TB-mBJ band structure along with the c) total DOS with PBE and TB-mBJ and d) PDOS with TB-mBJ for CdO.

The PDOS of CdO (see Fig.8.4(d)) calculated with the TB-mBJ scheme also show *p*-*d* hybridization. The VBM is mainly derived from the O-2*p* states

which are hybridized with the Cd-4*d* states. The Cd-4*d* energy levels around ∼-6.5 eV are at higher binding energy compared to the experimental result of -8.8 eV below VBM. The lowest valence band at ∼ -18 eV shows O-2*s* character. The comparison between the total DOS plots of CdO (Fig.8.4(c)) show a similar trend as observed in the case of ZnO. The dispersion of the upper valence bands is narrowed and the lowest valence band, on the other hand, is lowered.

Tin dioxide:

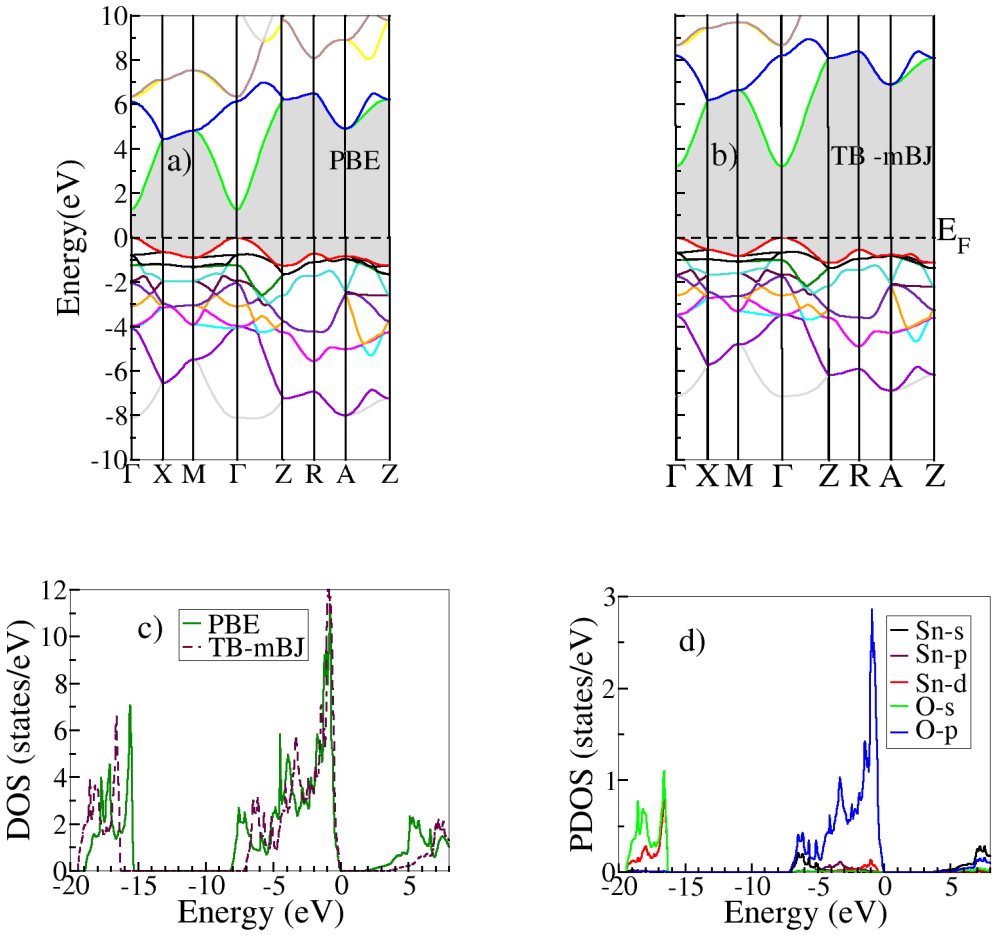

Figure 8.5: a) PBE and b) TB-mBJ band structure along with the c) total DOS with PBE and TB-mBJ and d) PDOS with TB-mBJ for SnO_2.

SnO_2 exists in rutile structure. The lattice parameters are a=4.7374 Å, c=3.1864 Å, and internal parameter u=0.305. The band structure shown in Fig. 8.5 yields a direct band gap of 1.25 eV for PBE and 3.20 eV for TB-mBJ. The valence bands in the range of 0 to -7 eV are composed of O-2p, Sn-4s,4p orbitals as evident from the PDOS presented in the same figure. There is also hybridization between $Sn-d$ and $O-s$ orbitals for the lowest valence bands between -16 to -19 eV. These Sn-4d are at lower binding energy in comparison with reported experimental value of 21.1 - 21.4 eV [50]. Unlike the other oxides, a distinct p-d hybridization is not observed in the PDOS.

In summary, the comparison between the total DOS shows that the valence band dispersion is reduced in the TB-mBJ scheme compared to the PBE band structure. It suggests that the TB-mBJ scheme tends to localize the valence bands compared to their PBE counterparts. This feature is found to be common for all the oxides studied and is more pronounced for widely dispersed bands than localized states such as O-2s.

8.4.2 p-type ternary oxides

We now present the TB-mBJ electronic structure of p-type ternary oxides: the delafossite $CuXO_2$ (X=Al,Ga,In) family and ZnX_2O_4 (X=Co,Rh,Ir) in the spinel structure. The delafossite crystal structure (space group $R\bar{3}m$, #166) is composed of O-Cu-O dumbbell layers in a hexagonal plane separated by a XO_6 edge-sharing octahedral layer (see Fig. 8.6). The spinel (space group $Fd\bar{3}m$, #227) lattice is based on face centered cubic packing of oxygen atoms (32 e sites) which are tetrahedrally coordinated with Zn ions (8 a sites) and octahedrally coordinated with the X cations (16 d sites) as shown earlier in Fig. 7.1. The experimental lattice constants are listed in Table-8.1.

Table 8.1: The experimental lattice constants and the internal parameter 'u', for delafossite (Ref. [133]) and spinel (Ref. [9]) structure.

Delafossite	$CuAlO_2$	$CuGaO_2$	$CuInO_2$
a (Å)	2.858	2.963	3.292
c (Å)	16.958	17.100	17.388
u	0.1099	0.1073	0.1056
Spinel	$ZnCo_2O_4$	$ZnRh_2O_4$	$ZnIr_2O_4$
a (Å)	8.104	8.489	8.507
u	0.263	0.263	0.263

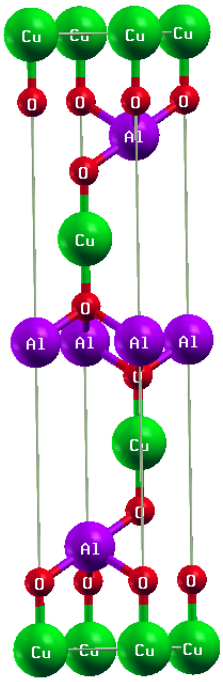

Figure 8.6: $CuAlO_2$ delafossite structure: O-Cu-O dumbbell layers in a hexagonal plane separated by a XO_6 edge-sharing octahedral layer. The image is generated using XCrySDen [141].

Table 8.2: The indirect (E_{ind}) and direct (E_{dir}) band gap at L of the delafossite structure calculated with PBE, TB-mBJ along with reported G_0W_0 (Ref. [134]) and experimental band gap (all in eV).

Oxide	PBE		TB-mBJ		G_0W_0		Expt.	
	E_{ind}	E_{dir}	E_{ind}	E_{dir}	E_{ind}	E_{dir}	E_{ind}	E_{dir}
$CuAlO_2$	1.92	2.57	2.21	3.28	4.96	5.05	3.00	3.4[a]
$CuGaO_2$	0.92	2.40	1.35	3.14	4.03	4.83	–	3.6[b]
$CuInO_2$	0.42	2.96	0.82	3.42	3.53	5.55	1.44	3.9[c]

[a] Ref. [3] [b] Ref. [4] [c] Ref. [5]

Delafossite $CuXO_2$ (X=Al,Ga,In) family

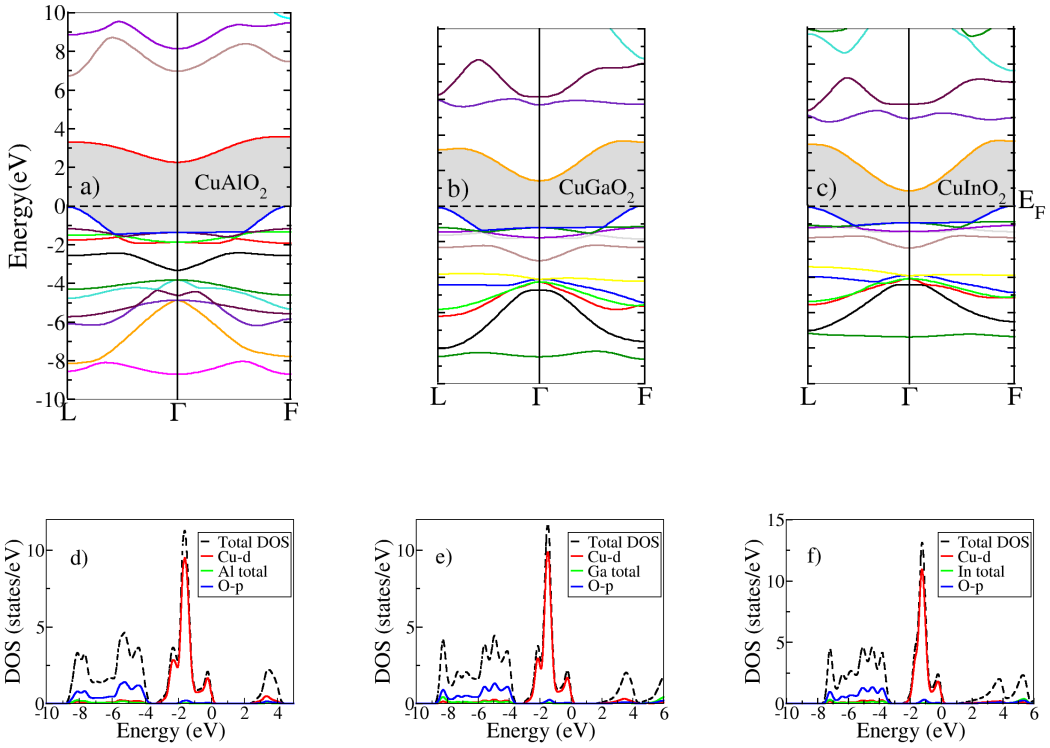

Figure 8.7: a), b), c)- TB-mBJ band structure and d), e), f) - the DOS plot for delafossite $CuXO_2$ (X=Al,Ga,In).

The TB-mBJ calculated band structures and PDOS of the delafossite family are shown in Fig. 8.7. All three compounds have an indirect fundamental band gap with the CBM is at Γ and the VBM is near F along the Γ-F direction. As seen in the PDOS, the well-isolated peak in the region 2 to 4 eV is the CBM which is composed of Cu-3*d* and O-2*p* orbitals. In the valence band the Cu-3*d* states are placed close to the Fermi level with a pronounced peak around -1.8 eV. These states are shallow compared to the XPS measurements of about -2.8 eV by Aston *et al.* [142]. The calculated indirect band gaps are 2.21, 1.35 and 0.82 eV for $CuAlO_2$, $CuGaO_2$ and $CuInO_2$ respectively. We also list in Table-8.2, the direct gap at the L point since the optically allowed transition is at L while the transition at the Γ point is optically forbidden for symmetry reasons [133, 134]. The calculated direct band gaps are 3.28, 3.14 and 3.42 eV, which are underestimated compared to the experimental values of 3.4, 3.6 and 3.9 eV by $\sim$ 3-12 % for $CuAlO_2$, $CuGaO_2$ and $CuInO_2$ respectively. The trend in the direct band gap, which slightly decreases from $CuAlO_2$ to $CuGaO_2$ and increases afterward for $CuInO_2$, is in qualitative agreement with previous PBE and G_0W_0 @ COHSEX results. It should be noted that the surprising overestimation of the G_0W_0 gap is attributed to polaronic effects and it has been shown that the direct gap is well reproduced by many-body approaches only if the polaronic effects are taken into account [135]. Also, $CuAlO_2$ features strong excitonic effects, with the exciton binding energy of 0.47 eV [136]. The TB-mBJ scheme can not account for either polaronic or excitonic effects observed in these systems.

ZnX_2O_4 (X=Co,Rh,Ir) spinels

Other interesting systems are ZnX_2O_4 (X=Co,Rh,Ir) spinels which are reported to be p-type TCOs. The origin of the band gap in these spinels is attributed to the ligand field splitting of X-*d* orbitals into fully occupied t_{2g}^6 and empty e_g^0 levels due to the octahedral surrounding of six oxygen anions forming a low spin state configuration. A recent theoretical study by Scanlon *et. al.* [137] has shown the underestimation of the band gap by PBE and a severe overestimation of the $t_{2g}^6 - e_g^0$ splitting with the HSE calculation compared to reported experimental values. Moreover, the observed decreasing trend in the band gap while moving from Co to Rh to Ir is in contrast with the only experimental study of Dekkers *et al.* [9] which reports the opposite. The TB-mBJ calculated band structures and PDOS for these spinels are shown in Fig. 8.8. All three spinels have an indirect band gap with the VBM occurring at the X point and the CBM located near the X point along the X-Γ direction. The well-isolated peaks of occupied t_{2g}^6 and empty e_g^0 levels forms the VBM and CBM respectively as is evident from the PDOS. The

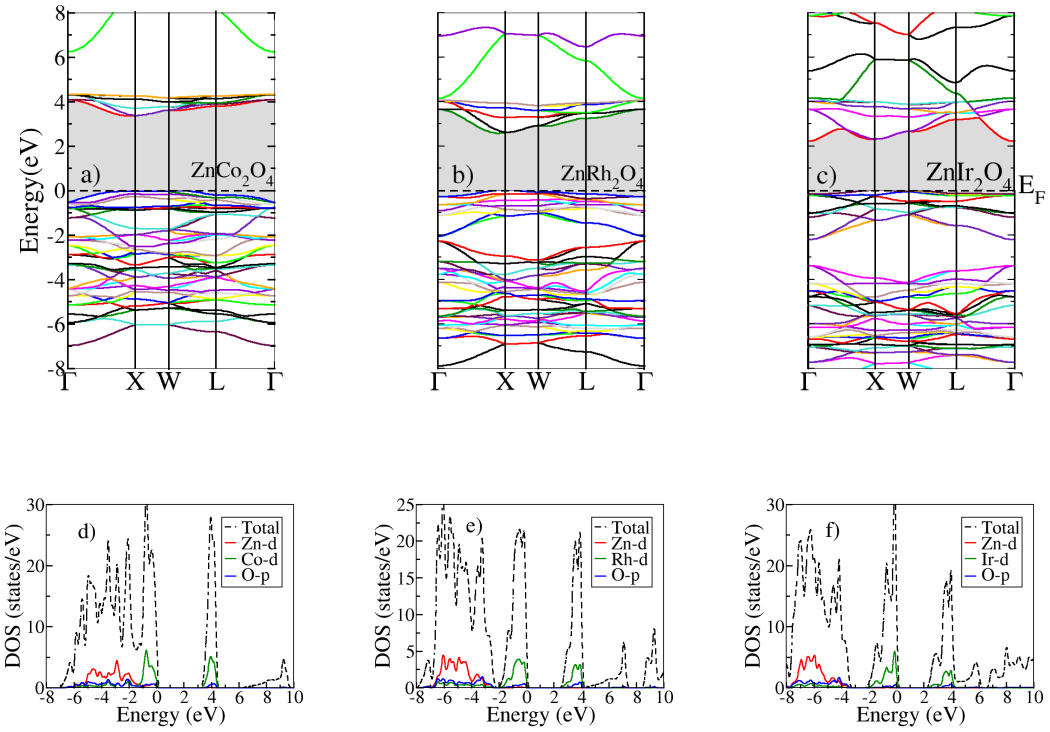

Figure 8.8: a), b), c)- TB-mBJ band structure and d), e), f) - the DOS plot for ZnX_2O_4 (X=Co,Rh,Ir) spinel.

Zn-3d states are spread in the lower part of the valence band with lowest peak around -4.8, -6.6 and -7.2 eV which are shallow compared to the experimental report of ∼-8.8, ∼-9.2 and ∼-9.5 eV for $ZnCo_2O_4$, $ZnRh_2O_4$ and $ZnIr_2O_4$ respectively. We also observe a decreasing trend in the indirect gap while moving from Co to Rh to Ir with both PBE and TB-mBJ in accordance with the HSE result. The calculated indirect band gaps are 3.36, 2.53 and 2.30 eV for $ZnCo_2O_4$, $ZnRh_2O_4$ and $ZnIr_2O_4$ respectively (See Table-8.3). Other experimental studies which report the band gap of 2.63 eV and 2.1 eV for $ZnCo_2O_4$ [8] and $ZnRh_2O_4$ [7] are at variance with Dekkers *et al.* and also show a decrease in the band gap when Co is replaced by the heavier Rh cation. We find TB-mBJ yields a better estimate of the band gap than HSE for $ZnCo_2O_4$ and $ZnRh_2O_4$ in comparison with these experiments, although the $t_{2g}^6 - e_g^0$ splitting is overestimated. Thus the TB-mBJ calculations sup-

port the claim made by Scanlon *et. al.* for reinvestigation of the band gaps for these spinels.

Table 8.3: The indirect band gap calculated with PBE, TB-mBJ along with reported HSE (Ref. [137]) and experimental band gap for the spinel structure (all in eV).

Oxide	PBE	TB-mBJ	HSE	Expt.
$ZnCo_2O_4$	0.71	3.36	3.86	2.26[a], 2.63[b]
$ZnRh_2O_4$	0.89	2.53	2.87	2.74[a], 2.1[c]
$ZnIr_2O_4$	0.28	2.30	2.45	2.97[a]

[a] Ref. [9] [b] Ref. [8] [c] Ref. [7]

8.5 Discussion and Conclusions

Table 8.4: The PBE, TB-mBJ, G_0W_0 and experimental band gap for four different oxides (all in eV).

Oxide	E_g^{PBE}	E_g^{TB-mBJ}	$E_g^{Expt.}$	$E_g^{G_0W_0}$
In_2O_3	1.18	2.90	3.10[a]	3.10[c]
ZnO	0.78	2.68	3.44	2.49[d]
CdO	-0.28	1.82	1.2 - 2[b]	1.07[e]
SnO_2	1.25	3.20	3.60	3.85[f]; 3.65[g]

[a] Ref. [52] [b] Ref. [47] [c] Ref. [138] [d] Ref. [86] [e] Ref. [132] [f] Ref. [139] [f] Ref. [140]

We first discuss the results obtained for the binary oxides, namely In_2O_3, ZnO, CdO and SnO_2. The calculated band gaps along with the experimental and GW results are tabulated in Table-8.4. The strong underestimation of the Kohn-Sham gaps with PBE can be attributed to the strong *p-d* hybridization between the anion and cation. The TB-mBJ band gaps, as listed in the second column, show a good improvement in the gaps compared to PBE. These gaps also are in agreement with the experimental values with small underestimation except ZnO. For ZnO the band gap is underestimated as large as 22%. It should be noted that the G_0W_0 result for ZnO is also underestimated. Since LDA or GGA is typically used as a starting point to calculate the G_0W_0 gap, the *p-d* hybridization in the LDA/GGA band structure influences the result and correspondingly the G_0W_0 gap of ZnO is

underestimated. For other systems which show a weaker hybridization in the LDA/GGA band structure, the agreement between the G_0W_0 and the experimental gap is remarkably good.

Table 8.5: The electron effective mass (in units of the electron mass, m_e) for n-type binary oxides.

Oxide	m_e^{PBE}	m_e^{TB-mBJ}	$m_e^{Expt.}$
In_2O_3	0.22	0.54	0.30
ZnO	$m_\parallel = 0.23$	$m_\parallel = 0.51$	0.32
	$m_\perp = 0.14$	$m_\perp = 0.33$	
CdO	0.16	0.35	0.21
SnO_2	$m_\parallel = 0.29$	$m_\parallel = 0.42$	0.29
	$m_\perp = 0.17$	$m_\perp = 0.23$	

The TB-mBJ DOS shows that the dispersion of the upper valence band is narrowed and the lower valence bands are moved to higher binding energies by $\sim$ 0.8-1.0 eV compared to PBE counterparts in the case of ZnO and SnO_2. For In_2O_3 and CdO, such a change is less significant. This might explain a better agreement between the TB-mBJ and experimental band gap observed in the case of In_2O_3 and CdO. Another important physical property of n-type TCO is the electron effective mass. The TB-mBJ effective masses are listed in Table-8.5. The observed trend shows that the effective masses are systematically overestimated (almost by a factor of 2) compared to PBE values and also experiment. This agrees with similar observations recently made for III-V semiconductors by Kim *et. al.* [124]. This overestimation can be attributed to the general tendency of the TB-mBJ scheme to reduce the dispersion of the bands as discussed earlier.

For the p-type conducting TCOs studied namely delafossite $CuXO_2$ (X=Al,Ga,In) and spinel ZnX_2O_4 (X=Co,Rh,Ir), we find qualitative agreement between TB-mBJ and G_0W_0 or HSE results with respect to the trends in the band gap. Quantitatively the TB-mBJ gaps are different from those reported with G_0W_0 or HSE. Moreover, we observe that the Cu-3d and Zn-3d states in these systems are also shallow compared to their experimental counterparts as was also the case for ZnO and CdO. In spite of the complicated electronic structure of these systems the TB-mBJ scheme gives a better estimation of the band gap over PBE and the trends observed within G_0W_0/HSE are also reproduced. Thus we find that the TB-mBJ offers a reliable, simple way and viable alternative to the computationally expensive techniques for the calculation of the band gaps of TCOs with desired accuracy.

Chapter 9

Formation energy of native defects in $ZnAl_2O_4$ spinel

9.1 Introduction

Al-doped ZnO thin films are highly attractive TCOs due to their stability and low cost compared to ITO films. In a mixture of ZnO and Al_2O_3, the $ZnAl_2O_4$ spinel structure can appear if the Al concentration becomes too large [101, 102]. This spinel structure is in itself of technological interest due to its wide band gap. We have shown in chapter 7 that using the quasiparticle calculations the expected band gap of $ZnAl_2O_4$ spinel is about 6.55 eV almost twice of the band gap of ZnO. As it is observed for semiconductors that defects and impurities play an important role in determining their electronic structure and physical properties, we have undertaken a study of all possible point defects in $ZnAl_2O_4$[1]. To the best of our knowledge such a study is not available. Pandey *et al.* have done a study using two body inter-atomic potentials on a limited set of defects [143]. With the recent advances in first principles calculations based on DFT, we are able to do more accurate defect physics. Here we present results with the GGA, GGA+U and hybrid functionals (HSE06 as proposed by Heyd, Scuseria and Ernzerhof [35, 36]). The formation energy calculations based on DFT using the LDA or GGA suffer from the well known band gap error which is explained in the following. The reported experimental band gap of $ZnAl_2O_4$ spinel is 3.8-3.9 eV [101]. Interestingly the tight-binding calculations gives a gap of 4.11 eV [106] and the LDA yields 4.24 eV [144] - almost 8% overestimated compared to the

[1]The work presented in this chapter will be communicated as - H. Dixit, Nandan Tandon, S. Cottenier, R. Saniz, D. Lamoen and B. Partoens: "*Formation energy of point defects in $ZnAl_2O_4$: first-principles study with hybrid functional*", in preparation.

experimental value. The band gap, however, should be underestimated due to the strong *p-d* hybridization observed in the electronic structure of $ZnAl_2O_4$ spinel with LDA/GGA. Considering this band gap anomaly and the fact that the band gaps in [101] were derived from reflectance measurements of powder samples, the authors Sampath et al. [106] have suggested that the measured experimental value is probably incorrect and a correction due to the particle-size dependence of light scattering may be necessary. Recently, using the state of the art GW approximation to calculate the quasiparticle band gap in solids, we have shown that the expected value of the band gap is about 6.55 eV [130]. A reinvestigation of the experimental band gap of $ZnAl_2O_4$ spinel is thus warranted. The calculated DFT-GGA band gap of 3.83 eV is underestimated by $\sim$2.7 eV compared to the calculated value of the GW band gap. This underestimation may lead to uncertainties in the calculated position of the defect induced states with DFT-GGA in the band gap. As a consequence the defect formation energies will be affected. Thus we have also used HSE functionals which correct the band gap error which is demonstrated to be reliable method to calculate transition levels and formation energies of defects [37].

Thus the purpose of this study is twofold: firstly, we want to understand the shallow or deep character of native defects in $ZnAl_2O_4$, and secondly, we want to compare different methodologies for defect calculations. We present our results in the following way in this chapter. First a discussion of the electronic structure of defect free $ZnAl_2O_4$ is presented. This is followed by our results on formation energies of various defects in a $ZnAl_2O_4$ supercell using GGA, GGA+U and HSE. To reflect different experimental growth conditions theoretically, such as Zn-rich, O-rich etc., the chemical potential of the constituents is allowed to vary. This allows a comparison of formation energies of various defects under different growth conditions. Since charged defects are also possible, transition levels for different charged defects are also reported. Systematically formation energies under two types of growth conditions are discussed. These can be experimentally observed and hence are very important.

9.2 Method and Computational Details

Theoretical investigations reported here are based on DFT within the GGA and GGA+U approach as implemented in the Vienna ab initio simulation package (VASP) [145]. The Hubbard U parameter which adds an on-site Coulomb potential is used only for the Zn d orbital, to overcome practically

the known limitation of LDA to underestimate the band gap due to the erroneous prediction of $p-d$ hybridization in such semiconductors [48]. The choice of $U_{Zn} = 4.7$ eV follows from earlier work on ZnO [146]. Electron-ion interactions are treated using the projector augmented wave (PAW) potentials [147, 41]. For the description of the spinel structure Zn ($4s^2 3d^{10}$), Al ($3s^2 3p^1$) and O ($2s^2 2p^4$) are considered as valence electrons. A regular $ZnAl_2O_4$ unit cell consists of 14 atoms *viz.* 2 Zn, 4 Al and 8 O atoms. For total energy calculations of defects in the spinel structure, a $2\times2\times2$ supercell consisting of 112 atoms is considered as the starting point. Atoms are removed (added) to mimic vacancy (substitution) sites. The whole supercell is then allowed to relax to its ground state. We consider the system to be in its ground state when the forces acting on the atoms are below 0.01 eV/Å and simultaneously achieving total energy convergence up to 10^{-4} eV. This convergence is obtained with a Monkhorst-Pack special k-point grid of $2\times2\times2$. We have used 37.5% mixing of Hartree-Fock exchange in the HSE functional. This mixing parameter correctly reproduces the experimental value of the band gap in ZnO [37] and also the calculated band gap of 6.63 eV for $ZnAl_2O_4$ is in close agreement with the GW result of 6.55 eV.

The defect formation energy ($E_f[D^q]$) for a defect (D) in a charge state q is defined as:

$$E_f[D^q] = E_{tot}[D^q] - E_{tot}[bulk] + \sum_i n_i\mu_i + q[E_F + E_v + \Delta V] \qquad (9.1)$$

where $E_{tot}[D^q]$ is the total energy of the supercell containing the defect, $E_{tot}[bulk]$ is the total energy of the supercell without defect, n_i is the number of atoms of the type i ($n_i < 0$ if atom is added and $n_i > 0$ if atom is removed) and μ_i is the corresponding chemical potential. E_F is the Fermi energy with respect to the E_v which is chosen to be the top of the valence band of the primitive unit cell. ΔV is the difference in the reference potential of the supercell without defect and the supercell with defect.

Eq. 9.1 indicates that the defect formation energy depends sensitively on the chemical potential of both atomic species and electrons (often referred to as the Fermi energy - E_f). This is because in forming the defect, particles are exchanged between the host material and the chemical reservoirs. For example, to form the antisite defect Al_{Zn} in $ZnAl_2O_4$ one has to take an Al atom from the Al chemical reservoir, put it into the host, and remove a Zn atom from the host and put it into the Zn chemical reservoir. Therefore, the formation energy of Al_{Zn} decreases if the chemical potential of Al increases. Furthermore, to form a positively charged defect ($q > 0$), one has to put the electrons removed from the defect into an electron reservoir with its characteristic energy E_F. Thus, the positively charged defect will have a

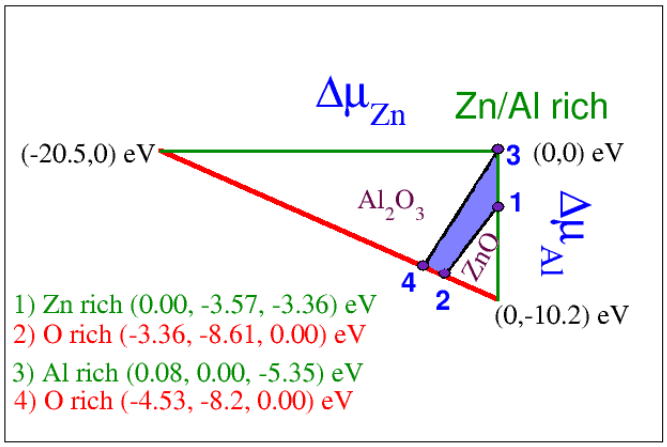

Figure 9.1: Schematic illustration for accessible chemical potential range.

higher formation energy in an n-type sample in which the Fermi energy is close to the CBM. Similarly, negatively charged defects ($q < 0$) will have a higher energy in p-type material in which the Fermi energy is close to the VBM. Therefore, by adjusting the chemical potential of the dopant or the Fermi energy, one can control the dopant solubility.

The chemical potential depends on the experimental growth conditions which can vary from X-poor to X-rich, where X could be either of Zn, Al or O. We first illustrate the possible variation of the chemical potential for a simple binary system and then will extend it to the ternary system $ZnAl_2O_4$. This method follows the formalism proposed by Wei [148, 149]. Consider ZnO, the formation energy is given by

$$\begin{aligned}\Delta H_f^{ZnO} &= E[ZnO] - E[Zn_{bulk}]/atom - \frac{1}{2}E[O_2(molecule)] \\ &= E[ZnO] - \mu_{Zn}^{Znbulk} - \mu_O^{O_2molecule} \\ &= \Delta\mu_{Zn} + \Delta\mu_O \\ &= -3.36 \text{ eV}\end{aligned}$$

where $\Delta\mu_{Zn} = \mu_{Zn}^{ZnO} - \mu_{Zn}^{Znbulk}$ and $\Delta\mu_O = \mu_O^{ZnO} - \mu_O^{O_2molecule}$ (here $\mu_{Zn/O}^{ZnO}$

corresponds to the energy of a Zn/O atom in ZnO, μ_{Zn}^{Znbulk} corresponds to the energy of a Zn atom in bulk Zn and $\mu_{O}^{O_2 molecule}$ corresponds to the energy of a O atom in oxygen molecule) indicating the possible variation of Zn and O chemical potential when ZnO is formed. In order to avoid the elemental precipitation into the bulk Zn and oxygen gas respectively, $\Delta\mu_{Zn}$ & $\Delta\mu_{O} \leq 0$. The upper limit on the Zn chemical potential is set by the Zn - rich conditions: $\mu_{Zn}^{ZnO} = \mu_{Zn}^{Znbulk}$ and $\Delta\mu_{Zn} = 0$. The oxygen chemical potential corresponding to the Zn - rich conditions is then determined as $\Delta\mu_{O} = \Delta H_f^{ZnO} = -3.36$ eV. Similarly the O - rich conditions imply $\mu_{O}^{ZnO} = \mu_{O}^{O_2 molecule}$ and $\Delta\mu_{O} = 0$. The zinc chemical potential corresponding to the O - rich conditions is then $\Delta\mu_{Zn} = \Delta H_f^{ZnO} = -3.36$ eV.

For ternary systems, the chemical potentials of each constituent species can be varied to reflect specific equilibrium growth conditions, but are always globally constrained by the calculated formation enthalpy of the host in order to maintain its stability. Thus in the case of $ZnAl_2O_4$ spinel:

$$\Delta H_f^{ZnAl_2O_4} = \Delta\mu_{Zn} + 2 \times \Delta\mu_{Al} + 4 \times \Delta\mu_{O} = -20.58 \text{ eV} \tag{9.2}$$

It should be noted that $\Delta\mu_{Zn} = \mu_{Zn}^{ZnAl_2O_4} - \mu_{Zn}^{Znbulk}$ and $\Delta\mu_{Zn}$, $\Delta\mu_{Zn}$ are also defined in a similar way. In addition to the host condition (Eq. 9.2), to avoid the elemental precipitation (Zn/Al solid or oxygen gas) the upper limits are set as:

$$\Delta\mu_{Zn} \leq 0, \Delta\mu_{Al} \leq 0, \Delta\mu_{O} \leq 0 \tag{9.3}$$

The resulting accessible range of the chemical potentials, is illustrated in Fig. 9.1 in a two-dimensional (μ_{Zn}, μ_{Al}) plane. The vertices of the stability triangle are formed from the host condition (Eq. 9.2) giving the limits of Zn/Al rich, Zn poor and Al poor environments, respectively. The Zn rich condition ($\Delta\mu_{Zn} = 0$ & $\Delta\mu_{O} = 0$) leads to the maximum possible variation in Al chemical potential: $\Delta\mu_{Al} = \Delta H_f^{ZnAl_2O_4}/2 = -10.29$ eV. On the other hand, the Al rich condition ($\Delta\mu_{Al} = 0$ & $\Delta\mu_{O} = 0$) leads to $\Delta\mu_{Zn} = \Delta H_f^{ZnAl_2O_4} = -20.58$ eV. The line joining the Zn poor (-20.58, 0.00) and Al poor (0.00, -10.29) vertex refers to $\Delta\mu_{O} = 0$ and mimics the oxygen rich condition. Thus within this triangle the $ZnAl_2O_4$ structure can exist, but the binary structures might have a lower formation energy.

Therefore, the constraints are also imposed by the formation of competing binary oxides ZnO and Al_2O_3, which are

$$\Delta\mu_{Zn} + \Delta\mu_{O} \leq \Delta H_f^{ZnO} = -3.36 \text{ eV} \tag{9.4}$$

$$2 \times \Delta\mu_{Al} + 3 \times \Delta\mu_{O} \leq \Delta H_f^{Al_2O_3} = -16.05 \text{ eV} \tag{9.5}$$

These constraints limit the possible accessible range of chemical potentials ($\Delta\mu_{Zn}$, $\Delta\mu_{Al}$) for $ZnAl_2O_4$ and available stable region is shown in gray. The vertices of this stable region are labeled as [1,2,3,4] and are determined as follows. First vertex, [1], refers to Zn rich condition ($\Delta\mu_{Zn} = 0$ eV) and using Eq. 9.4 it leads to $\Delta\mu_O = -3.36$ eV and $\Delta\mu_{Al} = -3.57$ eV from the stability of the host (Eq. 9.2). The coordinates of the first vertex thus corresponds to: $(\Delta\mu_{Zn}, \Delta\mu_{Al}, \Delta\mu_O) \equiv (0.00, -3.57, -3.36)$ eV. Second vertex, [2], corresponds to the O rich condition ($\Delta\mu_O = 0$) resulting in $\Delta\mu_{Zn} = -3.36$ eV using Eq. 9.4 and $\Delta\mu_{Al} = -8.61$ eV from the stability of the host (Eq. 9.2). The coordinates of the second vertex are: $(\Delta\mu_{Zn}, \Delta\mu_{Al}, \Delta\mu_O) \equiv (-3.36, -8.61, 0.00)$ eV. Below the line joining vertex [1] with [2], Eq. 9.4 is not fulfilled and ZnO will form instead of $ZnAl_2O_4$.

Similarly, vertex [3]$(0.08, 0.00, -5.35)$ and [4]$(-4.54, -8.02, 0.00)$ refers to the Al rich and O rich condition respectively and are determined from Eq. 9.5 and from the stability of the host (Eq. 9.2). Above this line, Al_2O_3 will be formed. For the formation energy plots, we only consider Zn rich (vertex-[1]) and O rich (vertex- [2]) conditions because the shaded region is rather narrow indicating the limited accessible range of the chemical potentials.

It should be noted that the value of the chemical potential also depends on the exchange-correlation functional. The above mentioned values corresponds to the GGA functional. For the case of HSE06 functional we repeat the same procedure to obtain the stable region.

Evaluation of the formation energy for different charged defects allows to find the transition level between two different charged states ($\epsilon(q/q')$). It is the Fermi energy for which two transition levels have the same formation energy. These transition levels can be observed in experiment with deep-level transient spectroscopy (DLTS). For the final charge states we allow the system to relax to its ground state. Five charged states ranging from $-2, -1, 0, 1, 2$ are considered and only the transition points for the ones with the lowest formation energy are mentioned in the next section. Additionally we also consider +3 charged states for Al-vacancy and Al at Zn (antisite) defects owing to the three valence electrons of Al.

9.3 Result and discussion

9.3.1 Electronic band structure with HSE06

The electronic structure and density of states (DOS) for $ZnAl_2O_4$ spinel, calculated using HSE06, is shown in Fig 9.2. $ZnAl_2O_4$ is a direct band gap material with both the VBM and the CBM at Γ. The calculated band

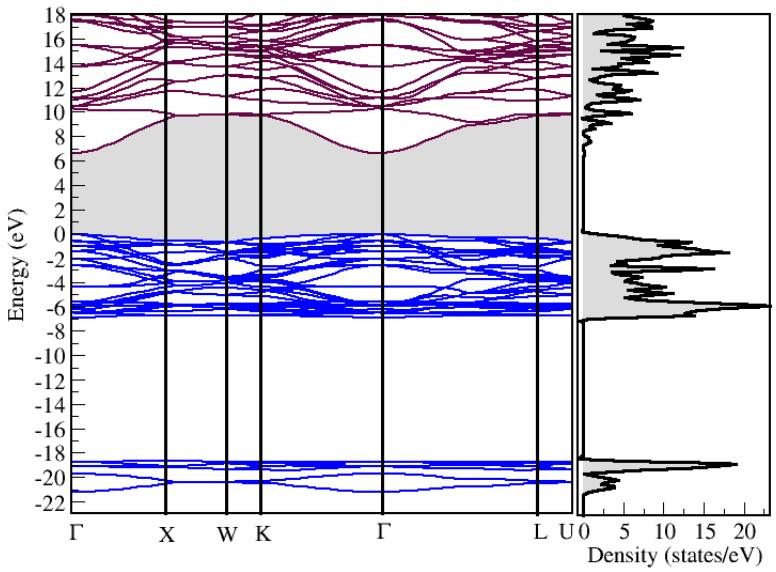

Figure 9.2: Electronic band structure and density of states calculated using HSE06.

gap with HSE06 is 6.63 eV which shows a significant opening of the gap compared to the GGA value of 3.83 eV and which is in good agreement with the reported G_0W_0 gap of 6.55 eV.

9.3.2 Formation energy with GGA and GGA+U

We have studied five point defects in the $ZnAl_2O_4$ lattice: the Al, Zn and O vacancy along with the antisite defects - Zn replacing Al (Zn_{Al}) and Al replacing Zn (Al_{Zn}). Formation energies of these defects are calculated using the methodology described in the previous section. The formation energy of each defect as a function of the Fermi level, calculated with GGA and GGA+U, is shown in Fig. 9.3. First, we discuss the formation energies calculated using the GGA. It is expected that the removal of either Zn or Al atom will result in a net electron deficiency and the generation of unoccupied acceptor levels. Such empty defect bands, if situated below the VBM are called shallow acceptors. This results in the production of positive holes (p-type carriers) in the valence band giving rise to p-type conductivity. We find that both the Zn and Al vacancy are acceptors and favor the -2 and -3 charge state respectively. Unfortunately, under Zn rich (oxygen poor) conditions,

the formation energy of both defects is high, tending toward 8 and 11 eV for the Zn and Al vacancy, as the Fermi level approaches the VBM. A change to oxygen rich (Zn poor) conditions reduces the cation chemical potentials, resulting in relatively lower formation energies (about 4 and 7 eV) of the Zn and Al vacancy. However the formation energies are still large suggesting that under such conditions, both can not be readily formed. The oxygen vacancy, on the other hand, exhibits an interesting behavior as a function of the Fermi energy. Initially it favors the +2 charge state, indicating donor like behavior. The +2/0 transition occurs at about 3.1 eV above the VBM (under Zn - rich condition) and it continues to prefer the neutral state till $\sim$ 4.3 eV where a 0/-1 transition occurs and finally becomes an acceptor and prefers the -2 charge state. This suggests that the oxygen vacancy acts as an amphoteric impurity, exhibiting both donor and acceptor like behavior depending on the Fermi energy. A similar amphoteric behavior is also shown by the Al_{Zn} antisite defect. However it is an unexpected result since removal of an oxygen is expected to result in two extra electrons in excess in the system. Also since the Al atom contains an extra electron in the valence compared to Zn, the Al_{Zn} antisite defect will also lead to an extra electron added to the system. Thus we expect both the oxygen vacancy and the Al_{Zn} antisite defect to prefer to be a donor state.

The GGA+U calculations also show similar trends for these native defects. It should be noted that the GGA+U (U = 4.7 eV) applied to Zn-d states results in a partial correction to the band gap (4.17 eV for GGA+U versus 3.83 eV for GGA). The surprising amphoteric nature of the oxygen vacancy and Al_{Zn} antisite defect is also observed in the GGA+U calculations and requires further analysis. We believe that it is an artifact due to the strong underestimation of both the GGA and GGA+U band gap compared to the G_0W_0 value of 6.55 eV. Thus in order to confirm it, we have calculated the formation energies using the HSE06 hybrid functional which yield a band gap of 6.63 eV in close agreement with the G_0W_0 result. These results are presented in the following section. However before discussing the hybrid results I would like to mention an interesting observation. In Fig. 9.3, if we set the CBM at the band gap calculated with the GGA and GGA+U schemes, i.e. E_F is varied between 0 and 3.8/4.17 eV, we find that the oxygen vacancy is a deep donor and the Al_{Zn} antisite defect is a shallow donor.

9.3.3 Formation energy with HSE06

In the GGA and GGA+U calculations, the whole supercell is allowed to relax after the introduction of the defect such that the forces on each atomic

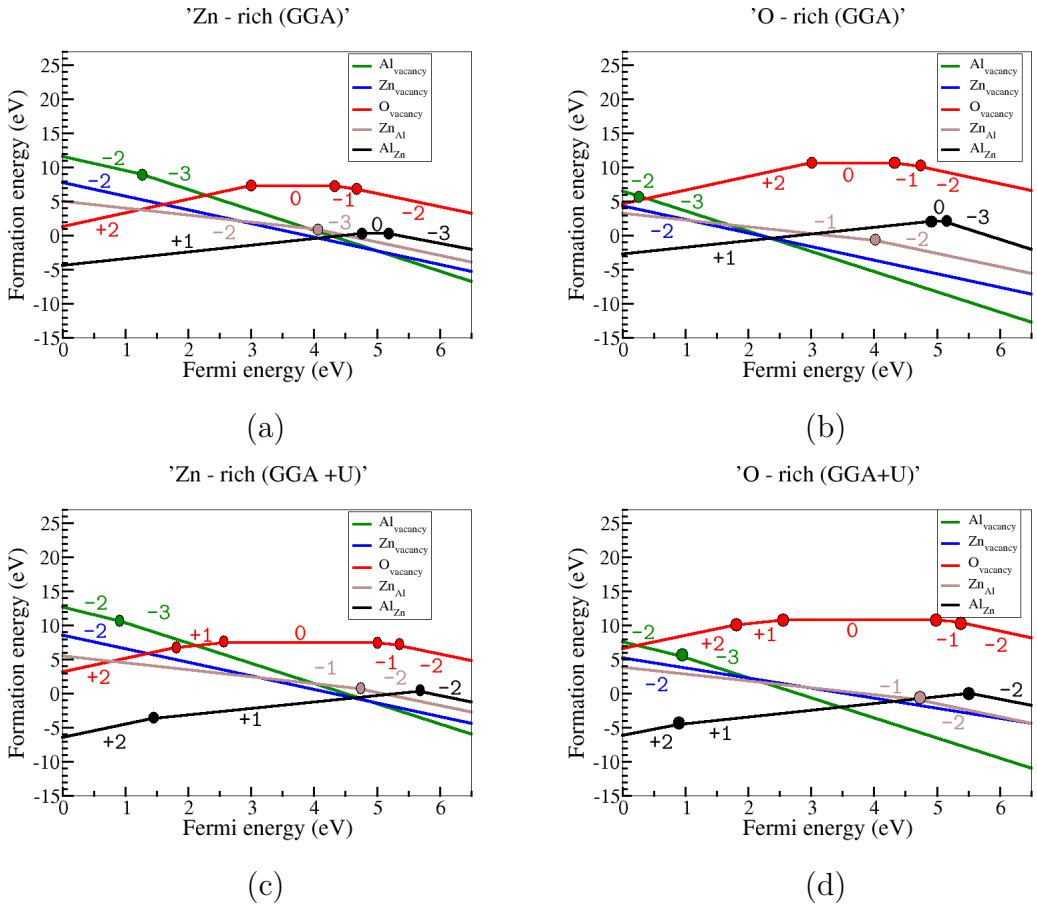

Figure 9.3: Calculated intrinsic defect formation energies as a function of Fermi energy under (a), (c) Zn-rich and (b), (d) O-rich condition with the GGA and GGA+U functional.

site are below 0.01 eV/Å. We have noticed that such a relaxation with the HSE06 functional is too time consuming. Hence we adopt the following scheme. First, only the unit cell is relaxed with HSE06. The supercell of 112 atoms is constructed with this relaxed unit cell. For a supercell with defects, the HSE06 optimized lattice constant and relaxed GGA coordinates of atoms are used. The total force acting on the atoms in the supercell, constructed in this way, are of the order of a few tens of meV since the optimized GGA and HSE06 lattice constants differ marginally. Thus instead of allowing the complete relaxation of lattice parameters and atomic positions of the supercell, we adopt this scheme to calculate the total energies. The calculated formation energies as a function of Fermi energy using HSE06 are

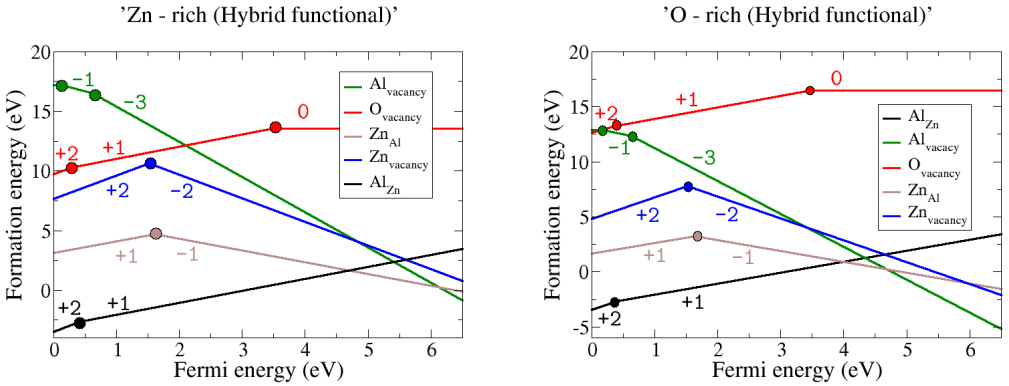

Figure 9.4: Calculated intrinsic defect formation energies as a function of Fermi energy under (a) Zn rich and (b) O rich condition with HSE06.

shown in Fig. 9.4. We find that both the Al and Zn vacancies are acceptors and prefer the -3 and -2 charged states respectively. The antisite defect Zn_{Al} is also an acceptor and favors the -1 charged state. The oxygen vacancy is found to be a really deep donor with the +1/0 transition occurring ∼3 eV below the CBM, ruling out the possibility of oxygen vacancies contributing electrons to the conduction band by thermal ionization. It should be noted that the formation energies of these four defects are high. Only the Al_{Zn} antisite defect has a low formation energy suggesting that it can be readily formed. It is a shallow donor and prefers the +1 charged state.

9.4 Conclusions

The calculated formation energies show that the Al and Zn vacancies along with the Zn_{Al} antisite defect are acceptors, however their formation energies are high. The oxygen vacancy is a deep donor and can not contribute to the conductivity. The donor Al_{Zn} antisite defect has the lowest formation under both Zn and O - rich conditions. These results suggest that the Al_{Zn} antisite defect can cause possible n-type conductivity in the $ZnAl_2O_4$ spinel. A comparative study of formation energies of native defects in $ZnAl_2O_4$ spinel with GGA, GGA+U and HSE06 clearly shows that the band gap error plays an important role and needs to be corrected. The hybrid functional, which corrects the band gap error, needs to be used for an accurate calculation of the formation energy of native defects.

Summary and outlook

First-principles electronic structure calculations play an important role in the understanding of the basic physics that governs the electronic and optical behavior of materials. They also offers a vital tool for efficient materials design. The key physical properties of TCO host materials are the band gap for optical transparency and the effective masses which determine the mobility of the charge carriers. The application of electronic structure methods, capable of calculating these quantities accurately, is thus helpful in designing better performing or new TCO materials. The electronic structure of these metal-oxide semiconductors has therefore been a subject of enduring interest. In this thesis we provide an accurate description of the electronic band structure of TCO materials using state of the art Density Functional Theory (DFT) and the GW approximation to the Many-body theory (MBT).

DFT is the most successful first-principles approach for the quantum mechanical description of the ground state properties of matter and after a general introduction in chapter 2, we present the band structure of the basic binary TCO compounds (In_2O_3, ZnO, CdO and SnO_2) in chapter 3 calculated within DFT. It is observed that although the structural properties of TCOs are accurately described, the electronic properties - namely the band gap and band mass, on the other hand are underestimated compared to experiment. Nevertheless, the DFT electronic structure calculations are useful to understand the nature of the valence and conduction band in these system and are a good starting point for more advanced approaches (e.g. GW calculations). The band structure shows a strong p-d hybridization between the cation d and anion p orbitals, which is a characteristic feature of these binary oxides. Thus for a quantitative prediction of the key physical properties of TCOs we have used the GW approximation within the MBT. The GW method is introduced in chapter 4.

The results obtained with the non self-consistent or single shot GW (G_0W_0) approximation are presented in chapter 5,6 and 7. We have studied ZnO, SnO_2 and spinel ZnX_2O_4 (X=Al, Ga and In) using the G_0W_0 approximation. The case study of ZnO (chapter 5) shows the necessity for using a

modified pseudopotential for an accurate description of the self-energy operator in the G_0W_0 approximation. We also observed that the *p-d* hybridization in the DFT band structure also influences the calculated G_0W_0 band gap in ZnO. Thus the G_0W_0 band gap of zincblende and wurtzite ZnO is underestimated compared to the experiment. On the other hand for the rocksalt phase of ZnO the G_0W_0 band gap shows good agreement with the experimental counterpart.

Equipped with this knowledge (the necessity of a modified pseudopotential for an accurate description of the self-energy operator), we further studied other interesting systems namely SnO_2 and CdO. We have calculated the quasiparticle band structure and the results are presented in chapter 6. For both these systems a good agreement between G_0W_0 and the experimental results for band gap and band mass is observed. We have further studied the effects of uniaxial pressure on the SnO_2 band gap. The band gap increases with increasing pressure and the rate of change is significant. For CdO, we have used an interpolation scheme using the maximally localized Wannier functions to construct the complete quasiparticle band structure. This interpolation scheme reduces the computational effort considerably and G_0W_0 corrections over a coarse Monkhorst-Pack grid are sufficient to construct the full quasiparticle band structure.

The last system studied with the G_0W_0 approximation is the ZnX_2O_4 (X=Al, Ga and In) spinel structure and results are discussed in chapter 7. In the case of $ZnAl_2O_4$ spinel, DFT overestimates the band gap in comparison to the experiment, which is in contrast to the general trend of DFT to systematically underestimate band gaps. This band gap anomaly was also observed by other researchers and it has been claimed that the experimental value is probably incorrect and needs to be re-investigated. Thus in order to explain this band gap anomaly with DFT for the case of $ZnAl_2O_4$ spinel, we have used the G_0W_0 approximation. Indeed the G_0W_0 band gap is larger than the experimental value and the G_0W_0 calculation supports the claim that the experimental band gap is incorrect.

During this study, we have observed that the application of the G_0W_0 method is computationally very demanding. Moreover, special care needs to be taken in the pseudopotentials used for an adequate treatment of the self-energy. This makes the G_0W_0 method computationally inefficient when a large class of material systems needs to be studied. Thus we have tested the recently proposed Tran-Blaha modified version of the Becke-Johnson potential (TB-mBJ) for TCO materials. This method has proved to be a successful method for accurate band gaps of semiconductors and insulators, and computationally it is as economical as LDA or GGA. We find that although the band gaps are in good agreement with the G_0W_0 method, the band masses

on the other hand are systematically overestimated. However, this method is still useful for high-throughput materials design due to the reduced computational effort.

Additionally I have also calculated the formation energies of native defects in $ZnAl_2O_4$ spinel. A set of five native defects which include the Zn, Al and O vacancy along with the antisite Al_{Zn} and Zn_{Al} defects are studied in different charge states. The results are obtained using a supercell approach using GGA, GGA+U and hybrid functionals. The calculated formation energies indicate that the Al_{Zn} is the most stable defect indicating possible n-type conductivity in the $ZnAl_2O_4$ spinel. Moreover, a comparative study between the GGA, GGA+U and hybrid functionals indicates that an electronic structure method which determines the band gap accurately is also necessary for a correct description of the charge transition levels and formation energies of the defect states.

To conclude, this thesis presents the electronic structure of TCOs using DFT and state of the art G_0W_0 approximation. For a quantitative and accurate prediction of the key physical properties of TCOs the G_0W_0 approximation should be used. However, computationally it is very demanding and the problem is further complicated by the *p-d* hybridization observed in TCOs. In particular the G_0W_0 band gap is influenced by the *p-d* hybridization present in the DFT band structure, which is used as the starting point for the G_0W_0 calculation, as observed in the case of ZnO. For other systems studied namely SnO_2, CdO and spinel $ZnGa_2O_4$ the G_0W_0 band gap shows a good agreement with the experimental counterpart. Thus for systems where G_0W_0 significantly underestimates the (experimental) band gap, one may use either the self-consistent GW calculations, which are computationally far more demanding, or use an exchange-correlation potential which improves the DFT result.

An alternative approach for the prediction of the band gap, which is computationally economic compared to the expensive G_0W_0 calculation, is provided by the recently proposed TB-mBJ potential scheme. We have tested this scheme for TCOs with a complex electronic structure. The TB-mBJ results obtained are in agreement with the G_0W_0 results. Thus this scheme can be efficiently used for high-throughput materials design due to the reduced computational effort.

Future developments

This thesis is focused on the accurate description of the band gap of TCOs, using one particle Green's function in the appealing framework of G_0W_0

approximation. The band gaps calculated in this way can only be compared with the band gaps measured using photoemission spectroscopy. However it is also possible to consider complex electron-hole interactions using the two particle Green's function and solve the Bethe-Salpeter equation within MBT. Thus the optical absorption spectra, optical gap and the dielectric properties of TCOs can be calculated using the Bethe-Salpeter equation.

Samenvatting

First-principles elektronische structuurberekeningen spelen een belangrijke rol in het begrijpen en doorgronden van de fundamentele processen die aan de grondslag liggen van de elektronische en optische eigenschappen van materialen. Dit betekent dat ze ook een belangrijk instrument zijn bij het ontwerpen van nieuwe materialen. Twee belangrijke karakteristieke grootheden voor TCO materialen zijn de bandkloof en de effectieve massa. De eerste geeft informatie over de optische transparantie van het materiaal en de tweede over de mobiliteit van de ladingsdragers. In dit proefschrift geven we een accurate berekening van deze grootheden op basis van de elektronische bandenstructuur voor een aantal belangrijke TCO materialen in het kader van het Density Functional Theory (DFT) en het Many-Body Theory (MBT) formalisme.

DFT is de meest succesvolle methodologie voor een kwantummechanische beschrijving van de grondtoestandseigenschappen van de materie. Na een algemene inleiding tot DFT in hoofdstuk 2, wordt in hoofdstuk 3 de bandenstructuur van de belangrijkste binaire TCO materialen (In_2O_3, ZnO, CdO and SnO_2) gegeven. Volledig in lijn met DFT berekeningen op andere systemen, zien we dat de structurele eigenschappen in excellente overeenstemming zijn met de experimentele waarden, maar dat de berekende waarden voor bandkloof en effectieve massa het experimentele resultaat onderschatten. Niettemin geven deze berekeningen inzicht in de aard van de valentie- en conductieband en de sterke *p-d* hybridisatie tussen de kation *d*- en anion *p*-orbitalen, wat een typische eigenschap is van deze binaire oxides. De DFT berekeningen vormen bovendien een geschikt startpunt voor een meer gevorderde aanpak zoals de GW berekeningen in het kader van het MBT formalisme.

Een korte inleiding tot de GW methode wordt in hoofdstuk 4 gegeven. In hoofdstuk 5,6 en 7 geven we de resultaten bekomen met de niet-zelfconsistente of single-shot GW (G_0W_0) voor ZnO, SnO_2 en spinel ZnX_2O_4 (X=Al, Ga, In). Het voorbeeld van ZnO toont aan dat een aangepaste pseudopotentiaal voor het kation noodzakelijk is voor een accurate beschrijving van de

zelfenergie operator in de G_0W_0 benadering. Bovendien zien we dat de *p-d* hybridisatie een sterke invloed heeft op de G_0W_0 bandkloof.

In hoofdstuk 6 wordt de G_0W_0 bandenstructuur voor SnO_2 en CdO gegeven. Voor beide systemen vinden we een bandkloof en een effectieve massa in goede overeenstemming met het experiment. Verder werd ook de drukafhankelijkheid van de bandkloof in SnO_2 onderzocht: de bandkloof neemt toe bij toenemende uni-axiale druk. Voor CdO berekende we de volledige G_0W_0-bandenstructuur door gebruik te maken van een interpolatieschema dat gebaseerd is op maximaal gelokaliseerde Wannier functies, wat de computationele kost in sterke mate reduceert.

Tenslotte onderzochten we in hoofdstuk 7 ook spinel ZnX_2O_4 (X=Al, Ga, In) in het kader van de G_0W_0 benadering. In tegenstelling tot wat men verwacht overschat DFT de bandkloof van $ZnAl_2O_4$ wat werd bevestigd door de G_0W_0 berekeningen. Dit suggereert dat de experimentele waarde niet correct is.

Tijdens deze studie hebben we vastgesteld dat de toepassing van de G_0W_0 methode computationeel zeer zwaar is. Bovendien moet speciale aandacht besteed worden aan de pseudopotentialen voor een correcte beschrijving van de zelf-energie. Dit maakt de G_0W_0 methode erg inefficiënt indien een grote klasse van materialen moet bestudeerd worden. Daarom hebben we de recent door Tran en Blaha voorgestelde modificatie van de Becke-Johnson potentiaal (TB-mBJ) getest voor TCO materialen. Het succes van deze methode in de voorspelling van een accurate bandkloof is reeds aangetoond voor halfgeleiders en isolatoren, en is computationeel even economisch als LDA of GGA. We vonden dat de bandkloof voor TCO materialen goed overeenkwam met de G_0W_0 methode, maar dat de effectieve massas systematisch overschat worden. Toch is de TB-mBJ methode een erg nuttige methode voor het high-throughput ontwerpen van materialen omwille van de lage computationele kost.

Daarnaast hebben we ook de vormingsenergieën berekend van intrinsieke defecten in de $ZnAl_2O_4$ spinel structuur. Een set van vijf defecten in verschillende ladingstoestanden werd onderzocht: de Zn, Al en O vacatures, samen met de antisite defecten Al_{Zn} en Zn_{Al}. De resultaten werden bekomen met behulp van een supercel en de GGA, GGA+U en hybride functionalen. De berekende vormingsenergieën tonen dat Al_Zn het meest stabiele defect is wat n-type geleiding in $ZnAl_2O_4$ mogelijk maakt. Een vergelijking van de resultaten bekomen met GGA, GGA+U en hybride functionalen toont dat een elektronische structuur methode die de bandkloof accuraat voorspelt ook noodzakelijk is voor een correcte beschrijving van de ladingstransitieniveaus en vormingsenergieën van de defecttoestanden.

Deze thesis bestudeert de elektronische structuur van TCOs met stan-

daard DFT en de state-of-the-art G_0W_0 methode. Voor een kwantitatieve en accurate voorspelling van de belangrijke fysische eigenschappen van TCOs moet de G_0W_0 methode gebruikt worden. Echter, deze methode is computationeel erg zwaar en het probleem wordt bovendien gecompliceerd door de *p-d* hybridisatie in TCOs. In het bijzonder wordt de G_0W_0 bandkloof beïnvloed door de *p-d* hybridisatie die aanwezig is in het DFT resultaat, dat als startpunt gebruikt wordt voor de G_0W_0 berekening, zoals vastgesteld in het geval van ZnO. Voor de andere bestudeerde systemen, SnO_2, CdO en spinel $ZnGa_2O_4$, vertoont de G_0W_0 bandkloof goede overeenkomst met de experimentele resultaten. Dus voor systemen waarvoor de G_0W_0 methode de experimentele bandkloof onderschat, kan men zich ofwel toeleggen op zelfconsistente GW berekeningen, die echter computationeel nog veel zwaarder zijn, ofwel gebruik maken van een exchange-correlatiefunctionaal die het DFT resultaat verbetert.

Een alternatieve aanpak voor de voorspelling van de bandkloof, die computationeel veel minder zwaar is dan de G_0W_0 berekening, is de recent voorgestelde TB-mBJ potentiaal. We hebben deze aanpak getest voor TCO materialen en een goede overeenkomst met de G_0W_0 resultaten werd gevonden. Daarom kan dit schema dan ook gebruikt worden voor het efficiënte high-throughput ontwerpen van materialen tegen een gereduceerde computationele kost.

Toekomstige ontwikkelingen

Dit proefschrift handelt hoofdzakelijk over de accurate berekening van de bandenstructuur en in het bijzonder van de bandkloof door middel van de één-deeltjes Greense functie in de GW benadering. Deze "fundamentele" bandkloof kan experimenteel gemeten worden door middel van foto-emissie spectroscopie. Echter voor een nauwkeurige berekening van de optische bandkloof moet men de elektron-holte interactie in rekening brengen. Dit gebeurt door de twee-deeltjes Greense functie te gebruiken en de Bethe-Salpeter vergelijking op te lossen in het kader van het MBT formalisme. Hieruit kan men dan de optische spectra, optische bandkloof en de diëlektrische eigenschappen van de TCO materialen berekenen.

Appendices

Appendix A

Convergence studies of GW parameters

Calculating the standard one-shot GW band gap within ABINIT is a four step procedure as follows:

- Ground State calculation to obtain the self-consistent density.
- Perform a non self-consistent run to compute the Kohn-Sham eigenvalues and eigenfunctions on a regular grid of k-points
- Calculating the inverse dielectric matrix (ϵ^{-1}) which involves three numerical parameters: 1) nband - Bands used in the screening calculation 2) ecutwfn - Cut-off energy of the planewave set to represent the wavefunctions 3) ecuteps - Cut-off energy of the planewave set to represent the dielectric matrix
- Computation of the self-energy (Σ) matrix element at the given k-point in order to obtain the GW quasiparticle energies It also involves three numerical parameters which needs to be converged. 1) nband - Bands to be used in the Self-Energy calculation 2) ecutwfn - Planewaves to be used to represent the wavefunctions 3) ecutsigx - Dimension of the **G** sum in Σ_x

The following graphs show a systematic convergence study of the exchange (Σ_x) and the correlation (Σ_c) part of the self-energy along with the eigenvalue of the VBM and CBM at the Γ point w.r.to all the numerical parameters mentioned above for zb-ZnO with Zn^{20+} PP. The convergence criterion of 0.01 eV is used for the band eigenvalue and band gap. Note that we have carried out such a convergence study for all the pseudopotential and all the system studied in this thesis. Here it is only illustrated for the Zn^{20+} PP.

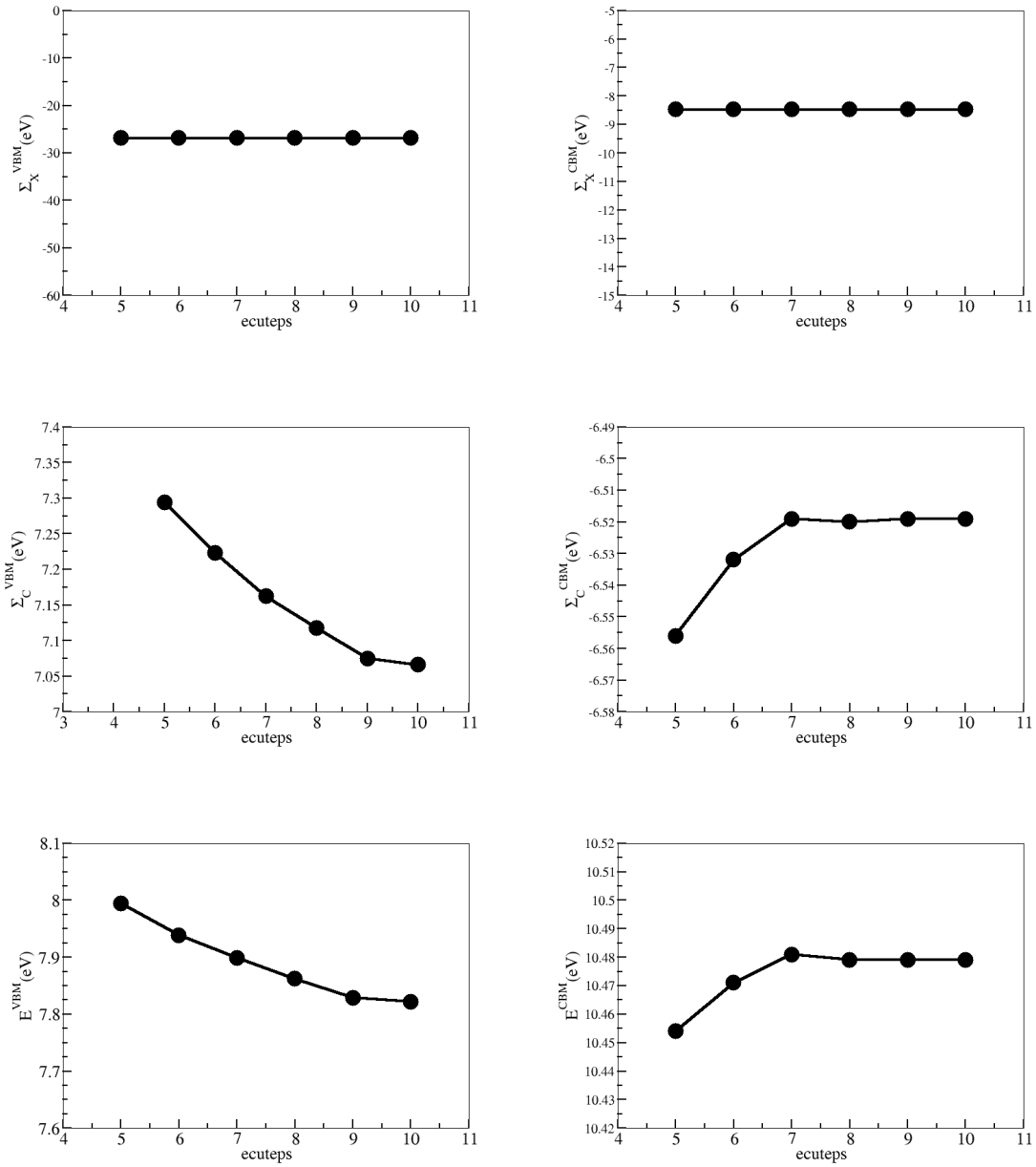

Figure 9.5: Convergence of the exchange (Σ_x) and correlation (Σ_x) part of self-energy along with the GW eigenvalue (E) of VBM (left panel) and CBM (right panel) w.r.to *ecuteps* used in the screening calculations.

Table 9.1: The convergence of VBM and CBM with respect to *ecuteps*, the converged values are highlighted with the bold face.

	VBM			CBM		
ecuteps	Σ_x	Σ_c	E	Σ_x	Σ_c	E
5	-26.855	7.294	7.995	-8.476	-6.556	10.454
6	-26.855	7.223	7.939	-8.476	-6.532	10.471
7	-26.855	7.162	7.899	-8.476	-6.519	10.481
8	-26.855	7.118	7.862	-8.476	-6.52	10.479
9	-26.855	7.075	7.829	-8.476	-6.519	10.479
10	**-26.855**	**7.066**	**7.822**	**-8.476**	**-6.519**	**10.479**

Table 9.2: The convergence of VBM and CBM with respect to *ecutwfn*, the converged values are highlighted with the bold face.

	VBM			CBM		
ecutwfn	Σ_x	Σ_c	E	Σ_x	Σ_c	E
20	-26.855	7.272	7.981	-8.476	-6.547	10.461
25	-26.855	7.237	7.95	-8.476	-6.541	10.465
30	-26.855	7.223	7.939	-8.476	-6.532	10.471
35	**-26.855**	**7.215**	**7.931**	**-8.476**	**-6.532**	**10.471**
40	-26.855	7.212	7.927	-8.476	-6.535	10.468

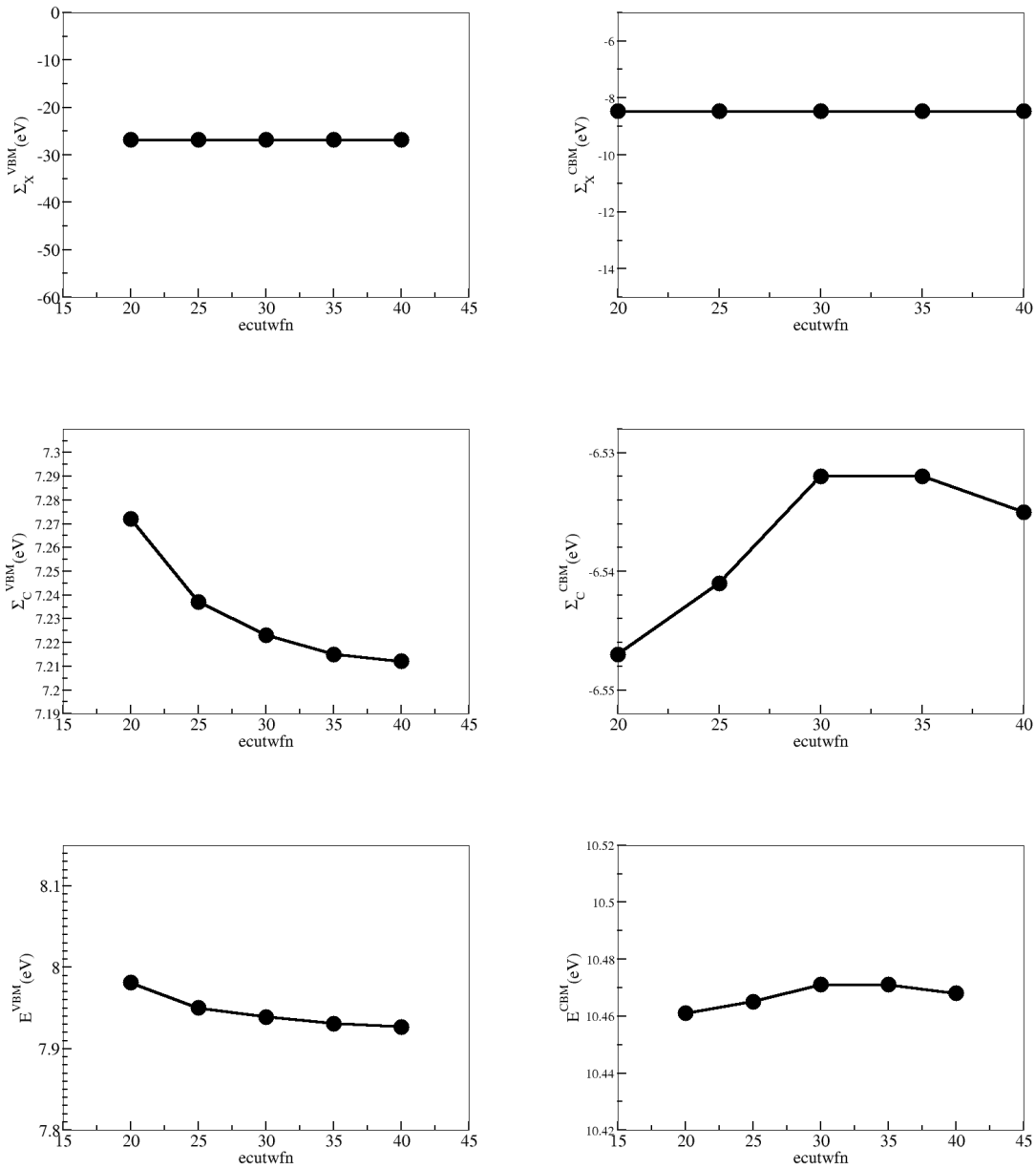

Figure 9.6: Convergence of the exchange (Σ_x) and correlation (Σ_x) part of self-energy along with the GW eigenvalue (E) of VBM (left panel) and CBM (right panel) w.r.to *ecutwfn* used in the screening calculations.

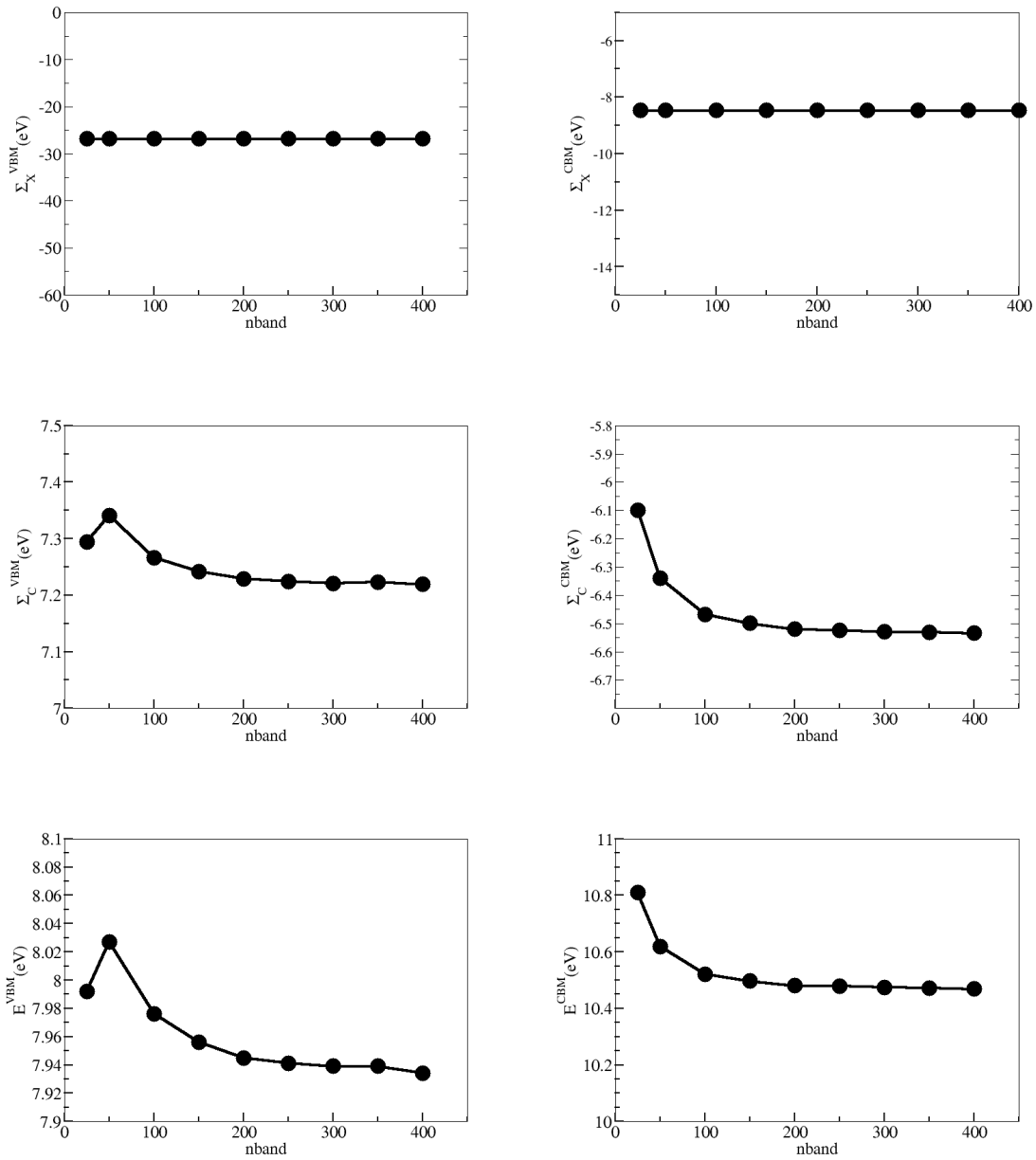

Figure 9.7: Convergence of the exchange (Σ_x) and correlation (Σ_x) part of self-energy along with the GW eigenvalue (E) of VBM (left panel) and CBM (right panel) w.r.to *nband* used in the screening calculations.

Table 9.3: The convergence of VBM and CBM with respect to *nband*, the converged values are highlighted with the bold face.

	VBM			CBM		
nband	Σ_x	Σ_c	E	Σ_x	Σ_c	E
25	-26.855	7.294	7.992	-8.476	-6.099	10.809
50	-26.855	7.341	8.027	-8.476	-6.34	10.619
100	-26.855	7.266	7.976	-8.476	-6.469	10.521
150	-26.855	7.242	7.956	-8.476	-6.5	10.496
200	-26.855	7.229	7.945	-8.476	-6.521	10.48
250	-26.855	7.224	7.941	-8.476	-6.524	10.478
300	**-26.855**	**7.221**	**7.939**	**-8.476**	**-6.53**	**10.474**
350	-26.855	7.223	7.939	-8.476	-6.532	10.471
400	-26.855	7.219	7.934	-8.476	-6.535	10.468

Table 9.4: The convergence of VBM and CBM with respect to *ecutsigx*, the converged values are highlighted with the bold face.

	VBM			CBM		
ecutsigx	Σ_x	Σ_c	E	sigx	Σ_c	E
20	-26.73	7.025	7.88	-8.366	-6.455	10.61
25	-26.798	7.022	7.826	-8.423	-6.443	10.575
30	-26.831	7.021	7.801	-8.449	-6.437	10.56
35	-26.848	7.02	7.787	-8.469	-6.432	10.549
40	**-26.855**	**7.02**	**7.782**	**-8.476**	**-6.43**	**10.545**
45	-26.859	7.02	7.778	-8.479	-6.429	10.543
50	-26.86	7.02	7.777	-8.48	-6.429	10.543
55	-26.861	7.02	7.777	-8.48	-6.429	10.543
60	-26.861	7.02	7.777	-8.48	-6.429	10.543
65	-26.862	7.02	7.777	-8.48	-6.429	10.543

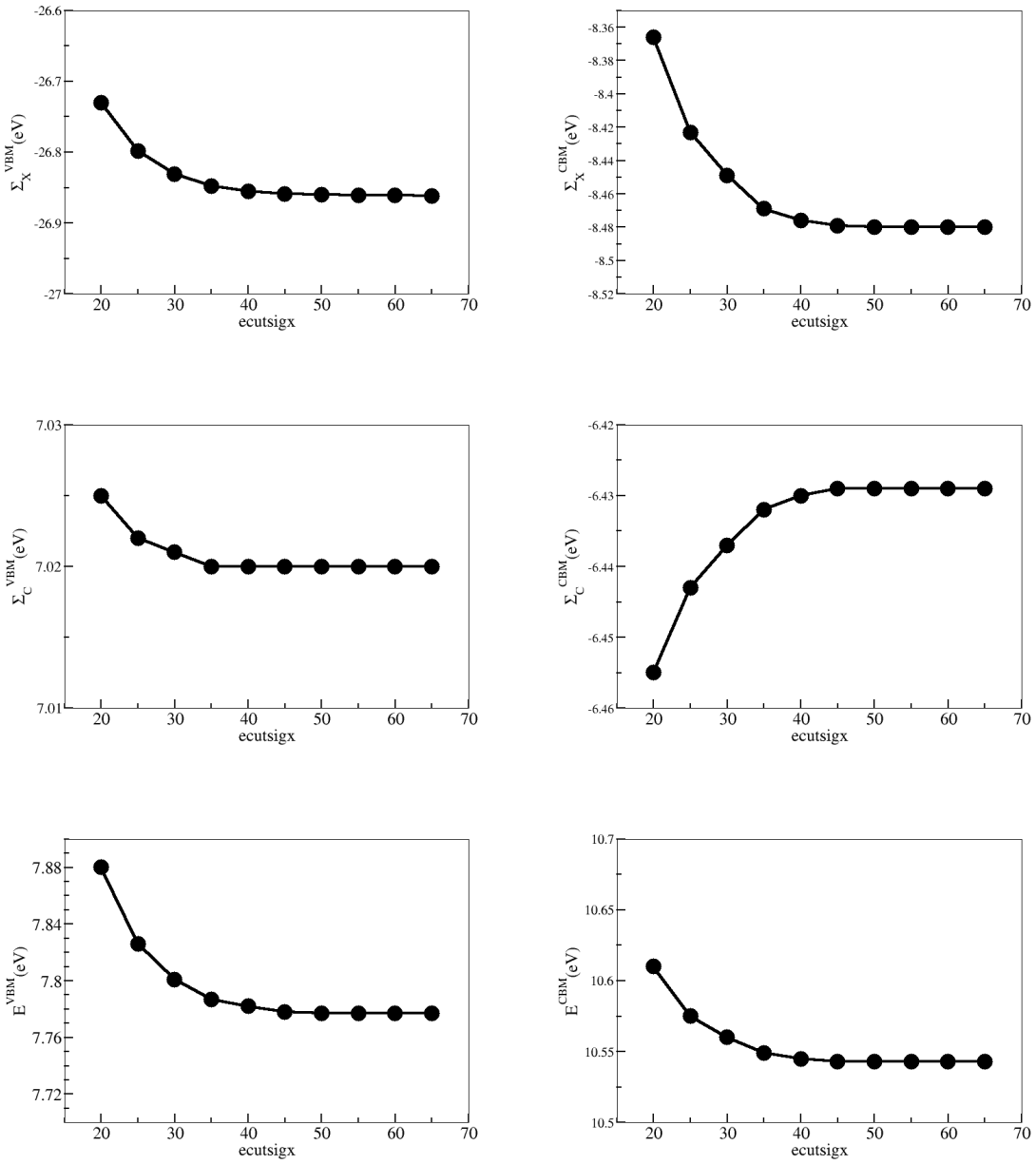

Figure 9.8: Convergence of the exchange (Σ_x) and correlation (Σ_x) part of self-energy along with the GW eigenvalue (E) of VBM (left panel) and CBM (right panel) w.r.to *ecutsigx* used in the self-energy calculations.

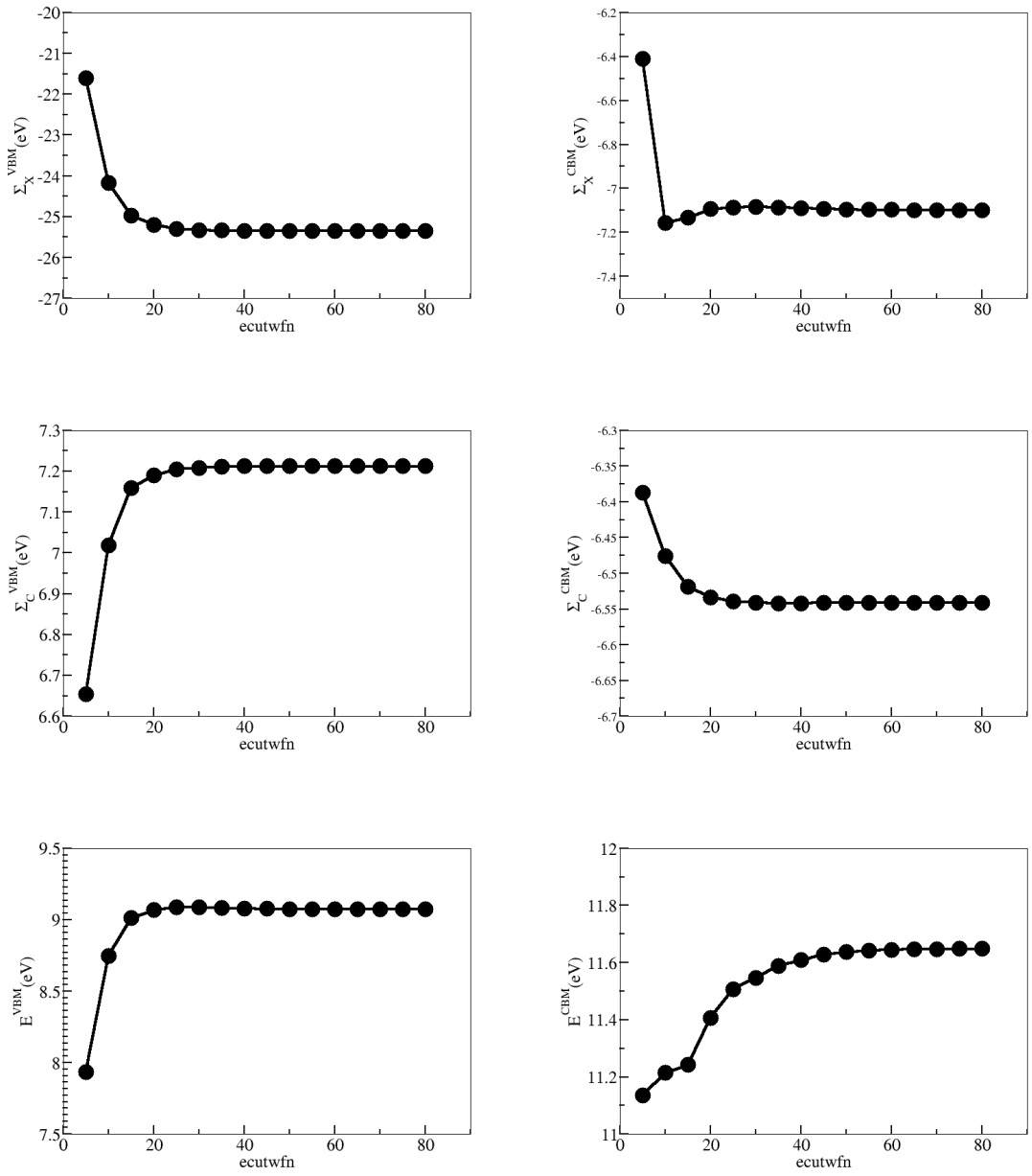

Figure 9.9: Convergence of the exchange (Σ_x) and correlation (Σ_x) part of self-energy along with the GW eigenvalue (E) of VBM (left panel) and CBM (right panel) w.r.to *ecutwfn* used in the self-energy calculations.

Table 9.5: The convergence of VBM and CBM with respect to *ecutwfn*, the converged values are highlighted with the bold face.

	VBM			CBM		
ecutwfn	Σ_x	Σ_c	E	sigx	Σ_c	E
5	-21.604	6.654	7.934	-6.412	-6.387	11.135
10	-24.174	7.018	8.748	-7.156	-6.476	11.214
15	-24.969	7.159	9.011	-7.134	-6.519	11.242
20	-25.205	7.189	9.067	-7.095	-6.534	11.406
25	-25.299	7.205	9.088	-7.086	-6.539	11.506
30	-25.328	7.208	9.086	-7.083	-6.541	11.547
35	-25.342	7.211	9.081	-7.087	-6.542	11.589
40	-25.345	7.212	9.078	-7.091	-6.542	11.608
45	-25.346	7.212	9.076	-7.094	-6.541	11.628
50	-25.346	7.212	9.074	-7.096	-6.541	11.636
55	-25.346	7.212	9.075	-7.098	-6.541	11.642
60	**-25.346**	**7.212**	**9.074**	**-7.098**	**-6.541**	**11.644**
65	-25.346	7.212	9.074	-7.099	-6.541	11.647
70	-25.346	7.212	9.075	-7.099	-6.541	11.647
75	-25.346	7.212	9.074	-7.099	-6.541	11.648
80	-25.346	7.212	9.075	-7.099	-6.541	11.648

Table 9.6: The convergence of VBM and CBM with respect to *nband*, the converged values are highlighted with the bold face.

	VBM			CBM		
nband	Σ_x	Σ_c	E	Σ_x	Σ_c	E
50	-26.86	7.514	8.151	-8.48	-6.142	10.764
100	-26.86	7.196	7.91	-8.48	-6.336	10.615
150	-26.86	7.103	7.84	-8.48	-6.386	10.576
200	-26.86	7.056	7.805	-8.48	-6.414	10.555
250	-26.86	7.02	7.777	-8.48	-6.429	10.543
300	**-26.86**	**7.005**	**7.766**	**-8.48**	**-6.437**	**10.537**
350	-26.86	6.993	7.757	-8.48	-6.442	10.533
400	-26.86	6.981	7.748	-8.48	-6.447	10.529
450	-26.86	6.979	7.747	-8.48	-6.448	10.528
500	-26.86	6.972	7.741	-8.48	-6.451	10.526
550	-26.86	6.968	7.739	-8.48	-6.452	10.525
600	-26.86	6.965	7.736	-8.48	-6.453	10.524
650	-26.86	6.965	7.736	-8.48	-6.453	10.524
700	-26.86	6.962	7.734	-8.48	-6.454	10.524
750	-26.86	6.961	7.733	-8.48	-6.454	10.523
800	-26.86	6.959	7.732	-8.48	-6.455	10.523
850	-26.86	6.958	7.731	-8.48	-6.455	10.523
900	-26.86	6.957	7.73	-8.48	-6.455	10.523
950	-26.86	6.957	7.73	-8.48	-6.456	10.522
1000	-26.86	6.957	7.73	-8.48	-6.456	10.522

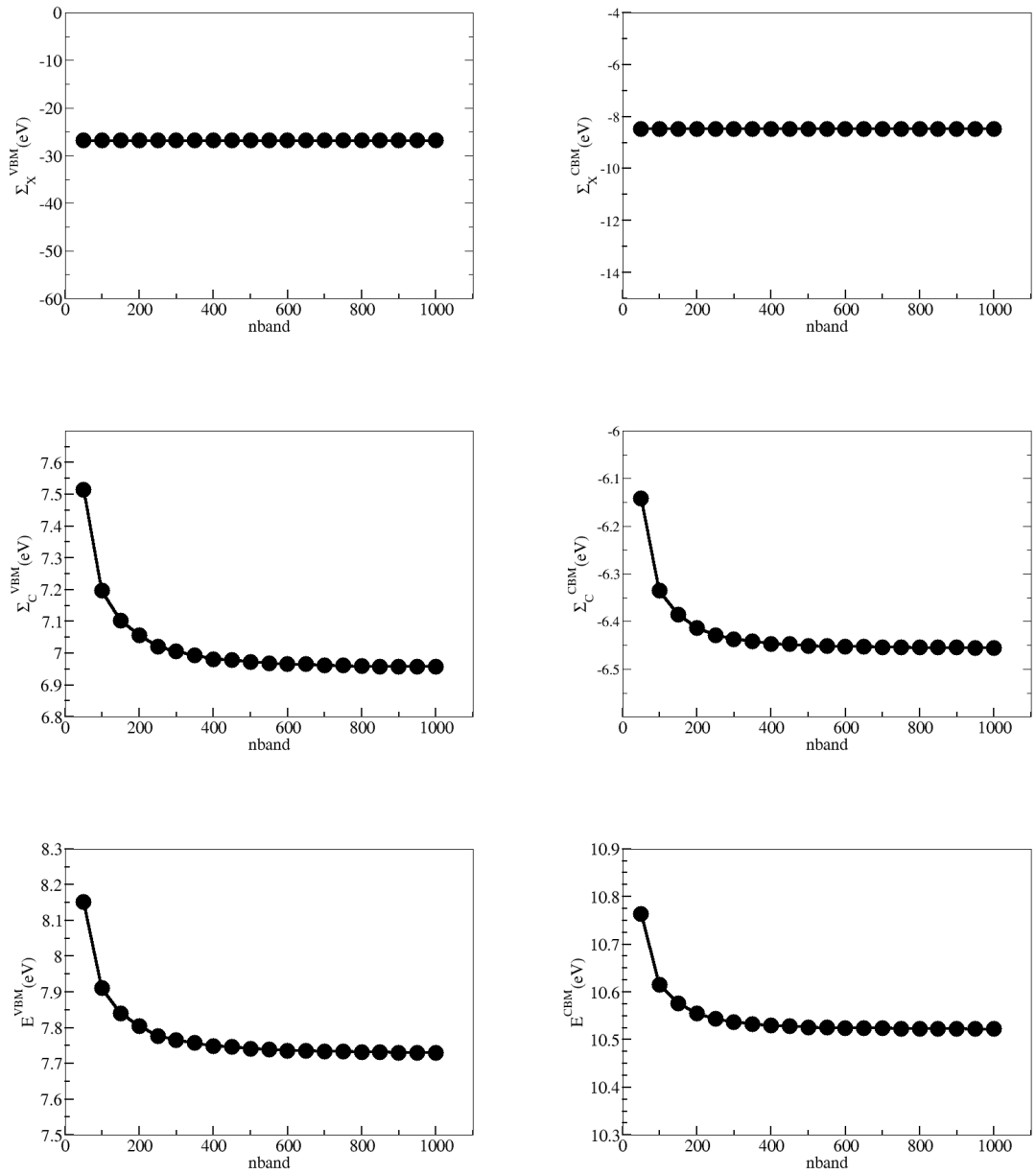

Figure 9.10: Convergence of the exchange (Σ_x) and correlation (Σ_x) part of self-energy along with the GW eigenvalue (E) of VBM (left panel) and CBM (right panel) w.r.to *nband* used in the self-energy calculations.

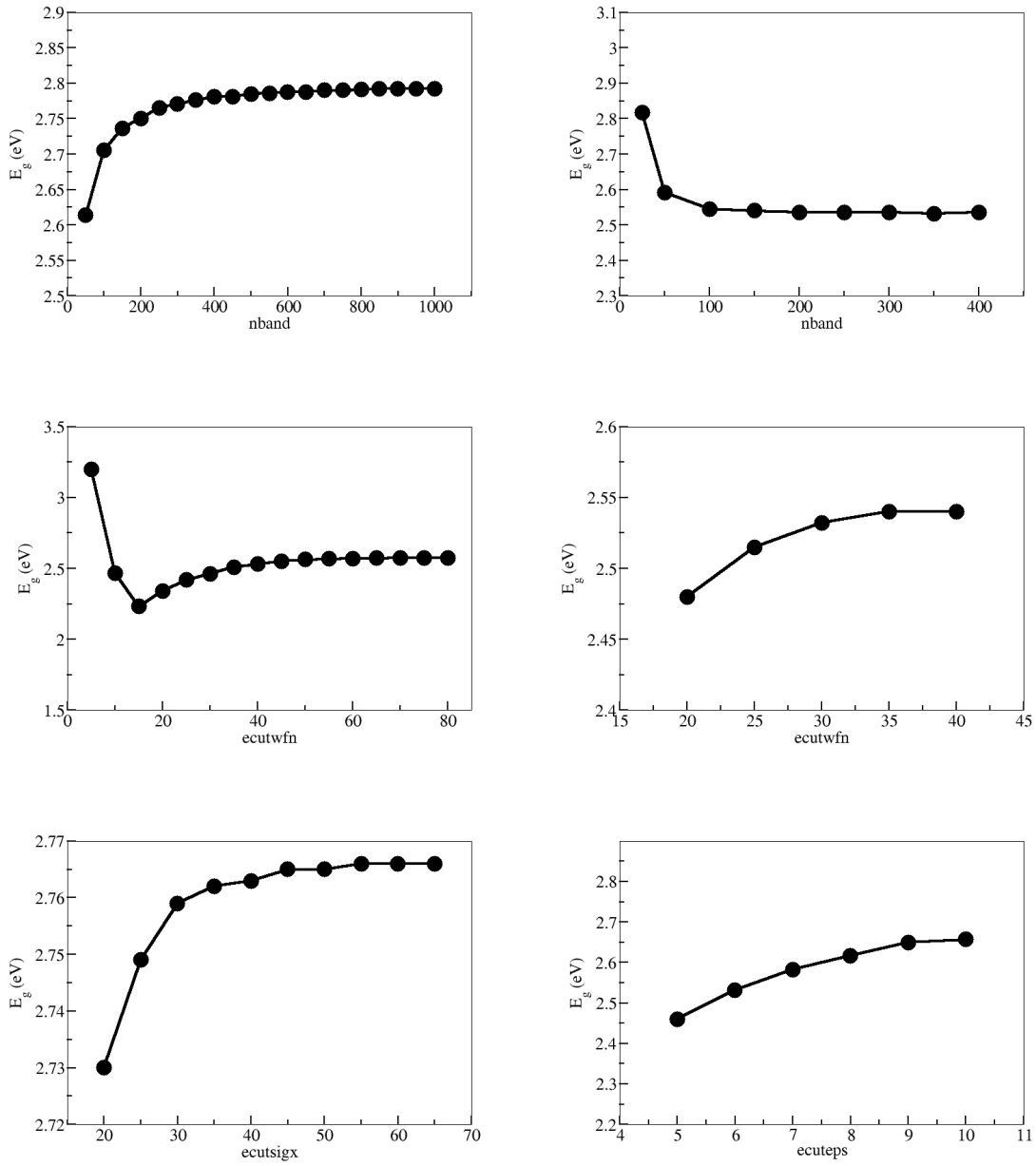

Figure 9.11: Convergence of the GW band gap (E_g) w.r.to *nband*, *ecutwfn* and *ecuteps*, *ecutsigx* used in the screening and self-energy calculations respectively.

Table 9.7: The convergence of band gap w.r.to parameters used in the screening computation, the converged values are highlighted with the bold face.

ecutsigx	E_g	ecutwfn	E_g	nband	E_g
5	2.46	20	2.48	25	2.817
6	2.532	25	2.515	50	2.592
7	2.582	30	2.532	100	2.545
8	2.617	**35**	2.54	150	2.54
9	2.65	40	2.54	**200**	**2.535**
10	**2.657**			250	2.536
				300	2.535
				350	2.532
				400	2.535

Table 9.8: The convergence of band gap w.r.to parameters used in the self-energy computation, the converged values are highlighted with the bold face.

nband	E_g	ecutwfn	E_g	ecutsigx	E_g
ecutsigx	E_g	ecutwfn	E_g	nband	E_g
20	2.73	5	3.201	50	2.614
25	2.749	10	2.466	100	2.705
30	2.759	15	2.231	150	2.736
35	2.762	20	2.34	200	2.75
40	**2.763**	25	2.418	250	2.765
45	2.765	30	2.461	**300**	**2.771**
50	2.765	35	2.508	350	2.776
55	2.766	40	2.53	400	2.781
60	2.766	45	2.551	450	2.781
65	2.766	**50**	**2.562**	500	2.785
		55	2.567	550	2.786
		60	2.569	600	2.788
		65	2.572	650	2.788
		70	2.573	700	2.79
		75	2.573	750	2.79
		80	2.574	800	2.791
				850	2.792
				900	2.792
				950	2.792
				1000	2.792

Appendix B

Projected weights of the Kohn-Sham wave functions

We have listed the projected weights of the Kohn-Sham wave functions, for the three systems discussed, at the Γ, K and L point in Table 9.9, 9.10, and 9.11. The eleven bands presented include nine occupied (valence) and two unoccupied (conduction) bands. The ZB-ZnO is a strongly hybridized system - as the 'p' and 'd' states show significant mixing (Table 9.9). For the RS-ZnO, the $p-d$ hybridization is absent at the Γ point (Table 9.10). The five valence bands (band index 2 to 6) show a strong 'd' character and the top three valence bands (band index 7 to 9) have a strong 'p' character. However at the K and L point they mix with each other. In the case of ZnS, the electronic structure shows a weaker hybridization compared to that of ZB-ZnO as evident from the projected weights of the Kohn-Sham wavefunction at the Γ, K and L point, listed in Table 9.11.

Table 9.9: The projected weights of the Kohn-Sham wavefunction at LDA level for ZB-ZnO with 12-electron Zn-PP at optimized lattice constant

At Γ point					
Band index	$Zn-3d$	$Zn-4s$	$O-s$	$O-p$	Energy(eV)
1	0.00	0.00	0.88	0.00	-17.91
2	0.76	0.00	0.00	0.28	-6.19
3	0.76	0.00	0.00	0.28	-6.19
4	0.76	0.00	0.00	0.28	-6.19
5	0.98	0.00	0.00	0.02	-4.94
6	0.98	0.00	0.00	0.02	-4.94
7	0.28	0.00	0.00	0.69	0.00
8	0.28	0.00	0.00	0.69	0.00
9	0.28	0.00	0.00	0.69	0.00
10	0.00	0.30	0.30	0.00	0.79
11	0.00	0.00	0.00	0.00	13.40
At K point					
1	0.00	0.00	0.94	0.00	-16.88
2	0.55	0.05	0.00	0.36	-6.28
3	0.77	0.00	0.00	0.24	-5.51
4	0.87	0.01	0.00	0.10	-5.19
5	0.98	0.00	0.00	0.00	-4.87
6	0.15	0.15	0.00	0.58	-4.49
7	0.91	0.17	0.01	0.03	-4.35
8	0.40	0.03	0.00	0.42	-2.91
9	0.23	0.00	0.00	0.64	-1.84
10	0.12	0.00	0.04	0.10	6.68
11	0.01	0.43	0.03	0.28	8.86
At L point					
1	0.00	0.00	0.93	0.00	-17.10
2	0.07	0.15	0.00	0.59	-5.99
3	0.77	0.00	0.00	0.25	-5.94
4	0.77	0.00	0.00	0.25	-5.94
5	0.98	0.00	0.00	0.00	-4.86
6	0.98	0.00	0.00	0.00	-4.85
7	0.87	0.03	0.01	0.08	-4.54
8	0.24	0.00	0.00	0.68	-0.86
9	0.24	0.00	0.00	0.68	-0.86
10	0.03	0.34	0.19	0.01	5.62
11	0.05	0.03	0.00	0.44	7.96

Table 9.10: The projected weights of the Kohn-Sham wavefunction at LDA level for RS-ZnO with 12-electron Zn-PP at optimized lattice constant

At Γ point					
Band index	$Zn-3d$	$Zn-4s$	$O-s$	$O-p$	Energy(eV)
1	0.00	0.00	0.86	0.00	-18.25
2	0.96	0.00	0.00	0.00	-5.38
3	0.96	0.00	0.00	0.00	-5.38
4	0.96	0.00	0.00	0.00	-5.38
5	0.98	0.00	0.00	0.00	-5.18
6	0.98	0.00	0.00	0.00	-5.18
7	0.00	0.00	0.00	0.96	-1.17
8	0.00	0.00	0.00	0.96	-1.17
9	0.00	0.00	0.00	0.96	-1.17
10	0.00	0.43	0.41	0.00	1.37
11	0.40	0.00	0.00	0.00	18.36
At K point					
1	0.00	0.00	0.94	0.00	-16.52
2	0.60	0.04	0.00	0.28	-6.16
3	0.39	0.00	0.00	0.44	-5.86
4	0.78	0.00	0.00	0.22	-5.66
5	0.99	0.00	0.00	0.00	-4.92
6	0.87	0.01	0.02	0.08	-4.86
7	0.60	0.00	0.00	0.31	-3.92
8	0.45	0.10	0.01	0.38	-3.22
9	0.23	0.00	0.00	0.67	-1.41
10	0.00	0.57	0.05	0.10	6.43
11	0.11	0.02	0.04	0.25	10.09
At L point					
1	0.00	0.00	0.94	0.00	-16.69
2	0.29	0.19	0.00	0.48	-7.51
3	0.77	0.00	0.00	0.25	-6.21
4	0.77	0.00	0.00	0.25	-6.21
5	0.98	0.00	0.00	0.00	-4.96
6	0.98	0.00	0.00	0.00	-4.96
7	0.71	0.09	0.00	0.20	-3.92
8	0.28	0.00	0.00	0.71	0.11
9	0.28	0.00	0.00	0.71	0.11
10	0.00	0.00	0.21	0.01	5.55
11	0.00	0.36	0.00	0.55	9.44

Table 9.11: The projected weights of the Kohn-Sham wavefunction at LDA level for ZnS with 12-electron Zn-PP at optimized lattice constant

At Γ point					
Band index	$Zn-3d$	$Zn-4s$	$O-s$	$O-p$	Energy(eV)
1	0.00	0.00	0.69	0.00	-13.49
2	0.88	0.00	0.00	0.08	-6.82
3	0.88	0.00	0.00	0.08	-6.82
4	0.88	0.00	0.00	0.08	-6.82
5	0.97	0.00	0.00	0.00	-6.30
6	0.97	0.00	0.00	0.00	-6.30
7	0.14	0.00	0.00	0.70	0.00
8	0.14	0.00	0.00	0.70	0.00
9	0.14	0.00	0.00	0.70	0.00
10	0.00	0.29	0.30	0.00	1.90
11	0.25	0.00	0.00	0.38	6.10
At K point					
1	0.06	0.00	0.79	0.00	-12.11
2	0.80	0.01	0.00	0.09	-6.74
3	0.92	0.00	0.00	0.05	-6.53
4	0.94	0.01	0.00	0.01	-6.42
5	0.97	0.00	0.00	0.00	-6.26
6	0.91	0.00	0.03	0.00	-5.97
7	0.10	0.29	0.00	0.38	-4.97
8	0.10	0.00	0.00	0.46	-3.49
9	0.07	0.00	0.00	0.59	-1.73
10	0.06	0.10	0.03	0.04	3.86
11	0.03	0.17	0.00	0.28	5.86
At L point					
1	0.04	0.04	0.79	0.00	-12.44
2	0.89	0.00	0.00	0.06	-6.70
3	0.89	0.00	0.00	0.06	-6.70
4	0.97	0.00	0.00	0.00	-6.27
5	0.97	0.00	0.00	0.00	-6.27
6	0.90	0.00	0.02	0.00	-6.08
7	0.02	0.02	0.00	0.41	-5.73
8	0.10	0.00	0.00	0.65	-0.97
9	0.10	0.00	0.00	0.65	-0.97
10	0.01	0.30	0.19	0.03	3.07
11	0.04	0.00	0.00	0.27	6.73

List of publications

Publications related to this thesis

1. H. Dixit, R. Saniz, D. Lamoen and B. Partoens: *The quasiparticle band structure of zincblende and rocksalt ZnO*, J. Phys.: Condens. Matter 22, 125505 (2010)

2. R. Saniz, H. Dixit, D. Lamoen and B. Partoens: *Quasiparticle energies and uniaxial pressure effects on the properties of SnO_2*, Applied Physics Letters 97, 261901 (2010)

3. H. Dixit, R. Saniz, D. Lamoen and B. Partoens: *Accurate pseudopotential description of the GW bandstructure of zincblende and rocksalt ZnO*, Computer Physics Communications 182, 2029 (2011).

4. H. Dixit, Nandan Tandon, R. Saniz, S. Cottenier, D. Lamoen, B. Partoens, V. Van Speybroeck and M. Waroquier: *Electronic structure and band gap of zinc spinel oxides beyond LDA: $ZnAl_2O_4$, $ZnGa_2O_4$, and $ZnIn_2O_4$*, New Journal of Physics, 13, 063002 (2011).

5. M. Stankovski, G. Antonius, D. Waroquiers, A. Miglio, H. Dixit, K. Sankaran, M. Giantomassi, X. Gonze, M. Côté, and G.-M. Rignanese: *The G_0W_0 band gap of ZnO: effects of plasmon-pole models*, Phys. Rev. B 84, 241201(R) (2011)

6. H. Dixit, R. Saniz, S. Cottenier, D. Lamoen and B. Partoens: *Electronic structure of transparent oxides with the Tran-Blaha modied Becke-Johnson density functional* , J. Phys.: Condens. Matter 24, 205503 (2012)

Other publications

7. N. Arun, Ashutosh Sharma, Partho S. G. Pattader, Indrani Banerjee, Hemant M. Dixit, and K. S. Narayan: *Electric-Field-Induced Patterns*

in Soft Viscoelastic Films: From Long Waves of Viscous Liquids to Short Waves of Elastic Solids, Phys. Rev. Lett. 102, 254502 (2009).

8. Hemant Dixit, Ganesh Bagler, Somdatta Sinha: *Modelling the host-parasite interaction*, Proceedings of the First Conference on Nonlinear Systems and Dynamics, IIT Kharagpur, pp. 321324, (2003).

Curriculum Vitae

Name: **Hemant Dixit**

Born: 04/07/1982, Ahmednagar, INDIA

Contact: U 313, Groenenborgerlaan 171
2020, Antwerp, BELGIUM

E-mail: Hemant.Dixit@ua.ac.be

Education

2008-2012: **PhD** University of Antwerp, BELGIUM

2002-2004: **MSc** University Of Pune, INDIA

1999-2002: **BSc** University Of Pune, INDIA

Honors & Awards

Jan - 2004 V. Subramanian best student award by
Physics Department, University Of Pune

Research experience

2006-2008 **Research Intern**
Motorola Research Lab, Bangalore, INDIA

2005-2006 **R&D Assistant**
JNCASR, Bangalore, INDIA

2004-2005 **Junior Research Fellow**
University of Pune, Pune, INDIA

Oral presentations

Invited talk	**ICTP, Trieste, Italy** *Ab-initio electronic structure calculations of Transparent Conducting Oxides.* [45 min.] February 8, 2012.
Symposium	**Yang Symposium, Brussels, Belgium** *Electronic structure and optical properties of Transparent Conducting Oxides.* [30 min.] November 15, 2010.
Workshop	**Trinity college, Dublin, Ireland** *Quasiparticle band gaps of IIB-VI transparent oxides within the GW approximation.* [20 min.] September 11, 2009.

Professional training

CECAM Workshop	**CECAM-HQ-EPFL, Lausanne, Switzerland** *Materials Informatics: Tools for Design and Discovery* May 23 - 25, 2011.
CECAM Workshop	**CECAM-ETHZ, Zurich, Switzerland** *Theoretical Spectroscopy Lectures: Theory and Codes* May 25 - 29, 2009.
Summer school	**Miramar Palace, San Sabastian, Spain** *Summer-School on Computational Materials Sciences* June 28 - 3, 2010.

Computer skills

Operating systems:	Windows, Linux
Programming (basic):	C/C++, Fortran, Python
DFT packages:	ABINIT, WIEN2K, VASP
Mathematical software:	MATLAB, Gnuplot, Xmgrace

Languages

Marathi (native), Hindi (fluent), English (fluent)

Bibliography

[1] R. G. Gorden *MRS Bulletin* 52 August (2000)

[2] T. Minami, *Semicond. Sci. Technol.* **20** S35 (2005)

[3] H. Kawazoe M. Yasukawa, H. Hyodo, M. Kurita, H. Yanagi and H. Hosono, *Nature (London)* **389**, 939 (1997).

[4] H. Yanagi, K. Ueda, H. Kawazoe and H. Hosono, *J. Appl. Phys.* **88**, 4159 (2000).

[5] K. Ueda, T. Hase, H. Yanagi, H. Kawazoe, H. Hosono, H. Ohta, M. Orita and M. Hirano, *J. Appl. Phys.* **89**, 1790 (2001).

[6] H. Yanagi, T. Hase, S. Ibuki, K. Ueda and H. Hosono, *Appl. Phys. Lett.* **78**, 1583 (2001).

[7] H. Mizoguchi, M. Hirano, S. Fujitsu, T. Takeuchi, K. Ueda and H. Hosono, *Appl. Phys. Lett.* **80**, 1207 (2002).

[8] H. J. Kim, I. C. Song, J. H. Sim, H. Kim, D. Kim, Y. E. Ihm and W. K. Choo, *J. Appl. Phys.* **95**, 7387 (2004).

[9] M. Dekkers, G. Rijnders and D. H. A. Blank, *Appl. Phys. Lett.* **90**, 021903 (2007).

[10] S. Bae, H. Kim, Y. Lee, X. Xu, J.-S. Park, Yi Zheng, J. Balakrishnan, T. Lei, H. R. Kim, Y. I. Song, Y.-J. Kim, K. S. Kim, B. Özyilmaz, J.-H. Ahn, B. H. Hong and S. Iijima *Nature Nanotechnology* **5**, 574-578 (2010)

[11] K. S. Kim, Y. Zhao, H. Jang, S. Y. Lee, J. M. Kim, K. S. Kim, J.-H. Ahn, P. Kim, J.-Y. Choi and B. H. Hong, *Nature* **457**, 706-710 (2009).

[12] C. M. Weber, D. M. Eisele, J. P. Rabe,Y. Liang, X. Feng, L. Zhi, K. Müllen, J. L. Lyon, R. Williams, D. A. Vanden Bout, and K. J. Stevenson *Small* **6**, 184-189 (2010).

[13] E. Burstein, *Phys. Rev.* **93**, 632 (1954)

[14] G. J. Exarhos and X.-D. Zhou, *Thin Solid Films* **515**, 70257052 (2007)

[15] I. Hamberg and C. G. Granqvist, *J. Appl. Phys.* **60**, R213 (1986)

[16] P. P. Edwards, A. Porch, M. O. Jones, D. V. Morgan and R. M. Perks, *Dalton Trans.* 2995-3002, (2004).

[17] C. G. Van de Walle and J. Neugebauer, *J. Appl. Phys.* **95**, 3851 (2004)

[18] E. Verploegen, R. Mondal, C. Bettinger, S. Sok, M. Toney, Z. Bao, *Advanced Functional Materials* **20**, 3519-3529 (2010)

[19] J. P. Perdew, R. G. Parr, M. Levy and J. L. Balduz Jr., *Phys. Rev. Lett.* **49**, 1691 (1982)

[20] L. J. Sham and M. Schlüter, *Phys. Rev. Lett.* **51**, 1888 (1983)

[21] L. J. Sham and M. Schlüter, *Phys. Rev. B* **32**, 3883 (1985).

[22] W. Kohn, *Phys. Rev. B* **33**, 4331 (1986).

[23] W. G. Aulbur, L. Jönsson, and J. W. Wilkins, *Solid State Phys.* **54**, 1 (2000).

[24] X. Gonze, J.-M. Beuken, R. Caracas, F. Detraux, M. Fuchs, G.-M. Rignanese, L. Sindic, M. Verstraete, G. Zerah, F. Jollet, M. Torrent, A. Roy, M. Mikami, P. Ghosez, J.-Y. Raty, and D.C. Allan, *Comput. Mater. Sci.* **25**, 478 (2002).

[25] X. Gonze, X. Gonze, G.-M. Rignanese, M. Verstraete, J.-M. Beuken, Y. Pouillon, R. Caracas, F. Jollet, M. Torrent, G. Zerah, M. Mikami, Ph. Ghosez, M. Veithen, J.-Y. Raty, V. Olevano, F. Bruneval, L. Reining, R.W. Godby, G. Onida, D.R. Hamann, and D.C. Allan, *Zeit. Kristallogr.* **220**, 558 (2005).

[26] F. Bruneval, N. Vast, and L. Reining, *Phys. Rev. B* **74**, 045102 (2006).

[27] M. C. Payne, M. P. Teter. D. C. Allan. T. A. Arias and J. D. Joannopoulos, *Rev. Mod. Phys.* **64** 1045 (1991)

[28] R. G. Parr and W. Yang, *Density-Functional Theory of Atoms and Molecules* New York: Oxford University Press. ISBN 0-19-509276-7 (1989)

[29] R. M. Martin, *Electronic Structure: Basic theory and practical methods* Cambridge University Press ISBN 0-521-78285-6 (2004)

[30] J. Kohanoff, *Electronic structure calculations for solids and molecules: theory and computational methods* Cambridge University Press ISBN-10 0-521-81591-8 (2006)

[31] P. Hohenberg and W. Kohn, *Phys. Rev.* **136**, B684 (1964).

[32] W. Kohn and L. J. Sham *Phys. Rev.* **140**, A1133 (1965).

[33] D.M. Ceperley and B.J Alder, *Phys. Rev. Lett.* **45** 566 (1980)

[34] J. P. Perdew, K. Burke and M. Ernzerhof, *Phys. Rev. Lett.* **77**, 3865-3868 (1996)

[35] J. Heyd, G. E. Scuseria and M. Ernzerhof, *J. Chem. Phys.* **118**, 8207 (2003).

[36] J. Heyd, J.E. Peralta, G. E. Scuseria and R. L. Martin, *J. Chem. Phys.* **123**, 174101 (2006).

[37] A. Janotti and C. G. Van de Walle, *Phys. Status Solidi. B* **248** 799 (2011).

[38] H. D. Monkhorst and J. D. Pack, *Phys. Rev. B* **13**, 5188 (1976).

[39] G. B. Bachelet, D. R. Hamann and M. Schlüter, *Phys. Rev. B* **26**, 4199 (1982)

[40] http://opium.sourceforge.net/index.html

[41] P. E. Blöchl, *Phys. Rev. B* **50**, 17953 (1994).

[42] P. Schröder, P. Krüger, and J. Pollmann, *Phys. Rev. B* **47**, 6971 (1993).

[43] http://www.fhi-berlin.mpg.de/th/fhi98md/fhi98PP

[44] Ü. Özgür, Ya. I. Alivov, C. Liu, A. Teke, M. A. Reshchikov, S. Doan, V. Avrutin, S.-J. Cho, and H. Morkoç, *J. Appl. Phys.* **98**, 041301 (2005).

[45] O. M. Madelung, *Semiconductors: Data Handbook*, 3rd ed. (Springer, Berlin, 2004).

[46] L. Ley, R. A. Pollak, F. F. Mcfeely, S. P. Kowalczyk, and D. A. Shirley, *Phys. Rev. B* **9**, 600 (1974).

[47] C. McGuinness, C. B. Stagarescu, P. J. Ryan, J. E. Downes, D. Fu and K. E. Smith, *Phys. Rev. B* **68**, 165104 (2003).

[48] S.-H. Wei and A. Zunger, *Phys. Rev. B* **37**, 8958 (1988).

[49] A.A. Bolzan, C. Fong, B.J. Kennedy, and C.J. Howard, *Acta Crystallogr. Sect. B-Struct. Sci.* **53** 373 (1997).

[50] M. Batzill, U. Diebold, *Progress in Surface Science* **79** 47154 (2005)

[51] M. Marezio, *Acta Crystallogr.* **20** 723 (1966).

[52] A. Walsh, J. L. F. Da Silva, S.-H. Wei, C. Körber, A. Klein, L. F. J. Piper, A. DeMasi, K. E. Smith, G. Panaccione, P. Torelli, D. J. Payne, A. Bourlange and R. G. Egdell, *Phys. Rev. Lett.* **100**, 167402 (2008)

[53] O. N. Mryasov and A. J. Freeman, *Phys. Rev. B* **64**, 233111 (2001).

[54] G. D. Mahan, *Many-Particle Physics* Plenum Press, New York, 1981.

[55] L. Hedin, *Phys. Rev.* **139**, A796-A823 (1965).

[56] C. Friedrich and A. Schindlmayr, *Computational Nanoscience: Do It Yourself!* John von Neumann Institute for Computing, Jülich, NIC Series, **31**, 335-355, (2006).

[57] M. van Schilfgaarde, T. Kotani, and S. Faleev, *Phys. Rev. Lett.* **96**, 226402 (2006)

[58] P. Duffy, D. P. Chong, M. E. Casida, and D. R. Salahub, *Phys. Rev. A* **50**, 4707 (1994)

[59] F. Bruneval, *Exchange and Correlation in the Electronic Structure of Solids, from Silicon to Cuprous Oxide: GW Approximation and beyond* PhD thesis, Ecole polytechnique, (2005).

[60] R. W. Godby and R. J. Needs, *Phys. Rev. Lett.* **62**, 1169 (1989).

[61] M. S. Hybertsen and S. G. Louie, *Phys. Rev. B* **34**, 5390 (1986).

[62] G. E. Engel and B. Farid, *Phys. Rev. B* **47**, 15931 (1993).

[63] W. von der Linden and P. Horsch, *Phys. Rev. B* **37**, 8351 (1988).

[64] A. Ashrafi and C. Jagadish, *J. Appl. Phys.* **102**, 071101 (2007).

[65] J. A. Sans, A. Segura, F. J. Manjón, B. Marí, A. Muñoz, and M. J. Herrera-Cabrera, *Microelectron. J.* **36**, 928 (2005).

[66] A. Schleife, F. Fuchs, J. Furthmüller, and F. Bechstedt, *Phys. Rev. B* **73**, 245212 (2006).

[67] N. Troullier and J. L. Martins, *Phys. Rev. B* **43**, 1993 (1991).

[68] J. P. Perdew and A. Zunger, *Phys. Rev. B* **23**, 5048 (1981).

[69] M. Rohlfing, P. Krüger, and J. Pollmann, *Phys. Rev. Lett.* **75**, 3489 (1995).

[70] M. Rohlfing, P. Krüger, and J. Pollmann, *Phys. Rev. B* **57**, 6485 (1998).

[71] P. Rinke, A. Qteish, J. Neugebauer, C. Freysoldt, and M. Scheffler, *New J. Phys.* **7**, 126 (2005).

[72] M. Usuda, N. Hamada, T. Kotani, and M. van Schilfgaarde, *Phys. Rev. B* **66**, 125101 (2002).

[73] T. Kotani, M. van Schilfgaarde, and S. V. Faleev, *Phys. Rev. B* **76**, 165106 (2007).

[74] F. Decremps, F. Datchi, A. M. Saitta, A. Polian, S. Pascarelli, A. Di Cicco, J. P. Itié, and F. Baudelet, *Phys. Rev. B* **68**, 104101 (2003).

[75] T. Miyake, P. Zhang, M. L. Cohen, and S. G. Louie, *Phys. Rev. B* **74**, 245213 (2006).

[76] B.-C. Shih, Y. Xue, P. Zhang, M. L. Cohen, and S. G. Louie, *Phys.Rev. Lett.* **105**, 146401 (2010)

[77] R. Shaltaf, G.-M. Rignanese, X. Gonze, F. Giustino, and A. Pasquarello, *Phys. Rev. Lett.* **100**, 186401 (2008).

[78] W. Kang and M. S. Hybertsen, *Phys. Rev. B* **82**, 085203 (2010).

[79] M. Stankovski, G. Antonius, D. Waroquiers, A. Miglio, H. Dixit, K. Sankaran, M. Giantomassi, X. Gonze, M. Côté, and G.-M. Rignanese, *Phys. Rev. B* **84**, 241201(R) (2011)

[80] M. Palummo, L. Reining, M. Meyer, and C. M. Bertoni, *22nd International Conference on the Physics of Semiconductors*, edited by D. J. Lockwood Vol.1 p.161 (World Scientific, Singapore, 1995).

[81] L. A. Errico, *Physica B* **389**, 140 (2007).

[82] A. A. Bolzan, C. Fong, B. J. Kennedy, and C. J. Howard, *Acta Crystallogr., Sect. B: Struct. Sci.* **53**, 373 (1997).

[83] J. Robertson, *J. Phys. C* **12**, 4767 (1979).

[84] Y. Duan, *Phys. Rev. B* **77**, 045332 (2008).

[85] P. D. Borges, L. M. R. Scolfaro, H. W. Leite Alves, and E. F. da Silva, Jr., *Theor. Chem. Acc.* **126**, 39 (2010).

[86] H. Dixit, R. Saniz, D. Lamoen and B. Partoens, *J. Phys.: Condens. Matter* **22**, 125505 (2010).

[87] M. Nagasawa and S. Shionoya, *Phys. Lett.* **22**, 409 (1966).

[88] J. A. Berger, L. Reining, and F. Sottile, *Phys. Rev. B* **82**, 041103 (2010).

[89] K. J. Button, C. G. Fonstad, and W. Dreybrodt, *Phys. Rev. B* **4**, 4539 (1971).

[90] J. A. Marley and R. C. Dockerty, *Phys. Rev.* **140**, A304 (1965).

[91] S. Ohta, T. Sekiya, and S. Kurita, *Phys. Status Solidi B* **223**, 265 (2001).

[92] W. Shan, W. Walukiewicz, J. W. Ager III, K. M. Yu, and J. Wu, *Appl. Phys. Lett.* **84**, 67 (2004).

[93] G.H. Wannier, *Phys. Rev.* **52** 191 (1937).

[94] S.F. Boys, *Rev. Modern Phys.* **32** 296 (1960).

[95] J.M. Foster, S.F. Boys, *Rev. Modern Phys.* **32** 300 (1960) .

[96] N. Marzari, D. Vanderbilt, *Phys. Rev. B* **56** 12847 (1997).

[97] A.A. Mostofi, J.R. Yates, Y.-S. Lee, I. Souza, D. Vanderbilt, N. Marzari, *Comput. Phys. Comm.* **178** 685 (2008).

[98] J.R. Yates, X. Wang, D. Vanderbilt, I. Souza, *Phys. Rev. B* **75** 195121 (2007).

[99] D.R. Hamann, D. Vanderbilt, *Phys. Rev. B* **79** 045109 (2009).

[100] P. H. Jefferson, S. A. Hatfield, T. D. Veal, P. D. C. King, C. F. McConville, J. Zúñiga-Pérez, V. Muñoz-Sanjosé, *Appl. Phys. Lett.* **92** 022101 (2008).

[101] S.K. Sampath and J. F. Cordaro , *J. Am. Ceram. Soc.* **81**, 649 (1998).

[102] J. F. Cordaro, Patent 5820669 Hughes Electronic Corporation, Los Angeles, CA, US, 1998.

[103] Y. E. Lee, D. P. Norton, J. D. Budai, and Y. Wei, *J. Appl. Phys.* **90**, 3863 (2001).

[104] H. Kawazoe and K. Ueda, *J. Am. Ceram. Soc.* **82**, 3330 (1999).

[105] S. Z. Karazhanov, and P. Ravindran, *J. Am. Ceram. Soc.* **93**, 3335 (2010).

[106] S.K. Sampath , D.G. Kanhere and R. Pandey, *J. Phys.: Condens. Matter* **11**, 3635 (1999).

[107] A. Bouhemadou and R. Khenata, *Physics Letters A* **360**, 339 (2006).

[108] F. Tran , P. Blaha and K. Schwarz, *J. Phys.: Condens. Matter* **19**, 196208 (2007).

[109] F. Tran and P. Blaha, *Phys. Rev. Lett.* **102**, 226401 (2009)

[110] P. Blaha, K. Schwarz, G. K. H. Madsen, D. Kvasnicka and J. Luitz, **WIEN2K:***An augmented planewave + local orbitals program for calculating crystal properties* Karlheinz Schwarz, Techn.Universität Wien, Austria), 2001. ISBN 3-950131-1-2.

[111] S. Cottenier, Density Functional Theory and the Family of (L)APW-methods: a step-by-step introduction, (Instituut voor Kern- en Stralingsfysica, KULeuven, Belgium), ISBN 90-807215-1-4 (freely available from http://www.wien2k.at/reg_user/textbooks) (2002).

[112] K. Momma and F. Izumi, *J. Appl. Crystallogr.*, **44**, 1272-1276 (2011).

[113] R.J. Hill, J.R. Graig and G.V. Gibbs, *Phys. Chem. Miner.* **4**, 317 (1979).

[114] S.H. Wei and S. B. Zhang, *Phys. Rev. B* **63**, 45112 (2001).

[115] Y.S. Kim, M. Marsman, G. Kresse, F. Tran and P. Blaha, *Phys. Rev. B* **82**, 205212 (2010).

[116] R. E. Newnham und Y. M. de Haan, *Zeitschrift für Kristallographie* **117**, 235 (1962)

[117] M. Marezio and J. P. Remeika, *J. Chem. Phys.* **46**, 1862 (1967)

[118] A. N. Christensen and N. C. Broch, *Acta Chemica Scandinavica* **21**, 1046 (1967)

[119] http://www.materialsproject.org/

[120] M. Grüning, A. Marini and A. Rubio, *J. Chem. Phys.* **124**, 154108 (2006).

[121] M. Grüning, A. Marini and A. Rubio, *Phys. Rev. B* **74**, 161103(R) (2006).

[122] G. Barcaro, I. O. Thomas and A. Fortunelli, *The Journal of Chemical Physics* **132**, 124703 (2010)

[123] W. Feng, D. Xiao, Y. Zhang, and Y. Yao, *Phys. Rev. B* **82**, 235121 (2010)

[124] Y.-S. Kim, M. Marsman, G. Kresse, F. Tran and P. Blaha, *Phys. Rev. B* **82**, 205212 (2010)

[125] D. J. Singh, S. S. A. Seo and H. N. Lee, *Phys. Rev. B* **82**, 180103 (2010)

[126] D. J. Singh, *Phys. Rev. B* **82**, 205102 (2010)

[127] D. J. Singh, *Phys. Rev. B* **82**, 155145 (2010)

[128] S. Gong and B.-G. Liu, *Physics Letters A* **375**, 1477 (2011)

[129] N. W. Johnson, J. A. McLeod and A. Moewes, *Journal of Physics: Condensed Matter* **23**, 445501 (2011)

[130] H. Dixit, N. Tandon, S. Cottenier, R. Saniz, D. Lamoen, B. Partoens, V. Van Speybroeck and M. Waroquier, *New Journal of Physics* **13**, 063002 (2011)

[131] D. Koller, F. Tran and P. Blaha, *Phys. Rev. B* **83**, 195134 (2011)

[132] P. D. C. King, T. D. Veal, A. Schleife, J. Zúñiga-Pérez, B. Martel, P.H. Jefferson, F. Fuchs, V. Muñoz-Sanjosé, F. Bechstedt and C. F. McConville, *Phys. Rev. B* **79**, 205205 (2009).

[133] X. Nie, S.-H.Wei and S. B. Zhang, *Phys. Rev. Lett.* **88**, 066405 (2002)

[134] F. Trani, J. Vidal, S. Botti and M. A. L. Marques, *Phys. Rev. B* **82**, 085115 (2010).

[135] J. Vidal, F. Trani, F. Bruneval, M. A. L. Marques and S. Botti, *Phys. Rev. Lett.* **104**, 136401 (2010)

[136] R. Laskowski, N. E. Christensen, P. Blaha and B. Palanivel, *Phys. Rev. B* **79**, 165209 (2009).

[137] D. O. Scanlon and G. W. Watson, *Phys. Chem. Chem. Phys.* **13**, 9667 (2011)

[138] F. Fuchs and F. Bechstedt, *Phys. Rev. B.* **77**, 155107 (2008)

[139] R. Saniz, H. Dixit, D. Lamoen and B. Partoens, *Appl. Phys. Lett.* **97**, 261901 (2010).

[140] A. Schleife, J. B. Varley, F. Fuchs, C. Rödl, F. Bechstedt, P. Rinke, A. Janotti and C. G. Van de Walle, *Phys. Rev. B* **83**, 035116 (2011).

[141] A. Kokalj, *Comp. Mater. Sci.*, **28**, 155 (2003). Code available from http://www.xcrysden.org/.

[142] D. J. Aston, D. J. Payne, A. J. H. Green, R. G. Egdell, D. S. L. Law, J. Guo, P. A. Glans, T. Learmonth and K. E. Smith, *Phys. Rev. B* **72**, 195115 (2005).

[143] R. Pandey, J. D. Gale, S. K. Sampath and J. M. Recio, *J. Am. Ceram. Soc.* **82**, 3337 (1999).

[144] S. López, A. H. Romero, P. Rodríguez-Hernández, and A. Muñoz, *Phys. Rev. B* **79**, 214103 (2009).

[145] G. Kresse and J. Furthmüller, *Comput. Mater. Sci.* **6** (1996), 15; Phys. Rev. B **54**, 11169 (1996).

[146] A. Janotti and C. G. Van de Walle, *Phys. Rev. B* **76**, 165202 (2007).

[147] G. Kresse and D. Joubert, *Phys. Rev. B* **59**, 1758 (1999).

[148] Wei, S.-H. *Comput. Mater. Sci.* **30**, 337 (2004).

[149] A. Walsh, Y. Yan, M. M. Al-Jassim, and S.-H. Wei *J. Chem. Phys.* **112**, 12044 (2008).